Effectiveness of Thrust Vectoring Control for Longitudinal Trim of a Blended Wing Body Aircraft

Honglin Chen

Delft University of Technology

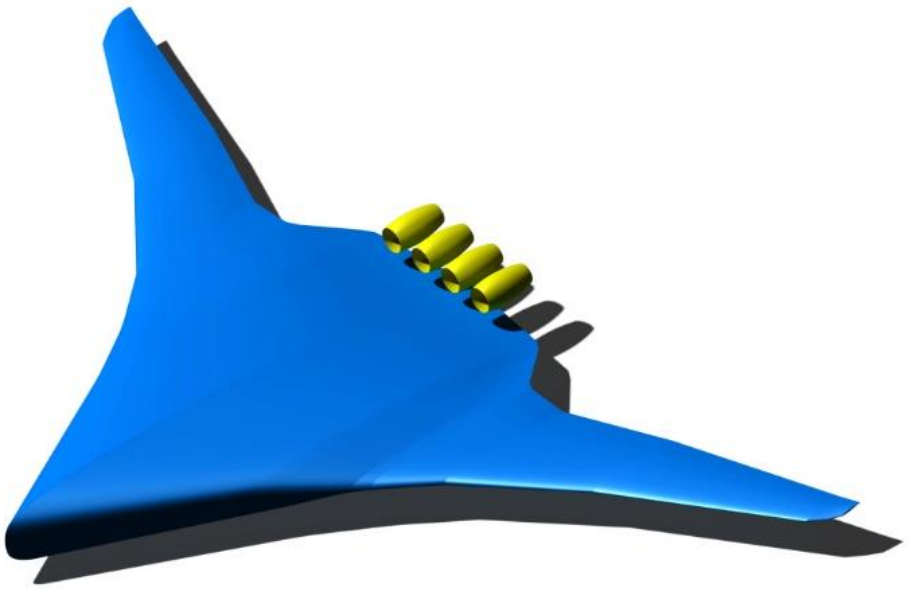

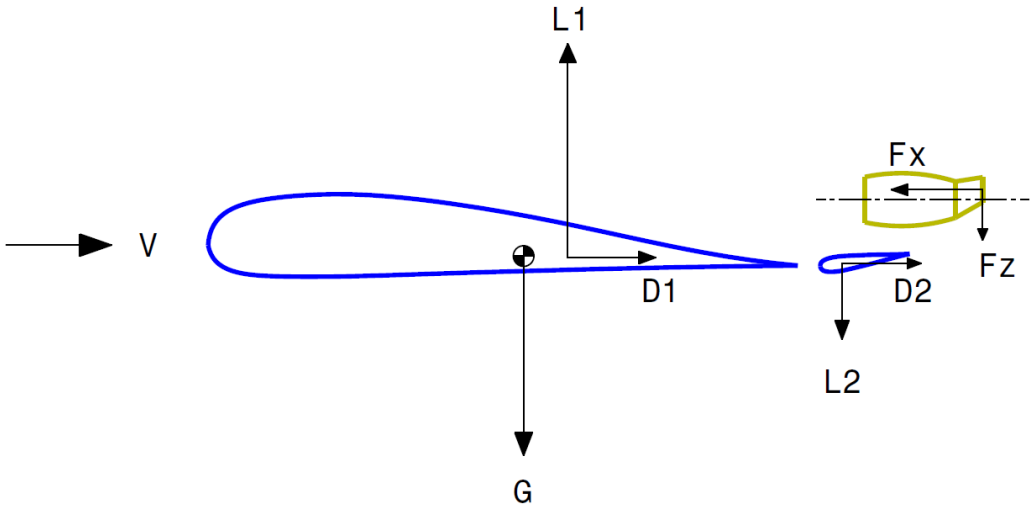

TU Delft Delft University of Technology
DLR
Challenge the future

Effectiveness of Thrust Vectoring Control for Longitudinal Trim of a Blended Wing Body Aircraft

by

Honglin Chen

in partial fulfillment of the requirements for the degree of

Master of Science

in Aerospace Engineering

at the Delft University of Technology,

to be defended publicly on Friday December 4, 2015 at 13:00.

-Thesis opportunity is provided by DLR

Supervisors: Dr.ir. Mark Voskuijl (Faculty of Aerospace Engineering, TU Delft)

Ir. Pier Davide Ciampa (Institute of Air Transportation Systems, DLR)

Thesis Registration Number: 064#15#MT#FPP

An electronic version of this thesis is available at http://repository.tudelft.nl/

DELFT UNIVERSITY OF TECHNOLOGY

DEPARTMENT OF

FLIGHT PERFORMANCE AND PROPULSION

The undersigned hereby certify that they have read and recommend to the Faculty of Aerospace Engineering for acceptance of the thesis entitled **"Effectiveness of Thrust Vectoring Control for Longitudinal Trim of a Blended Wing Body Aircraft"** by **Honglin Chen** in partial fulfilment of the requirements for the degree of **Master of Science**.

Dated: December 4th, 2015

Head of department:

Prof.dr.ir. Leo Veldhuis

Supervisor:

Dr.ir. Mark Voskuijl

Supervisor:

Ir. Pier Davide Ciampa

Reader:

Dr.ir. H.G. Visser

Summary

The Blended Wing Body configuration is a novel aircraft concept which has attracted the attention of aircraft designers for decades. This new configuration has several inherent advantages over conventional wing-fuselage configurations. Its characteristics of generating lift with all the aircraft components could result in a significant increment in aircraft cruise lift to drag ratio, and its smooth and tailless layout leads to a tremendous reduction of the wetted area hence friction drag compared to conventional designs. However due to the absence of a conventional tail, longitudinal stability and controllability become part of the key challenges of this configuration.

Thrust vectoring is a novel concept of control technology. It refers to the deflection of the engine thrust line in order to provide pitch, roll or yaw control moments or a direct lift force. Compared to conventional aerodynamic control surfaces, thrust vectoring control is less dependent on the dynamic pressure and is able to provide control moments at high angles of attack and post stall flight conditions. Therefore thrust vectoring technology has been applied on several military fighters to improve their maneuverability. The application of thrust vectoring on civil transport aircraft has only been studied by a few individuals. Quantified investigations need to be carried out to search for the potential benefits of the application of thrust vectoring control on a civil transport aircraft.

Based on the design challenges of the control power of a Blended Wing Body configuration and the possibility of controlling an aircraft with vectoring thrust, it is the objective of this thesis project to carry out quantified flight mechanics analyses on the effects and effectiveness of controlling a Blended Wing Body aircraft with vectoring thrust. As a starting point of investigating the application of thrust vectoring control with a novel civil transport aircraft configuration, flight mechanics simulations under steady symmetric level flight conditions are conducted in this project. A Blended Wing Body configuration from a European project is used as test case for thrust vectoring control.

Through this project a thrust vectoring model, which contains the calculation of nozzle deflection angles based on nozzle deflection controls and the calculation of engine thrust loss due to nozzle deflections, is developed and embedded in a flight mechanics toolbox used for the flight mechanics simulations. The flight mechanics simulations of thrust vectoring control are then carried out with a series of nozzle deflections, flight conditions, aircraft mass and CG locations. The influences of thrust vectoring on aircraft flight performance such as angle of attack, drag coefficient and engine fuel consumption etc. are analysed, and the control effectiveness of thrust vectoring and conventional aerodynamic control surfaces are compared based on the simulation results.

From the simulation results it is concluded that for the Blended Wing Body configuration tested in this project, thrust vectoring control under steady level flight conditions is much less effective than the conventional aerodynamic control surfaces. The maximum effectiveness ratio between thrust vectoring control and conventional aerodynamic control surfaces obtained in this project is about 11.2%. With extensive flight mechanics simulations and analyses, the way that aircraft flight conditions, mass and CG locations affect the effectiveness of thrust vectoring control is investigated through this project.

Acknowledgements

The thesis project presented in this report would not be possible to be accomplished without the help and support of a number of people.

Firstly, I wish to express my deepest gratitude to my two thesis supervisors, assistant professor Dr.ir. Mark Voskuijl from the Aerospace Engineering Faculty of Delft University of Technology, and Pier Davide Ciampa from the Integrated Aircraft Design Department of German Aerospace Center. Mark provided me the flight mechanics toolbox named Phalanx and developed by himself, without which it would not be possible to start the analyses conducted in this project. The valuable suggestions and feedback provided by Mark helped me to continue with the thesis project in the right direction. During my stay in the Integrated Aircraft Design Department of DLR, Pier helped me on every little problem I had in my project, and gave me enormous instructions and suggestions with his rich experience.

I would like to thank Björn Nagel who gave me the opportunity to finish my thesis project in his department, the Integrated Aircraft Design Department of DLR. I appreciate all the discussions and communications I had with the employees during my stay in this department. Their expertise and advanced research works have left me precious inspirations.

I wish to thank all my colleagues from AVIC especially from my department. Their help and support provided me a comfortable atmosphere for study. Many thanks for all the friends I met during my study in Europe. The friendship with these friends and the memory of this beautiful land is invaluable.

Finally, I would like to express my enormous gratitude to my family, especially my dear wife Liu Lei, for their unconditional and selfless support for my study abroad.

Honglin Chen

Delft, November 2015

Contents

List of Figures

List of Tables

Nomenclature

Roman letters

A	Nozzle section area	[m^2]
$\mathbf{B}$	Control effectiveness matrix	[——]
C_L	Lift coefficient	[——]
C_D	Drag coefficient	[——]
C_S	Side force coefficient	[——]
C_X	Force coefficient in X direction	[——]
C_Y	Force coefficient in Y direction	[——]
C_Z	Force coefficient in Z direction	[——]
C_{dw}	Wave drag coefficient	[——]
C_{fg}	Nozzle gross thrust coefficient	[——]
C_f	Flat plate skin friction coefficient	[——]
C_l	Rolling moment coefficient	[——]
C_m	Pitching moment coefficient	[——]
C_n	Yawing moment coefficient	[——]
D	Distance/Nozzle section diameter	[m]
F , T	Engine thrust	[N]
$\mathbf{F}$	Engine gross thrust matrix	[N]
$\mathbf{F}_S$	Pseudo force vector (including thrust)	[N]
FF	Form/Shape factor	[——]
$\mathbf{G}$	Ganging matrix	[——]
$\mathbf{H}$	Control allocation matrix	[——]
$[\mathbf{I}]$	Aircraft inertia tensor	[$kg \cdot m^2$]
L	Lift	[N]
L	Rolling moment	[N·m]
M	Pitching moment	[N·m]
M	Mach number	[——]
$\mathbf{M}$	Moment vector	[N·m]

M_{cr}	Critical Mach number	[——]
M_{DD}	Drag divergence Mach number	[——]
$\mathbf{M}_S$	Pseudo moment vector (including thrust)	[N·m]
N	Yawing moment	[N·m]
Re	Reynolds number	[——]
S	Area	[m^2]
TOP	Takeoff parameter	[——]
V	Airspeed	[m/s]
$\bar{V}$	Volume coefficient	[——]
W	Aircraft weight	[kg]
$\mathbf{W}$	Aircraft weight vector	[kg]
$\mathbf{a}$	Aircraft acceleration vector (for solving equations of motion)	[——]
b	Aircraft wing span	[m]
c	Airfoil chord length	[m]
$\mathbf{c}$	Aircraft control vector (for solving equations of motion)	[——]
$\bar{c}_{mac}$	Mean aerodynamic chord	[m]
d_{des}	Desired control variable	[——]
$\mathbf{d}$	Desired controlled variable vector	[——]
f	Friction factor	[——]
l	Moment arm	[m]
m	Threat of a fighter over its adversary	[——]
m	Mass	[kg]
$\dot{m}$	Mass flow rate	[kg/s]
p	Rolling angular rate	[°/s]
q	Pitching angular rate	[°/s]
r	Yawing angular rate	[°/s]
$\mathbf{r}$	Engine location vector	[m]
s_{TOFL}	Takeoff field length	[m]
t	Airfoil maximum thickness	[m]
u	Translational velocity in X direction	[m/s]

v	Translational velocity in Y direction	[m/s]
w	Translational velocity in Z direction	[m/s]
x	Pilot control input for aerodynamic control surface	[——]
$\mathbf{x}$	Aircraft state vector (for solving equations of motion)	[——]
y	Pilot control input for thrust vectoring	[——]

Subscripts

ACS	Aerodynamic control surface
TV	Thrust vectoring
a	Actual
a	Lateral control input
b	Longitudinal control input
e	Nozzle exit/Engine
g	Gross thrust
i	Ideal
n	nozzle
p	Directional control input
$pseudo$	Pseudo control
t	Nozzle throat

Superscripts

E	Effective
G	Geometrical

Greek letters

Γ	Circulation	[m^2/s]
Λ	Sweep angle	[°]
α	Angle of attack	[°]
α	Nozzle divergence angle	[°]

β	Sideslip angle	[°]
χ	Aircraft flight track angle	[°]
θ	Nozzle deflection azimuth angle	[°]
θ	Aircraft pitch attitude	[°]
ϕ	Aircraft roll angle	[°]
σ	Air density ratio	[——]
δ	Control Deflection	[°]
δ	Vortex strength along chordwise direction	[m^2/s]
$\dot{\delta}$	Control deflection rate	[°/s]
$\underline{\delta}$	Lower effective control position limits	[°]
$\overline{\delta}$	Upper effective control position limits	[°]
$\boldsymbol{\delta}$	Control effector deflection vector	[°]
γ	Vortex strength along wing spanwise direction	[m^2/s]
γ	Ratio of specific heat	[——]
γ	Flight path angle	[°]
$\boldsymbol{\omega}$	Aircraft angular rate vector	[°/s]
κ_A	Korn factor	[——]
ψ	Heading angle	[——]
$\dot{\psi}$	Turn rate	[°/s]
ε	Off-boresight angle	[°]
ξ	Deflection factor, Control effectiveness ratio	[——]
ω	Induced downwash velocity	[——]
η	Control allocation factor	[——]

Abbreviations

ACS	Aerodynamic control surface
ACTIVE	Advanced Control Technology for Integrated Vehicles
ALV	All Lift Vehicle
AMB	Aircraft main body
BWB	Blending Wing Body

CFD	Computational Fluid Dynamics
DA	Direct Allocation
DOC	Direct Operational Cost
DLR	German Aerospace Center
ENAC	Exhaust Nozzles for Aerocontrol
ETV	External Thrust Vectoring
FXP	Fixed-Point Iteration
HARV	High Angle of Attack Research Vehicle
IR	Infrared
ITV	Internal Thrust Vectoring
LP	Linear Programming
MATV	Multi-Axis Thrust Vectoring
MOB	Multidisciplinary Optimization of a Blended Wing Body
MDO	Multidisciplinary Optimization
MTOGW	Maximum Take-off Gross Weight
MTOW	Maximum Take-off Weight
MIT	Massachusetts Institute of Technology
NASA	National Aeronautics and Space Administration
OEW	Operation Empty Weight
ONERA	French National Aerospace Research Center
RCS	Radar Cross Section
SAX	Silent Aircraft eXperiment
S/VTOL	Short/Vertical Take-off and Landing
TOGW	Take-off Gross Weight
TV	Thrust Vectoring
TVC	Thrust Vectoring Control
USAF	United States Air Force
VELA	Very Efficient Large Aircraft
WPI	Weighted Pseudo-Inverse
ZEFT	Zero Emission Flying Testbed

1 Introduction

1.1 Project orientation

As stated in the Flightpath 2050 of the Europe's Vision for Aviation, the fuel efficiency of new aviation transports needs to be greatly improved compared to the capabilities of typical new aircraft in 2000, and CO_2 and NOx emissions need to be reduced by 75% and 90% respectively [1]. This ambitious goal needs tremendous improvements of the technologies applied on current transport aircrafts. To achieve this mission, several novel concepts of new aircraft configurations have already been studied and published on public sources.

A novel transport aircraft configuration called Blended Wing Body (BWB) configuration has great potential to improve the flight performance compared to current conventional wing-fuselage configurations. The BWB is a relatively clean layout. Wing and fuselage are connected smoothly. The fuselage is flat and shaped with particular airfoils, thus the fuselage of a BWB configuration also contributes to a large portion of the aircraft lift. A BWB configuration does not have a separate empennage. Maneuvering and trimming of BWB aircraft is achieved solely by trailing edge control surfaces of the main wings and center body. With the elimination of elevator and vertical tails, friction drag of this configuration could be reduced by a large portion due to a reduced wetted surface area. However, along with the elimination of traditional control surfaces the flight control system design becomes a significant challenge for BWB configuration. Compared to traditional horizontal tails, the moment arms of BWB trailing edge Aerodynamic Control Surfaces (ACS) are much shorter, and each ACS of a BWB configuration may be assigned to multiple functions. It is possible that the control surfaces on the trailing edge of main wing may saturate when multiple demands are sent to one single control surface [2].

A novel control technology called thrust vectoring which has been applied in the military aviation domain has the capability of improving the maneuverability and agility of aircraft, and provides the possibility for an aircraft to take-off and land in a short distance even vertically. Thrust vectoring is a novel technology of deliberately deflecting the directions of engine thrust during operation to provide control power for an aircraft. This cutting-edge technology has not been successfully applied on commercial aircraft despite some brief conceptual discussions conducted on its potential civil applications [3] [4] [5].

Thrust vectoring application is possible to reduce the difficulty of flight control system design and achieve a certain magnitude of flight performance improvements for a civil transport aircraft, especially for a BWB configuration which is essentially lack of control power. Flight mechanics analyses on thrust vectoring control with a BWB configuration are therefore proper approaches to investigate the effects and effectiveness of thrust vectoring control, and to make comparisons between the control effectiveness of thrust vectoring and conventional ACS.

1.2 Research objectives and questions

This thesis project is aiming to carry out flight mechanics analyses on thrust vectoring control with a BWB configuration. The implementation of thrust vectoring in a flight mechanics analysis environment is important to study the quantified effects and benefits of this novel technology. Several projects of thrust vectoring application on military aircraft have been conducted in the past few decades. Results from numerical simulations and flight tests of thrust vectoring control on military aircraft show that for military fighter aircraft thrust vectoring control is helpful to improve the maneuverability and post-stall controllability and provide the possibility of short/vertical takeoff and landing. Application of thrust vectoring on civil aircrafts has only been analyzed by a few individuals at a conceptual level. Implementation of thrust vectoring in a flight mechanics analysis environment can be a cost-saving approach to investigate thrust vectoring control on a civil transport aircraft. As a starting point of investigating the quantified effects and effectiveness of thrust vectoring control on a civil transport aircraft, thrust vectoring control simulations under symmetric steady flight conditions are conducted in this project.

In order to carry out the flight mechanics analysis proposed above, relevant information for the flight mechanics calculation needs to be prepared first. The information needed includes: the aerodynamic performance database, the control derivatives of the ACS, and the mass and inertia of the analyzed aircraft, as well as the engine performance map with thrust vectoring effects. Different tools need to be utilized to get the mentioned aircraft information. A flight mechanics toolbox is also needed to carry out the flight mechanics calculation.

A BWB configuration is chosen as the test platform of thrust vectoring controls. This novel configuration has potential advantages on its high lift to drag ratio, high cabin capacity over conventional configurations. However the lack of a conventional empennage results in a critical challenge of its flight control system (FCS) design. The relative short moment arms of the wing trailing edge control surfaces of BWB lead to a possible lack of control power. Therefore it is appropriate to study the effects of thrust vectoring control on a BWB configuration to see if this new control technology is helpful to contribute to the solution of the control power deficiency of a BWB design.

The flight mechanics analysis work of thrust vectoring control on a BWB configuration is confined to longitudinal steady level flight conditions in this project. The BWB aircraft is controlled either purely by ACS or by combined controls of wing trailing edge ACS and vectoring thrust. Parameters of the trimmed flight conditions are calculated under different control settings. Based on the calculated results comparisons can be made between the aircraft flight performance with pure conventional controls and the aircraft performance with combined controls, and conclusions can be made on the effects and effectiveness of thrust vectoring control on a BWB under steady level flight conditions.

The main research question to be answered at the end of this project is: What are the effects of thrust vectoring control on a BWB configuration under steady trimmed flight conditions? To reach the answer of this question, the following sub-questions need to be answered:

- How to model thrust vectoring in an analytical way and implement the modeling in a flight mechanics analysis environment?
- How should thrust vectoring controls and conventional aerodynamic controls be integrated for the flight mechanics analyses?

- What are the effects of thrust vectoring control compared to conventional control power? How effective is it?
- Which of the factors concerned in the conditions of flight mechanics simulations of this project have influences on the effectiveness of thrust vectoring control?

1.3 Project structure

The first step of this project is to determine an algorithm of thrust vectoring modeling for flight mechanics analysis. The modeling of thrust vectoring is in fact a process of counting the thrust loss due to nozzle deflection, and calculating the effective deflection angle of vectoring thrust based on the geometrical nozzle deflection angle. The modeling of thrust vectoring needs to be integrated with a flight mechanics analysis environment in order to take into account instantaneously the thrust vectoring effects during flight mechanics analyses. An analytical solution of calculating the thrust loss due to nozzle deflection, as well as the calculation of effective thrust deflection angle based on geometrical nozzle deflection angle, is developed by Erich Wilson [6]. This analytical solution is used in this thesis project for the conceptual modeling of thrust vectoring performance.

A flight mechanics toolbox called Phalanx (Performance, Handling Qualities and Loads Analysis Toolbox), developed by Mark Voskuijl, is used for aircraft flight mechanics analysis. Phalanx is a selective fidelity flight mechanics modeling and analysis tool based on multi-body dynamics. It enables the user to seamlessly integrate sub models from various aerospace disciplines in a single full nonlinear aircraft model. The toolbox is written in Matlab and make extensive use of the Simulink® platform.

Before running the flight mechanics analysis when thrust vectoring modeling has been successfully constructed and implemented in the flight mechanics toolbox, a second step of the thesis project is that all the required inputs of the flight mechanics toolbox need to be prepared. The inputs of Phalanx for steady state trim calculation include the aerodynamic performance database of the chosen aircraft configuration, the control derivatives of all the aerodynamic control surfaces, the engine performance map, and the mass and inertia of the aircraft. Proper tools for every set of the required inputs are used to calculate the required information. The flight mechanics analysis of thrust vectoring control in this project with conceptual fidelity level hence the tools utilized for inputs preparation are with low fidelity.

This thesis project is accomplished at the Department of Integrated Aircraft Design, Institute of Transportation Systems of the German Aerospace Center (DLR). A BWB configuration from the European VELA (Very Efficient Large Aircraft) project [7] is provided by DLR as the test platform of this thesis project. It is the second version of the BWB configuration developed in the VELA project and therefore is named as VELA2. The geometrical model of VELA2 used for this thesis project is initially with no vertical tails. However since this thesis project is focusing on thrust vectoring control simulations in longitudinal plane, the absence of vertical tails has no significant influence on the results. The four original wing mounted turbofan engines of the initial VELA2 configuration are relocated to the trailing edge of the center fuselage in order to increase the moment arms of vectoring thrust and maximize the effectiveness of thrust vectoring control. The original VELA2 configuration developed in the European VELA project as well as the modified VELA2 configuration used as the test platform in this thesis project are shown in Figure 1-1.

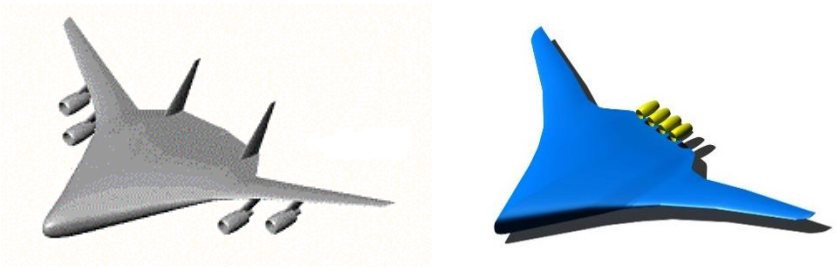

Figure 1-1 Original VELA2 (left) and modified VELA2 (right) configurations

When the inputs of Phalanx are prepared with the chosen aircraft configuration and used tools, a flight condition with altitude of 9000 meters and Mach number of 0.6 is taken as the first analysis point of thrust vectoring controls. Only steady symmetric level flight conditions are analyzed in this project for the first exploration of thrust vectoring control with a civil BWB configuration. Since the effects and effectiveness of thrust vectoring control on the chosen BWB configuration is not clear at the current stage, the vectoring nozzles and ACS are therefore controlled separately in order to compare the control effectiveness of thrust vectoring with the effectiveness of conventional ACS control. An arbitrary position limit of nozzle deflections is set to be ±20° as shown in Figure 1-2. Under a specified flight condition, vectoring nozzles are manually deflected from -20° to +20° with a step length of 2°. The definition of nozzle deflections in longitudinal plane is similar to the definition of conventional ACS: for an aircraft with engines mounted aft the Center of Gravity (CG) of the aircraft, deflections with nozzle exit section down are positive, producing nose down pitching moments w.r.t. the aircraft CG. In the contrast, deflections with nozzle exit up are defined as negative when nose up pitching moments are produced by thrust vectoring nozzles. At every nozzle deflection setting, the trim condition of the aircraft is calculated by Phalanx by searching for proper deflections of the aerodynamic control surfaces, and the respective angle of attack of the aircraft to reach a trimmed flight condition. The results with different nozzle deflections are compared with the results of zero nozzle deflections, and the effects and effectiveness of thrust vectoring controls can be observed from the comparisons.

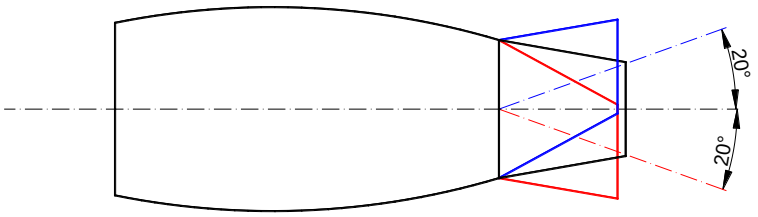

Figure 1-2 Range of vectoring nozzle deflections

When thrust vectoring control at a single flight condition is simulated, the next step of this thesis project is to carry out similar simulations on various flight conditions by changing the flight altitude and Mach number, aiming to examine the influences of flight conditions on thrust vectoring effects. In this project flight conditions with 4 different altitudes are examined, varying from 0 km to 9 km with a step length of 3 km. At every flight altitude different flight Mach numbers are considered. The distribution of flight conditions in a simplified flight envelop of a civil aircraft is shown in Figure 1-3. There are in total 19 flight conditions analyzed. Under every specified flight condition, steady trim

conditions are calculated with vectoring nozzles deflected from -20° to 20° with a step size of 2°. Comparisons on thrust vectoring effects can be made from the results of different flight conditions.

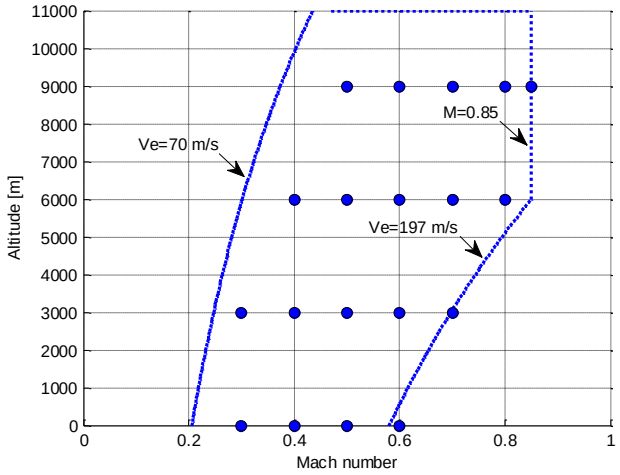

Figure 1-3 Flight conditions analysed

The operational empty mass (OEM) and the respective CG is taken for the analyses of all the flight conditions mentioned above. In fact the location of CG and the magnitude of aircraft mass also have influences on the trimming and control of an aircraft since these two parameters determine the moments required to be balanced. In order to not only focus on the influences of flight conditions but also the influences of the interior properties of the aircraft on thrust vectoring control, the CG and aircraft mass is varied for a broader exploration on factors that have influences on thrust vectoring control. The CG range is calculated based on statistic CG ranges of civil transports. Based on statistics data the CG location of a transport aircraft with 3 or 4 engines may travel forward and aft by a range of up to 22% of its mean aerodynamic chord (MAC) as shown in Figure 1-4 [8].

	AIRPLANE TYPE	C.G. LIMITS, PER CENT M.A.C.						PAY-LOAD	$\frac{S_h \ell_h}{\bar{S}c}$	hor. tail type **	$C_{L_{max}}$ ***
		FORWARD		REAR		RANGE					
		takeoff landing	flight	takeoff landing	flight	takeoff landing	flight	% OEW			
2 JET ENGINES	Aerospatiale Corvette SN601	-	20.0	-	36.0	-	16.0	28.3	.64	V	2.40
	A.C. Jet Commander 1121	20.0	20.0	36.0	36.0	16.0	16.0	20.6	.64	F	1.66
	Lear Jet 25	9.0	9.0	30.0	30.0	21.0	21.0	35.6	.64	F	1.39
	H. Siddeley HS-125 1A/1B	18.0 *	18.0 *	37.5 *	37.5 *	19.5 *	19.5 *	14.0	.69	F	2.44
	Dassault Mystère 20F	14.0	16.0	28.5	28.5	14.5	12.5	23.1	.66	V	2.30
	H.F.B. Hansa	13.0	11.7	23.0	21.7	10.0	10.0	30.9	.71	F	2.00
	Fokker VFW F-28 Mk1000	18.0	17.0	35.0	37.0	17.0	20.0	42.0	.97	V	2.53
	BAC 1-11 Srs. 400	15.0 *	14.0 *	39.0 *	41.0 *	24.0 *	27.0 *	35.3	.85	V	2.38
	Sud. Av. Caravelle 10R	25.0	25.0	41.5	41.5	16.5	16.5	32.3	.56	F	2.10
	McD. Douglas DC-9/10	16.3	15.0	39.0	40.0	22.7	25.0	42.4	1.15	V	2.40
	DC-9/33F	5.9	3.1	34.7	34.7	28.8	31.6	70.8	1.18	V	2.98
	Boeing 737/100	15.0	15.0	35.0	35.0	20.0	20.0	49.4	1.14	V	3.10
	Airbus A-300 B2	11.0	11.0	31.0	31.0	20.0	20.0	37.4	1.07	V	2.65
3 OR 4 JET ENGINES	Lockheed 1011 Tristar	-	12.0	-	32.0	-	20.0	36.1	.93	A	2.57
	Boeing 707/120	16.0	16.0	34.0	34.0	18.0	18.0	38.2	.61	V	1.86
	720/022	15.0	15.0	31.0	31.0	16.0	16.0	31.9	.59	V	2.26
	747/200B	-	12.5	-	32.0	-	19.5	45.8	1.00	V	2.55
	McD. Douglas DC-8/21	16.5	16.5	32.0	32.0	15.5	15.5	27.0	.58	V	2.10
	Lockheed C-141A	19.0	19.0	32.0	32.0	13.0	13.0	50.3	.51	V	2.32
	Lockheed C-5A	19.0	19.0	41.0	41.0	22.0	22.0	67.9	.64	V	2.60

Figure 1-4 CG location limits of jet transport aircrafts [8]

A CG range of 18% Mean Aerodynamic Chord (MAC) is then chosen based on statistic data. Unlike most conventional transport aircrafts with only positive static margin, a 9% MAC of negative static margin and a 9% MAC of positive static margin is evenly allotted for the CG range of the modified VELA2 used in this project, in order to investigate both the influences of negative and positive static margin on thrust vectoring controls. As shown in Figure 1-5, the CG of the VELA2 configuration with OEM mass is calculated to be at 34.23 from the nose of the aircraft on longitudinal symmetrical plane, while the aerodynamic center of the aircraft is calculated to be at 35.43 m from the aircraft nose. With 9% MAC of negative static margin and 9% MAC of positive static margin, the respective CG locations from the aircraft nose point in the longitudinal symmetrical plane is 32.19 m and 38.67 m.

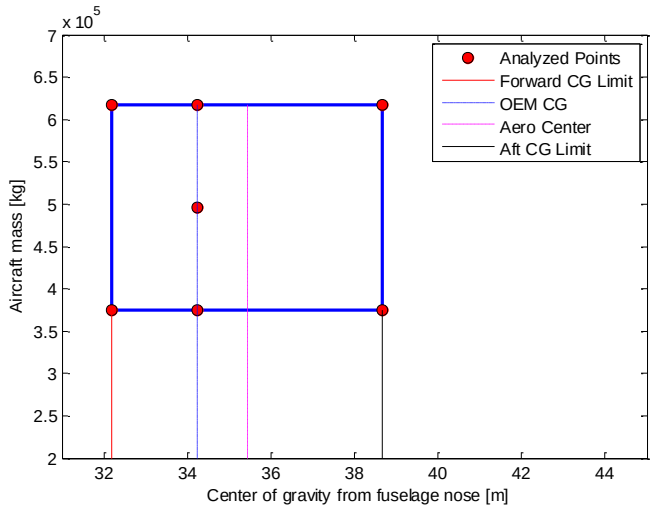

Figure 1-5 Variation of CG and mass

The mass variation of the VELA2 aircraft is accomplished by varying the fuel and payload mass from zero fuel and payload mass to half of the fuel and payload mass, and then the full fuel and payload mass (the respective Maximum TakeOff Mass, MTOM) as shown in Figure 1-5. In total 7 CG and mass combinations are tested. For every mass and CG combination all the flight conditions shown in Figure 1-3 are simulated, and for every flight condition point the trimmed conditions are calculated with nozzle deflections varying from -20° to 20°. Therefore there are 2660 combinations of the mass and CG conditions, the flight conditions, and the nozzle deflection angles calculated in this thesis project.

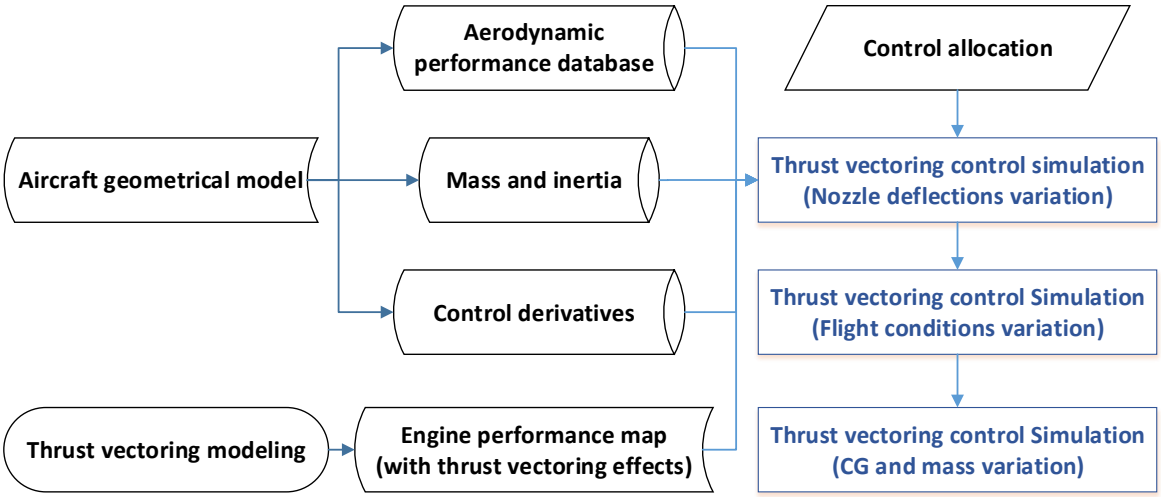

Figure 1-6 Structure of the thesis project

A brief process and structure of the thesis project is shown in Figure 1-6. With the geometrical model of the VELA2 aircraft provided by DLR, the aerodynamic performance database, control derivatives, mass and inertia of the aircraft can be estimated with a series of tools. A thrust vectoring model is constructed with the selected algorithm in this project and is integrated with an existing engine performance map. With proper control allocations of the aerodynamic control surfaces and vectoring nozzles, the aerodynamic forces and moments produced by all the aircraft components as well as the thrust forces and moments produced by vectoring nozzles can be calculated under a specified flight condition. Then the trim condition can be solved with Jacobian algorithm used in Phalanx. When all the required inputs for trimming the VELA2 aircraft with Phalanx are prepared, thrust vectoring control investigations are then carried out with various nozzle deflections, flight conditions as well as aircraft CG and mass conditions. The effectiveness of thrust vectoring control for longitudinal trim of a BWB aircraft is therefore extensively investigated through the process given in Figure 1-6.

2 Background information

Two novel disciplines, the BWB configuration and the thrust vectoring technology, are integrated through this project. This chapter gives a brief insight into the history and basic characteristics of these two new concepts and provides summaries on the benefits and shortcomings of the two disciplines.

2.1 Blended wing body

The current common layout of a Blended Wing Body configuration is originated from a collaborative study among McDonnell Douglas Corporation[1] and several American Universities, funded by the Langley Research Center of the National Aeronautics and Space Administration (NASA). McDonnell Douglas took the idea of flying wing airplanes as the initial point of a new transport aircraft, which integrates engines, wings and fuselage of an aircraft into a unified All Lift Vehicle (ALV) to maximize the overall efficiency [9]. Although the resulted layout of McDonnell's study, the Blended Wing Body configuration, looks highly relevant to the concept of the early flying wing models such as the Northrop YB-35 and YB-49, the preliminary configuration concept of McDonnell's project was far away from either a typical modern BWB configuration or a typical flying wing configuration. The Northrop YB-35 and YB-49 aircrafts were for new technology tests and did not have strong requirement on passenger capacity and therefore was able to implement a pure flying wing configuration without typical fuselage component. The McDonnell's study was aiming at a long range transport aircraft, thus at the beginning of the study a hoop shaped fuselage was chosen, concerning its efficiency of taking cabin pressure and emergency egress. However this constraint leads to a conventional combination of fuselage and wings. Consequently the requirement of a hoop fuselage was abandoned and the initial design gradually resulted in a new configuration concept, namely the first generation BWB configuration as shown in Figure 2-2 [10].

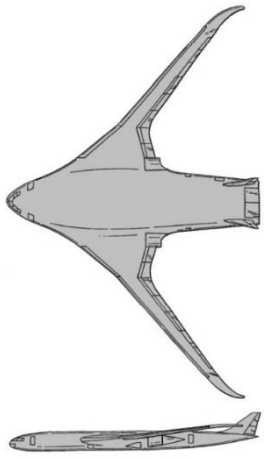

Figure 2-1 Early blended configuration concept, figure from [10]

[1] Merged with Boeing at 1 August 1997

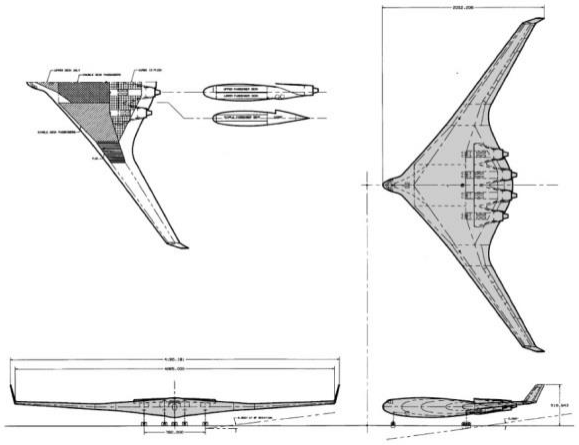

Figure 2-2 First-generation BWB, figure from [10]

2.1.1 Historical aspects of ALV

From the emerging process of the first generation BWB and the classification of ALV by Richard M. Wood [11], BWB configuration can be considered as a new member of ALV family. The germination of BWB concept has been doubtlessly inspired by the early researches conducted on ALV configurations, therefore it is necessary to first address some brief information on the history of ALV researches. Based on Richard M. wood's classification ALV family can be mainly sorted into two categories: Flying Wing and Flying Fuselage concepts. The Flying Wing concept can be further sorted into All-Wing concept and Tailless concept, while the Flying Fuselage concept can be further classified as Lifting Fuselage and Lifting Body. Each of the above concepts will be illustrated by some early designs in the following sections.

Development of ALV can date back to the beginning of manned aviation technologies at the end of 19th century. Over a century has passed since the first introduction of ALV concept. However after a century of research on this concept, ALV is still considered to be an unconventional configuration and not accepted or utilized for transport aircraft. The main reason for this delay of acceptance is the control and stability problem, and the resistance of conventional-minded shareholders and publics according to the observations of A. R. Weyl and Richard M. Wood [11] [12].

The history of ALV configurations can be generally separated into two periods, the pre-1950s era and the post 1950s era. The pre 1950s period was the golden period of ALV configuration development when several countries such as Germany, England, France, as well as America, took their individual researches on this subject. During this period a number of ALV concepts were developed and tested. Since mid-1950s most of the development work on ALV technologies has moved from Europe to America. The main focus of investigations has also switched from various configuration concepts to mainly lifting body configurations as used for space shuttles, as well as flying wing configurations as used for military attackers and bombers. It is hard to address all the contributors to ALV developments and is not the focus of this report, a few prominent individuals, institutes and corporations on the research and development of several typical ALV concepts will be illustrated in the order of different countries. The collection of these illustrations is mainly based on the historical review of ALV concepts

carried out by Richard M. Wood. Because the researches on ALV concepts during the pre-1950s era were mainly carried out by different individuals, the review on this history is categorized by individual researchers, while the brief description of ALV development in the post 1950s era is categorized in different institutes or companies.

2.1.1.1 The pre-1950s researches on ALV

Manned aviation history started with studying natural species and got inspiration from observation from Zanonia seeds gliding and birds flying. Early pioneers on aviation researches carried out their airplane designs by imitating those natural phenomena. Among those pioneers, Otto Lilienthal is believed to be the "father of flight". He was the first person to make successful manned gliding flights. Lilienthal built several gliders and made a number of controlled gliding flights. His gliders primarily contain bionic wings inspired from studies on plant seeds and birds. The American aviation pioneer Octave Chanute also built several biplane gliders based on Lilienthal's design. His systematic survey on fixed-wing heavier-than-air aviation research and his book "Progress in Flying" had non-negligible influence on the progress of early aviation development. Even though gliders developed by these early aviation pioneers are not pure flying wings, they are believed to be the inspiration of later flying wing researches [13].

a. Lilienthal's glider

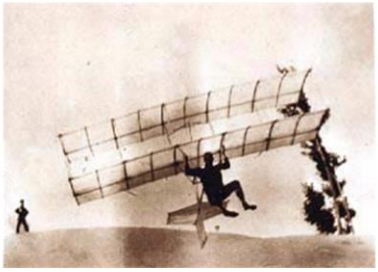

b. Chanute's glider

Figure 2-3 Early photos of gliding attempts

Empennage is not the intension of aircraft design. It was when the controllability and stability problems became clear to early aviation scientists that tails were forced to be added to their designs. Among those early aviation explorers a French engineer Clement Ader developed his bat-like steam engine powered aircraft in 1890s. Some typical features of a powered manned flying wing aircraft could already be found from this early attempt. Another British aeronautical engineer John William Dunne was also interested in tailless aircraft design during 1900s and 1910s. He began his research on aviation engineering by constructing tailless gliders in the early 1900s which was turned into powered tailless aircrafts later. Most of Dunne's tailless aircrafts were biplane configuration, which also features some typical characters of a flying wing configuration. Following Dunne's work anther British aviator Geoffrey Terence Roland Hill designed and tested several tailless aircrafts, called Pterodactyl, with monoplane configuration. Another member of the early ALV family which should not be neglected is the lifting fuselage concept which was carefully studied by an American aeronautical engineer Vincent Justus Burnelli. His focus was on the configuration with airfoil shaped fuselage and conventional wings.

Despite the tails kept on his models, he still contributed to the concepts of ALV family by designing the fuselage as part of lift generators [11].

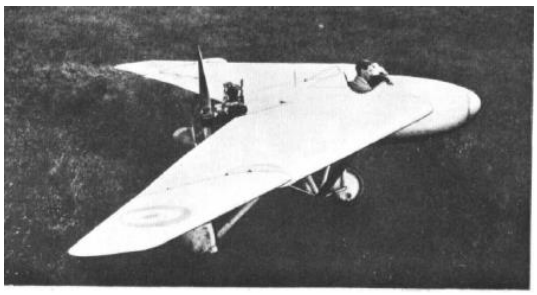

Figure 2-4 Hill's monoplane tailless aircraft: Pterodactyl 1A

Figure 2-5 Burnelli's lifting fuselage configuration: UB-14

Even though it is difficult to draw a clear line for ALV configurations between early attempts and the later typical ALV aircrafts, it can be told that most of the early designs as mentioned above have more or less some parts not generating lift, such as the tails in Lilienthal's gliders and fuselages in Hill's monoplane tailless aircrafts. The most prominent designers and researchers on the later typical flying wing developments and studies are the Horten Brothers from Germany and Jack Northrop from America. Both conducted their developments around the 1930s and 1940s. Horten Brother's first aircraft was a flying wing glider. Later on they began their development on powered flying wing researches. Their outcome, the Ho-229, is the first jet powered flying wing aircraft. The American aviation industrialist and designer Jack Northrop is doubtlessly one of the prominent pioneers in American flying wing aircraft design history. Northrop dedicated most of his lifetime to the research and development of advanced flying wing aircrafts. The representatives of his achievements are the YB-35 and YB-49. The well-known strategic bomber B-2 has inherited several concepts from Northrop's researches.

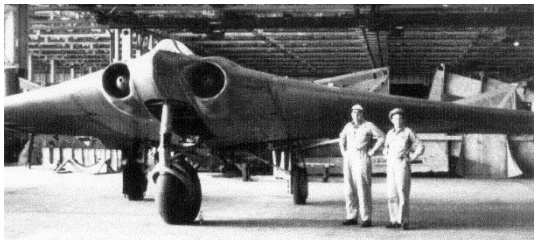

Figure 2-6 Horten Brother's flying wing concept: Ho-229

Figure 2-7 Northrop's flying wing concept: YB-49

Part of the pre-1950s prominent contributors of ALV concepts are listed in Table 2-1.

Table 2-1 Part of Pre-1950s main contributors to ALV development

Name	Country	Years of Research on ALV	Representatives
Otto Lilienthal	Germany	1870s-1896	Manned gliders
Octave Chanute	America	1880s-1900s	Biplane hang gliders
Clement Ader	France	1880s-1900s	Avion Ⅲ
John William Dunne	Britain	1900s-1910s	D.1 - D.10
Alexander Lippisch	Germany	1920s-1930s	Storch Ⅰ - Storch Ⅸ
Vincent Burnelli	America	1920s-1940s	KB-1, CB-16, UB-14, XCG-16, CBY-3
Geoffrey T.R. Hill	Britain	1920s-1950s	Pterodactyl
Horten Brothers	Germany	1930s-1940s	Ho 229
Jack Northrop	America	1940s	N-1M, N-9M, YB-35, YB-49

2.1.1.2 The post 1950s researches on ALV

According to Richard's overview on ALV development history, the interests in flying wing encountered a decline during the 1960s and 1970s, and the dominance of flying wing researches has moved from Europe to America since this period. The researches on ALV in America were mainly focused on two fields from 1960s to 1980s instead of various concepts. One of the interests was the development of space shuttle for which lift body configuration was used. The other focus was the flying wing configuration. When enormous researches had been carried out in the pre-1950s period, the achievements of ALV design were not successfully converted into industrial production in the following 1960s and 1970s. One main reason was the inadequate controllability and stability of this configuration without the help of fly-by-wire system as well as a computer aided design of meticulous aerodynamic shape. It was during this stagnant period of ALV development that the fly-by-wire technology was developed. Therefore in the 1980s and 1990s there was a new beginning of ALV design interests when the well-known flying wing tactical attacker F-117 and strategic bomber B-2 were revealed to the public [11].

a. Space shuttle
Picture: NASA

b. F-117
Picture: Lockheed Martin

c. B-2
Picture: Northrop Grumman

Figure 2-8 Representative industrial applications of ALV in the post 1950s

Except for the industrial production of flying wing aircrafts as listed above, there are several ongoing military combat aircraft projects which implement the concept of ALV configurations, mainly flying wing configurations. Some examples of these future combat aircrafts are the Boeing X-45, the Northrop Grumman X-47B, the BAE Systems Taranis and the European nEUROn.

a. X-47B
Picture: Northrop Grumman

b. TARANIS
Picture: BAE Systems

c. nEUROn
Picture: Dassault Aviation

Figure 2-9 UCAV demonstrators with ALV configurations

2.1.2 Recent commercial BWB researches

After a century of development on flying wing aircrafts, the advantages of the ALV configuration have been widely accepted. The challenges of designing this novel configuration for civil applications, mainly aerodynamic design, cabin arrangement, structure design of the center body, stability and controllability aspects, are likely to be resolved with new technologies developed in the post 1950s era. Industrial productions of flying wing configuration can already be found in military applications such as the American F-117 and B-2, but commercial applications are still not achieved. Industry, research institutions and academic groups have carried out a series of researches and developments on civil applications of ALV configurations, namely the BWB configurations. In the late 1980s NASA funded a research project to conduct studies on alternative configurations for future long-haul transport aircrafts. This research work at McDonnell Douglas Corporation led to an early blending configuration. However the consideration of a hoop shaped fuselage to take the hoop tension put a restriction on the aircraft design and resulted in a conventional fuselage and wing combination. The later abandonment of the hoop fuselage resulted in the first generation of BWB configuration [10]. The layout of the resulted BWB concept could be viewed as an optimization of early flying wing concept and lifting fuselage concept, while inheriting the advantages of flying wing concept and ensuring the

cargo capabilities of a transport aircraft simultaneously. Under the guidance of requirements of future aviation transport systems such as the European Aviation 2050, and with the inspiration of BWB advantages revealed from Boeing's project, several research groups have carried out their own BWB researches with varying emphases.

2.1.2.1 BWB researches at Boeing

Boeing's BWB program originated from McDonnell Douglas's researches on blending configuration. The orientation of this project is to integrate new technologies, including blended wing body layout, in a novel commercial transport aircraft design, with primary design requirements of maximum 800 passengers, maximum range of 7000 nm, and cruise Mach number of 0.85 [10]. The first researches were focusing on the aerodynamic shape design while considering payload capabilities. For comparison, an aircraft with conventional configuration of the same design requirements were designed simultaneously since there is no BWB aircraft already in production for reference. The preliminary study of this project has already indicated significant improvements of the aircraft performance over the conventional design.

The emergence of Blended Wing Body concept was based on the reduction of surfaces area while keeping equivalent inner cabin volume, hence reduce the wetted area by up to 33%. This could in turn increase the cruise lift to drag ratio of the configuration.

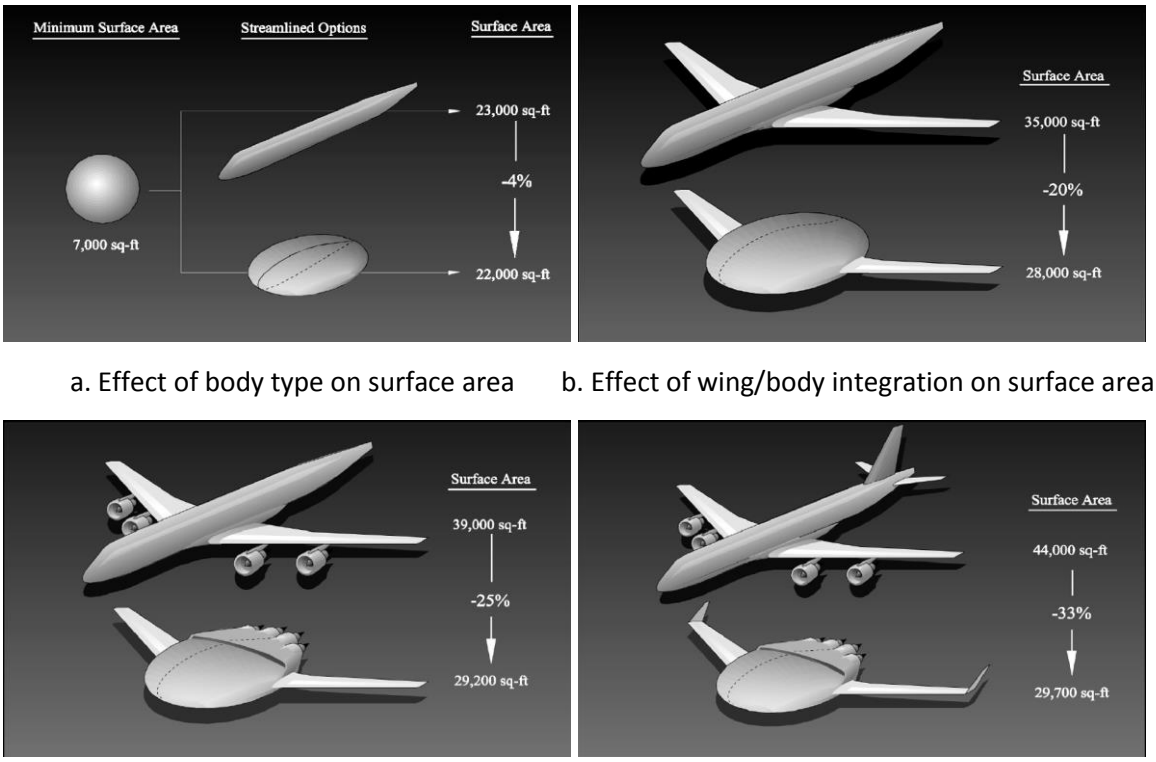

a. Effect of body type on surface area b. Effect of wing/body integration on surface area

c. Effect of engine installation on surface area d. Effect of controls integration on surface area

Figure 2-10 Genesis of BWB concept [10]

Like other aircraft configurations, BWB concept has a process of emergence. The project of advanced technology subsonic transports at McDonnell Douglas funded by NASA Langley Research Center was

first focusing on designing a blended configuration with circular passenger cabin to take the cabin pressure. The cylindrical cabin constraint resulted in a conventional design and this constraint was therefore abandoned. The project gradually resulted in the first generation of BWB concept as shown in Figure 2-2. The performance improvements of Boeing's first generation BWB design over the conventional design with the same design requirements are listed in Table 2-2.

Table 2-2 Brief performance improvements of Boeing's BWB project [14]

Item	Changes over conventional configuration
L/D	21%
MTOGW	-15%
OEW	-12%
Fuel Burn	-28%
Total SLST	-27%

With the significant improvements of the aircraft performance during the first generation BWB project, a subsequent project was followed by a NASA/industry/university team in 1994. During this second generation BWB project emphases of the research work included:

- Upgrading the aerodynamic layout of the aircraft
- Wind tunnel tests for CFD results validation
- Stability and control analysis for control surfaces design
- Flight demonstrator for low speed flight mechanics exploration
- Propulsion integration investigation for satisfactory engine performance as well as aircraft aerodynamic performance
- Structure design for this novel configuration especially the passenger cabin structure of the center body
- Safety and environment aspects, such as noise production, when the arrangement of aircraft components are different from conventional designs
- Performance evaluation by comparing with a conventional subsonic transport design with the same design mission, and implementing the same advanced technologies

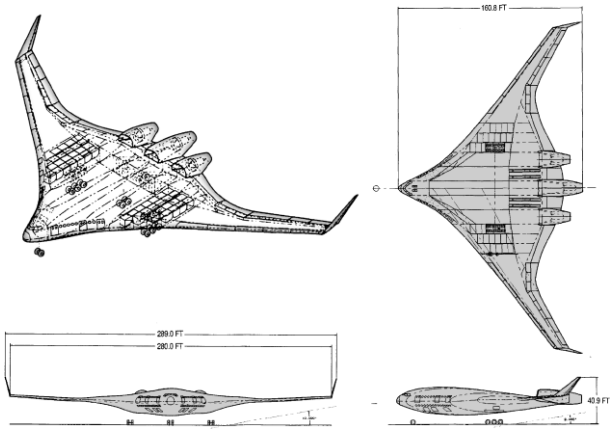

Figure 2-11 Boeing's second generation BWB [10]

After 3 years of the second generation BWB project, Boeing conducted a BWB-450 project. This project was mainly initiated from the fact that the previous first and second generation BWB project were with large scale and were not possible to make comparisons with existing aircrafts for validation. Three main characters of BWB-450 project are

- Multidisciplinary optimization was implemented for minimum TOGW
- A positive static margin was achieved without drag penalty by careful wing design
- Podded engines were chosen instead of embedded engines to reduce technology risks

Boeing's unprecedented and radical researches on a modern civil all lift transport configuration, the BWB concept, has started a new era of various researches on this novel configuration. Several projects have been launched by various industries, institutes and universities on studying various disciplines of BWB concept, aiming to a have a comprehensive understanding on all the critical topics and facilitate the industrial applications of the BWB configuration.

2.1.2.2 European MOB project

The European MOB (Multidisciplinary Optimization of a Blended Wing Body) project was mainly aiming on the development of a system of integrating different tools from various institutions and countries for multidisciplinary design and optimization of complicated aircraft configurations. Demonstrating the tool system was accomplished by implementation on a novel BWB design which requires multiple tool integration and multidisciplinary optimization [15]. Therefore with the development of the MOB project a BWB aircraft was designed for testing the tool system. The basic concept of the BWB aircraft from the MOB project came from a design from Cranfield University. This initial design was a commercial transport aircraft which required a set of strict considerations on airworthiness restrictions. To simplify the problems of the MOB project, the BWB configuration was therefore switched into a freight aircraft. Multidisciplinary optimization was implemented in the demonstration of the tool system as well as the design of aircraft [16].

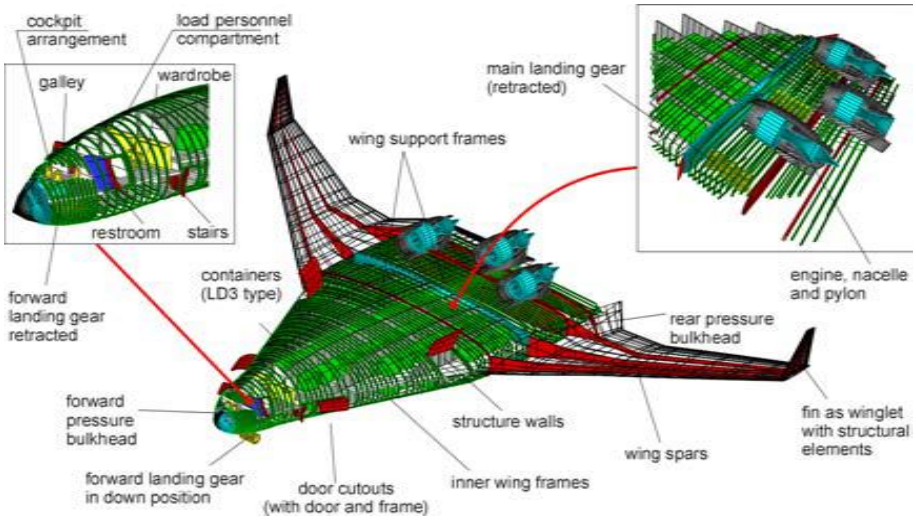

Figure 2-12 BWB aircraft from the MOB project [16]

2.1.2.3 European VELA project

Another European BWB project, the VELA project, was focusing on investigations on several disciplines of BWB configuration including initializing of the base configuration, aerodynamic shape optimization, stability and control, structure design, interior cabin design, and integration of all the disciplines mentioned above. These disciplines cover the most important topics of a novel BWB configuration [17].

Table 2-3 Work packages of the VELA project [7]

Work package	Objectives
Configuration setup	Develop three reference configurations with the same design requirements, including one conventional configuration and two BWB configurations. The conventional configuration is used for BWB design validation and comparison. The two BWB configurations differs on the level of blending between center body and outer wing, as well as the longitudinal position of wings w.r.t the center body.
Aerodynamic shape optimization	Identify the relevant parameters for aerodynamic optimization and maximize lift over drag ratio for a particular flight condition point. Provide aerodynamic loads for structure work package and stability analysis.
Stability and control	Define the stability and control requirements, analyse the stability and control characters of this novel configuration through both theoretical and experimental aerodynamic data.
Structural solutions	Define different solutions for primary structure solutions, perform FEM structure analysis and establish preliminary BWB weight breakdown.
Payload accommodation	Define reference cabin arrangements, analyse evacuation time requirements and provide solution to fulfil the evacuation time limits.
Integration assessment exploitation	Implement the findings from work package 2 and 5, define a new BWB configuration.

During the VELA project two initial BWB configurations were designed in work package 1, namely the VELA1 and VELA2 configurations as shown in Figure 2-13. The VELA1 configuration has high wing mounted at the front part of the center fuselage with a sharp side wall and a fuselage-like cockpit nose. The VELA2 configuration has a middle wing mounted at the rear part of the center fuselage with higher level of wing fuselage blending. Based on the findings and recommendations from the work packages of this project, a series of refined configurations were developed based on VELA1 and VELA2 configurations. In the last work package a refined interpolated configuration, the VELA3 shown in Figure 2-14, was constructed by implementing and interpolating the results obtained from work

package 1 to 5 with a high wing mounted around the central longitudinal location of the center fuselage [7].

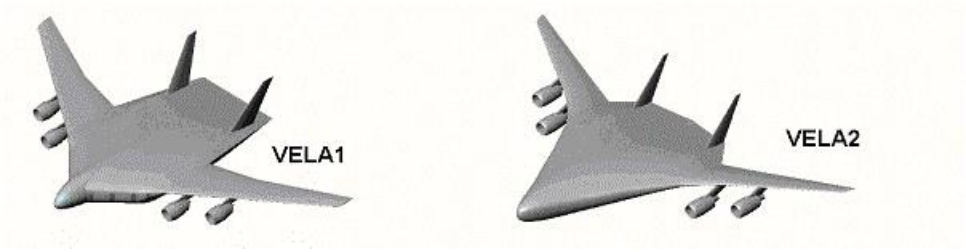

Figure 2-13 VELA1 and VELA2 configurations [7]

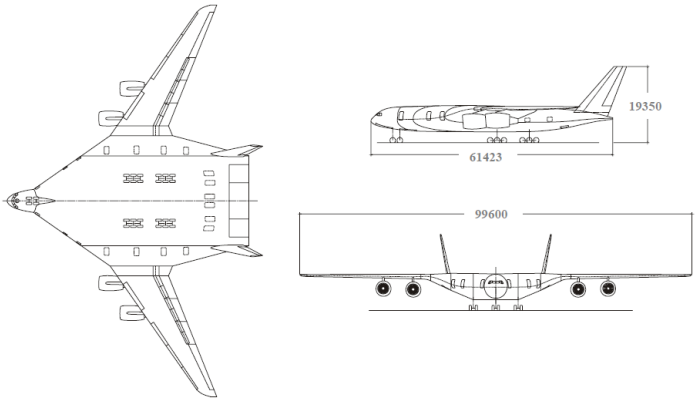

Figure 2-14 VELA3 configuration [7]

While focusing on extensive investigations into the most critical disciplines of a BWB configuration, the goals of the VELA project were to pave the way for further researches on this novel concept at a conceptual level and get closer cognition of the most important issues involved in designing an outstanding BWB transport aircraft. It was realized from this project that the fidelity of BWB assessment and analysis tools had great influences on the design results. The fidelity of tools need to be further improved for a satisfactory design based on the levels of tool fidelity used in the VELA project [7].

2.1.2.4 Silent aircraft at Cambridge-MIT Institute

A BWB transport aircraft program designated “Silent Aircraft eXperiment” (SAX) was conducted by a group from Cambridge University and Massachusetts Institute of Technology (MIT). There are mainly three goals of this research project: construct a multidisciplinary optimization framework with noise as the main design objective, examine the aerodynamic and noise performance of the selected configuration, and finally pinpoint the key challenges of significant noise reduction of aircraft design with the same performance level as the next generation aircraft entering service in 2030s. A BWB configuration was chosen as the baseline of this project based on its advantages on aerodynamic performance and platform mass reduction, and its inherent potential of low noise since a BWB configuration without separate tails has a rather smooth surface. Furthermore, the relatively thick and wide trailing edge of the center fuselage of a BWB configuration provides opportunity to embed the engine inlets. The forward-radiating noise from the engines are in this way shielded by the fuselage

[18]. Another main character that was considered to have dominant influence on the acoustic radiation of an aircraft within the airport perimeter was the speed of the aircraft. With a slower approaching speed the aircraft would have a lower noise production [19].

Three generation of airframes were designed through the SAX project. The optimization of the first generation SAX was focused on minimizing the takeoff weight. The final version of the first generation SAX was SAX-12 which was still confronted with the challenges of reaching the goal of noise reduction. The second generation of SAX design incorporated a quasi-3D airframe design methodology with inverse design capabilities. The objective of the second generation SAX was the reduction of noise by reducing the approaching speed hence the stall speed. The final version of this generation was SAX-29. The last generation of SAX, the SAX-40, was aiming on further refinement of the aerodynamic and weight model. Through the three generations of SAX design the aerodynamic performance of the aircraft was greatly improved and the stall speed was successfully reduced. The accomplishments of this project prove that improving aerodynamic performance and reducing noise radiation could be achieved simultaneously. Key challenges still remain for the airframe design such as the integration of propulsion system and the airframe [19].

Figure 2-15 Three representing SAX designs (SAX-12, SAX-29, and SAX-40) [19]

2.1.3 Pros and cons of BWB configuration

The BWB configuration is a promising choice of next generation transport aircraft based on its inherent advantages over current conventional configurations. Through the extensive researches on different disciplines such as aerodynamic performance, cabin arrangement, stability and controllability, noise reduction etc. the potential of BWB is widely agreed on. However there are still a number of critical challenges for industrial applications of this novel concept. A list of advantages and disadvantages of BWB concept are summarized in this section.

2.1.3.1 Advantages of BWB configuration

- Aerodynamic performance

The emergence of BWB configuration was initially based on the benefits of aerodynamic advantages of its clean and smooth shape compared to the conventional configurations. From the deduction process of Boeing's BWB shape, this configuration has a tremendous reduction of the wetted area compared to a conventional design with the same passenger capacity. The summation of body surface area, exposed wing surface area, engine and nacelle surface area in case of embedded engine installation, and control surface area of a BWB design, is reduced by 33% in total compared to a conventional design with the same requirement of 800 pax. The reduction on wetted area directly reduces the friction drag of the aircraft, which in turn increases the aircraft cruise lift to drag ratio [10].

Besides the benefits from drag reduction, another obvious improvement on aerodynamic performance comes from the all lift section characteristic of a BWB layout. Unlike conventional fuselage which has a cylindrical shape and do not contribute to lift generation, BWB concept is originated from flying wing concepts which means all sections of the configuration are contributing to produce lift. This unique feature of flying wing configuration, including BWB, has a potential of high lift over drag ratio. The Boeing second generation BWB design reached a cruise lift to drag ratio of 23 while 19 of a conventional design with the same design requirements and technologies was achieved [10].

- Cabin capacity

The highly blended shape between center fuselage and outer wings of a BWB provides a wide area of cabin floor. It is therefore possible to arrange more seats in a single deck of a BWB than the conventional tube shaped cabin designs. The passenger capacity of a conventional configuration has almost reached its limit due to the airport limitations. The Airbus A380 has a maximum passenger capacity of 853 and with a span of 79.75m which is very close to the airport 80m limitation of aircraft wing span. Further improving the passenger capacity is difficult for a conventional design without breaking the wing span limitation. The BWB configuration provides opportunity of further improving the passenger capacity with its advantages on aerodynamic efficiency and cabin volume features.

- Cruise speed

The wave drag is related to the second derivative of aircraft section area. For high cruise speed transport, area ruling is required to have a smooth change of section area to reduce the wave drag. A conventional tube and wing transport requires area ruling of the fuselage when its cruise Mach is higher than 0.88. This area ruling will require the section area hence the width of the fuselage to vary by a great extent. The variation of fuselage width then reduces the seats available while increase the structure weight. However, a BWB has an inherent property of smooth variation of its cross section area. The BWB-250 layout designed in Boeing's BWB project has an area ruling very close to the ideal Sears-Haack area distribution. The optimum maximum cruise Mach number of a BWB is still to be investigated even though 0.88 seems no longer a limitation for this configuration [2].

- Noise

Compared to the conventional transport, the clean shape of a BWB with highly blended wing and fuselage, and without conventional empennages produces less acoustic radiation sources. The approaching speed is also an important factor which influences the noise level around the airport perimeter. To reduce the approaching speed the aircraft needs to approach at a higher angle of attack without stall on the basis of current level. The Cambridge-MIT group successfully achieved a BWB design with a lower approaching speed than conventional designs by utilizing multidisciplinary optimization tools in the design process, setting the noise production level of the aircraft as the objective of the optimization. Furthermore, the relatively wide trailing edge of a BWB center fuselage provides opportunity to embed or partially embed the engine inlets when engines are mounted upon the trailing edge of the center fuselage. This arrangement will shadow the forward acoustic radiation of engine inlet noise, and further reduces the noise level of a BWB transport. The result of the SAX research conducted by the Cambridge-MIT group showed that a combination of several noise reduction technologies implemented on a BWB configuration could achieve a drastic noise reduction of 22.5 dB during taking-off and 30 dB during approaching [18].

- Structure

Due to the all lift sections property of a BWB configuration, the wing root section is at the symmetry plane of a BWB aircraft. The wing root section of a BWB has much larger structural height compared to a conventional transport configuration. The large thickness of the root section of BWB comes from the fact of long chord at the central section and the requirement of a relatively large thickness to chord ratio. With a regular thickness to chord ratio the thickness at the wing root section is already much larger than that of a conventional tube wing transport, despite the fact that the thickness to chord ratio at the root section of a BWB is normally large due to the cabin height requirements. The peak bending moment and shear stress at the wing root of a BWB is only about one half of the value of a conventional configuration [10]. The reduction on bending moment and shear stress at the wing root section results in a reduction of the structural weight of a BWB design.

2.1.3.2 Disadvantages of BWB configuration

- Longitudinal stability

Due to the absence of horizontal tails, the longitudinal stability becomes one of the main concerns of a BWB design. A BWB configuration is considered to be trimmed during cruise phase when its aerodynamic center of pressure coincides with its CG with all the trailing edge control surfaces faired. A BWB with a positive static margin as required for conventional transport aircraft implies several design constraints. The wingtips of the swept wings need to be downloaded, acting like the conventional horizontal tails. The downloading of wing tip violates the possibility of elliptical lift distribution along the wing span, resulting an increase of the induced drag. For a positive static margin, the nose down pitching moment needs to be minimized which limits the use of positive aft camber of the BWB section airfoils thus limits the aerodynamic efficiency of transonic airfoils. On the contrast, a BWB with a negative static margin requires active control power with high bandwidth and possibly prohibitive control power requirement [10]. Therefore it may be necessary to have a positive static margin for a BWB design even though it results in a reduction in aerodynamic benefits. At the end of both Boeing and Cambridge-MIT BWB projects, a BWB configuration with positive static margin and without aerodynamic penalties were successfully achieved with careful wing load distribution. The results of these two projects show that it is possible to design a BWB aircraft with positive static margin and with satisfactory aerodynamic performance. However the compromise between satisfactory aerodynamic performance and longitudinal stability needs very careful investigation and modern design methodologies such as MDO tools.

- Controllability

The short moment arms of the trailing edge control surfaces of a BWB configuration raise the requirement of all spanwise control surface distribution and large control surface area. The hinge moments of the control surfaces are related to their sizes by the square/cube law, which means that the size of control surfaces increase by the square of the dimension and the hinge moments increase by the cube. The all spanwise trailing edge control surfaces and their large sizes lead to substantial control power requirements which may easily exceed the capability of current turbofan engines [20]. To maximize the wetted area reduction and structural weight, the BWB configurations from Boeing's project, the European MOB project and Cambridge-MIT project are all without vertical tails. For

directional stability satisfaction of a BWB aircraft either wingtip ruddervons (Boeing X-48) or split-drag ailerons (Northrop Grumman B-2) need to be used. The absence of tails therefore introduce new challenges to the flight control system design.

- Control allocation

The control allocation of a BWB is complicated because of the lack of long coupled pitch effectors, the lack of conventional trimming devices, and the large number of coupled and redundant control surfaces. Without conventional tails some of the trailing edge control surfaces have coupled functions. For example the outboard split elevens can provide pitch, roll and yaw control moments. However, for those control surfaces with multiple functions they may exceed their saturation limits when multiple control commands are given. Under extreme conditions, multiple commands may conflict with each other on the deflections of a particular control surface [20].

- Approaching and landing

Because of the lack of conventional tails the trailing edge control surfaces cannot be used as high lift devices since there are no moments available to balance the moments produced by trailing edge control surfaces. Therefore the maximum section lift coefficient during approaching will be lower than the configuration with trailing edge flaps. This lower maximum lift coefficient then leads to a substantial lower wing loading, and a higher attitude corresponding with higher angle of attack during landing [20].

2.2 Thrust vectoring technology

Thrust vectoring (TV) or thrust vectoring control (TVC) refers to the deflection of thrust line of an engine or rocket during flight in order to provide pitch, yaw, roll moments or direct lift force. For a rocket or ballistic missile which flies outside the atmosphere, thrust vectoring is the primary control force when aerodynamic effect is not available. However for an aircraft thrust vectoring is mainly treated as an augmentation of the primary aerodynamic control forces, or as direct lift force for vertical/short take-off and landing. Almost all the current practical applications of thrust vectoring on aircraft control are within military domain. The effects of thrust vectoring control on civil aircrafts have only been analyzed by a few individuals on particular disciplines. The literature review about thrust vectoring in this report will be limited to the application as a control force providing pitch, yaw or roll moments for aircrafts, excluding the cases of rocket nozzles and the cases of direct lift generators. Therefore hereafter thrust vectoring in this report refers to aircraft control with pure thrust vectoring or combination of thrust vectoring and conventional aerodynamic control surfaces.

2.2.1 History of thrust vectoring researches

2.2.1.1 Researches on thrust vectoring nozzles

The application of thrust vectoring as a control force on an aircraft had a process of evolution and was first applied on military aircrafts. Engine thrust of an aircraft was considered to provide pure propulsive

force before 1970s and was not considered to help control the aircraft. Part of the earliest researches on thrust-vectored control are the American programs among 1973-1980 and were conducted by cooperation among United States Air Force (USAF), NASA, US Navy and industry. These researches were focused on two-dimensional nozzles. It was the simplicity of construction and design which allowed for the 2 dimensional convergent-divergent nozzles to be a natural first choice for nozzle geometry. Implementing a dynamic geometry in axisymmetric nozzles carried with it many inherent design difficulties. The thrust vectoring/reversal researches from the early American thrust vectoring projects reached the following conclusions for the capabilities of advanced nonaxisymmetric nozzle concepts (e.g. two-dimensional nozzles with a vectoring/reversing capability) [21]

- Increasing maneuverability and agility at high lift and/or low dynamic pressure conditions by thrust vectoring/reversal with supercirculation
- Reducing subsonic/transonic cruise drag compared to close coupled axisymmetric nozzles through better nozzle/airframe integration
- Improving longitudinal agility for air combat and increased accuracy and survivability in air-to-ground weapons delivery due to steeper dive angles and higher weapon release altitude by incorporating an in-flight thrust reverser
- Reducing infrared (IR) and radar cross section (RCS) signal due to nozzle configuration influence; IR and RCS observables tend to be highly directional, thereby thrust vectoring has the potential of greatly increases aircraft survivability against seeker missiles
- Improving take-off and landing performance and ground handling of high thrust aircraft

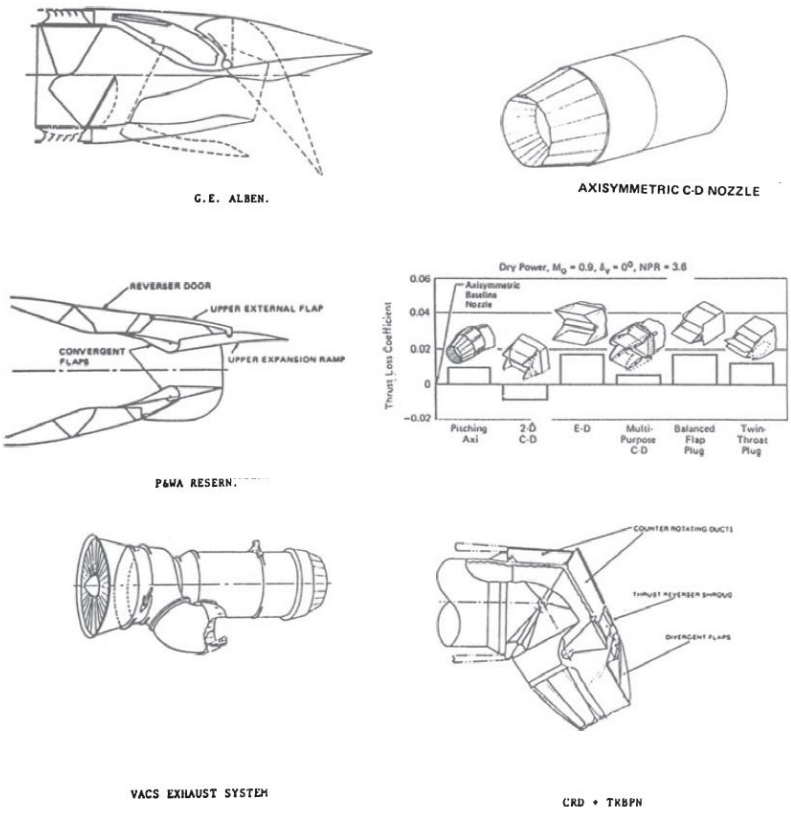

Figure 2-16 Evolution of a few early concepts in thrust-vectoring nozzles [22]

The Exhaust Nozzles for Aerocontrol (ENAC) program conducted by the McDonnell Aircraft Company[2] and sponsored by the Air Force Wright Aeronautical Laboratories, was a project focusing on examining benefits and penalties of using multiplane thrust vectoring nozzles on an advanced supercruise fighter aircraft [23]. Two engine manufacturers, the GE Aircraft Engines and Pratt & Whitney Aircraft, were both participants in this program. The impetus of this program was a postulation that fighter aircraft would face an increasingly formidable threat environment, and operational effectiveness of an advanced supercruise fighter is possible to be increased using advanced nozzles with thrust vectoring/reversing capability.

In contrast to the previous researches which examined 2 dimensional convergent-divergent nozzles as mentioned above, the ENAC project considered advanced nozzles capable of combined thrust vectoring in both pitch and yaw planes. From their results, the resultant thrust coefficient due to thrust vectoring had only a small reduction. At the design nozzle pressure ratio of 7.3 of one examined nozzle, the thrust reduction due to thrust vectoring was only 0.015, and the thrust deflection angle closely matched the nozzle geometrical deflection angle. Another examined nozzle showed similar behaviour on nozzle thrust coefficient and effective deflection angle. Except for the benefits on low speed and high angle of attack maneuvers obtained from thrust vectoring, there were penalties noticed through this project. One penalty was the increment of drag due to enlarged nozzle cross section area and larger faring area over the vectoring nozzles. For the two nozzles reviewed, subsonic drag was increased respectively by 6 and 4 counts, while supersonic drag was increased by 18 and 21 counts. Another penalty was the increment of nozzle weight and the resultant increment of aircraft take-off gross weight. Additional hydraulic power and actuators required to deflect the vectoring nozzles was also one of the penalties from thrust vectoring application [23].

2.2.1.2 Researches on thrust vectoring benefits

Dr. W. B. Herbst, a prominent researcher on modern thrust vectoring flight control from the Messerschmitt-Boelkow-Blohm GmbH (MBB, now part of Airbus Group), indicated in one of his article published in 1980 that there was a need of new fighter aircraft concept which needed to have three contradicting requirements [24]

- Interception of intruders under all weather conditions beyond visual range with middle range missiles
- Air superiority against a superior number of maneuvering offensive targets with short-range weapons
- Short field performance for base survival

Three key technologies were believed to provide solution for the three contradicting requirements

- Digital fly-by-wire control
- Delta wing
- Supermaneuverability

[2] MCAIR, merged with Douglas Aircraft Company in 1967 to form McDonnell Douglas, and later merged with Boeing in 1997 to form The Boeing Company

Here supermaneuverability is a concept of combined post-stall maneuvering and direct force maneuvering capability, and direct force refers to the vectoring thrust. Post stall maneuvering capability is primarily used for positioning a fighter aircraft into an advanced condition. It is believed that a lack of high angle of attack capability and the controllability under this condition will lose the offensive and defensive advantages of a fighter aircraft. A conventional fighter aircraft is not able to perform post stall maneuver because beyond its maximum lift angle of attack the airflow around the wing is separated, the efficiency of control surfaces will decrease while the requirement of control power increases as a result of backward movement of aerodynamic center. The most suitable solution to post stall maneuvering or supermaneuverability is the deflection of engine thrust, i.e. thrust vectoring [24].

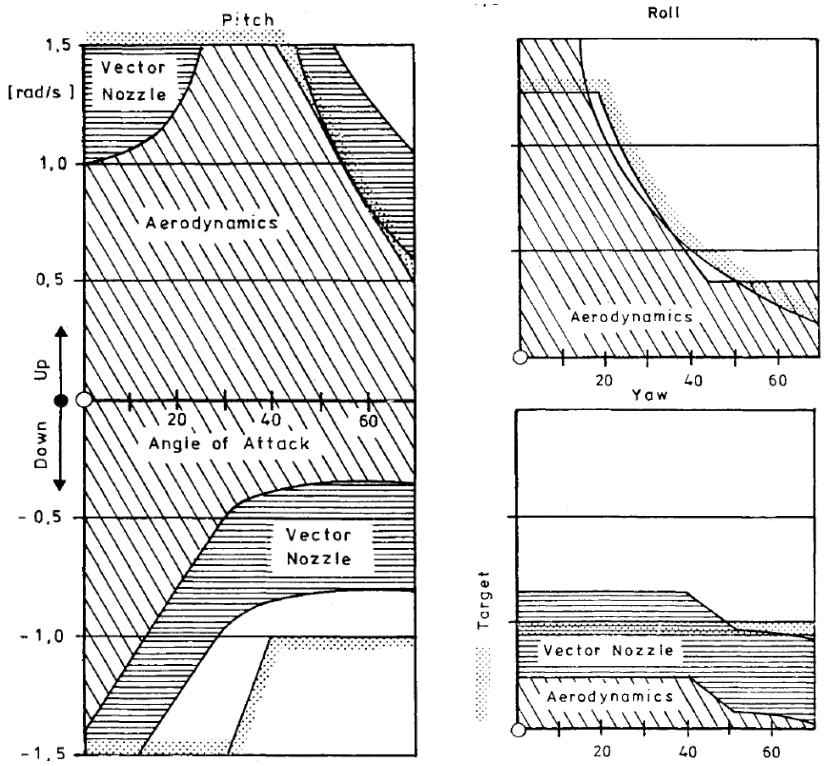

Figure 2-17 Benefits of thrust vectoring in controllability of a fighter aircraft [24]

Philippe Costes, a researcher from the French National Aerospace Research Center (ONERA), investigated thrust-vectored and post-stall maneuvers with a numerical method. The numerical method was designed and validated for dynamic performance assessment of an aircraft in a one-to-one close range air combat. Philippe appears to be the first researcher studying on the advantages of thrust vectoring in a combat situation with a conventional aircraft [6]. In Philippe's investigation, thrust vectoring and post-stall maneuvers are investigated in this way: numerical simulations of air-gunnery combat maneuvers from two initial conditions (high altitude and low altitude) and various aircraft combat scenarios (conventional aircraft, conventional aircraft with thrust vectoring, and conventional aircraft with thrust vectoring and high angle of attack capabilities) were carried out. Results of these simulations were compared and advantages of advanced control methodology were validated.

Variables including aircraft state (horizontal coordinates x and y, altitude z, velocity vector V, flight path angle and azimuth angle, angle of attack, bank angle, thrust ratio, thrust deflection, Mach number) as well as threat of one fighter aircraft engaged in the combat over the other fighter aircraft

were taken into account through the simulation. The threat m of a fighter aircraft over its adversary was defined as a function of the distance D between two airplanes, and the off-boresight angle ε (angle between the fuselage axis and the line of sight – leading to the adversary), which could be expressed with the following equation

$$m = m(D, \varepsilon)$$

A representing contour plot of the threat of a fighter aircraft over its opponent is shown in Figure 2-18

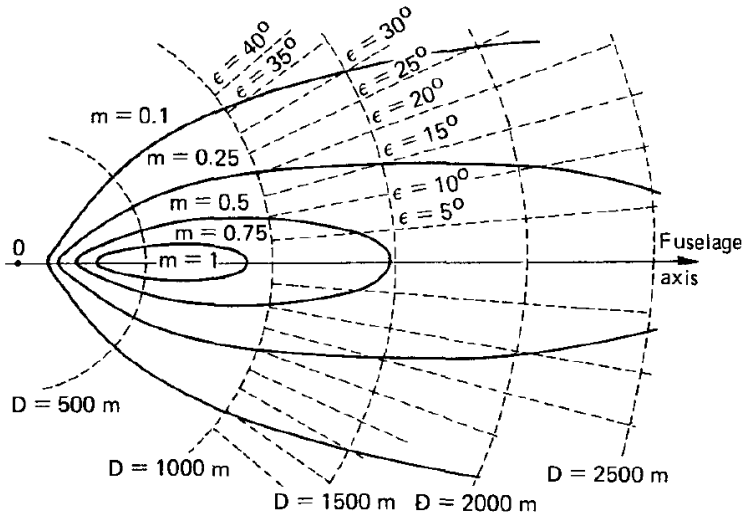

Figure 2-18 Typical iso-threat curves [25]

Results of Philippe's simulations indicated:

- By implementing thrust vectoring in one of the two conventional fighter aircrafts engaged in a close-distance dog-fight, and without post-stall maneuvering capabilities for both of the aircrafts, thrust vectoring was effective in: maximizing normal load factor and providing a positive increment in turning rate for the thrust-vectored aircraft; exerting a high threat for a longer duration at the first shooting opportunity; remaining in a favorable positon behind the adversary.
- Applying post-stall maneuvers (high angle of attack) in one of the two conventional fighter aircrafts without the help of thrust vectoring had little use of this kind of combat engagement since the favorable post-stall maneuver and the relevant aircraft position was not able to be preserved.
- Use of both thrust vectoring and high angles of attack was a very efficient way to improve maneuverability.

The benefits of using thrust vectoring and post-stall maneuvers simultaneously could be depicted with Figure 2-19, which was one of the cases of Philippe's simulations. In this simulation case airplane A used both thrust vectoring and post-stall maneuvering capabilities, while airplane B was a conventional configuration. It can be found from the plots of Figure 2-19 that airplane A had a much rapid changes of angle of attack, bank angle and Mach number. The threat of airplane A over airplane B was always larger than the threat of the airplane B over airplane A [25].

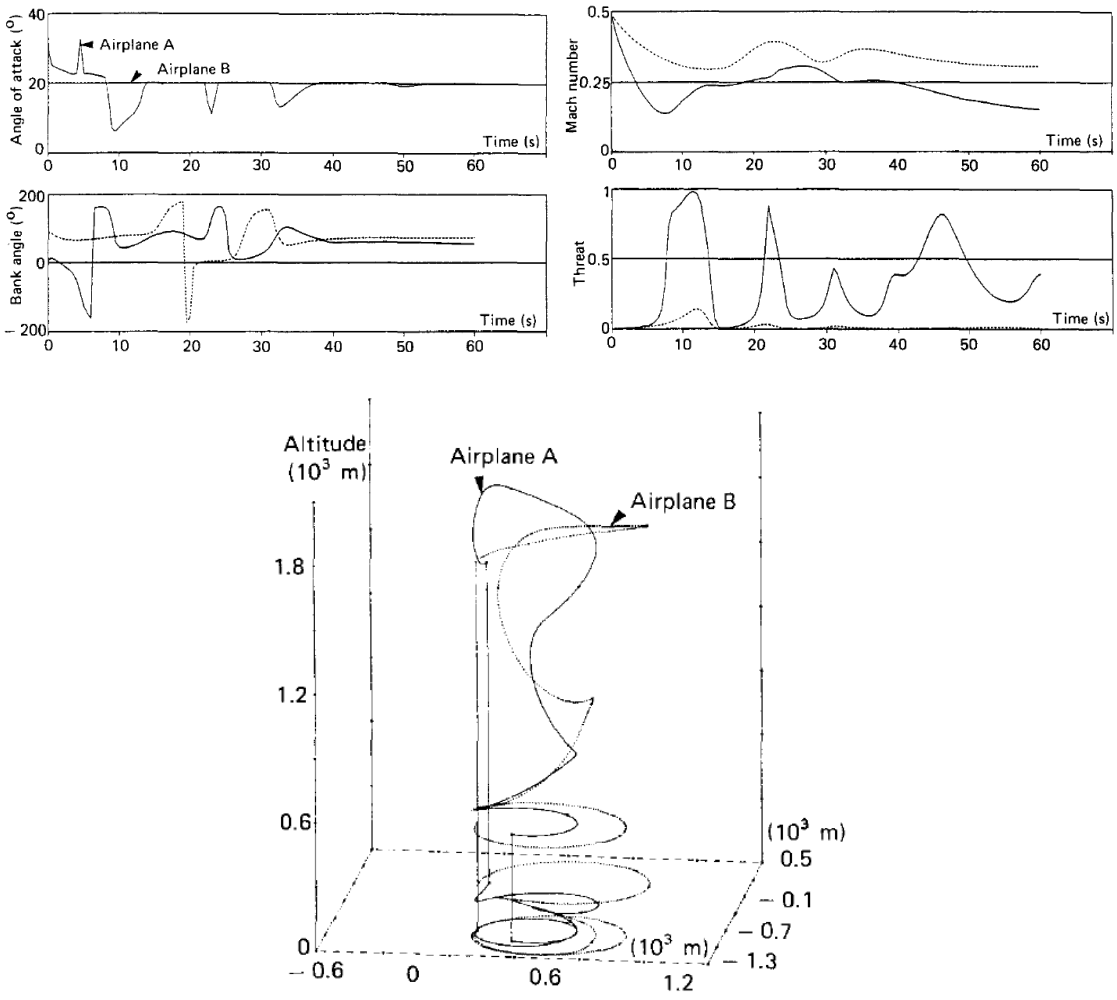

Figure 2-19 Close-distance dog-fight simulation between two fighter aircrafts [25]

2.2.1.3 Military implementations

Not long after the suggestions of applying thrust vectoring on new fighter aircraft for supermaneuverability, this novel idea had started to be tested on several military aircraft configurations. From the implementations and tests of thrust vectoring conducted until now, there are mainly two kinds of applications of thrust vectoring on military aircrafts. The first and earliest application is to provide Short/Vertical Take-off and Landing (S/VTOL) capability. Typical examples are the British/American Harrier AV8B and American F-35B. The second and wider application is to provide in-flight maneuvering control or control augmentation. Some of the well-known research projects and tests, focusing on the effects of thrust vectoring for in-flight maneuver control, are the American/German X-31, the American F-15 ACTIVE (Advanced Control Technology for Integrated Vehicles), F-16 MATV (Multi-Axis Thrust Vectoring), F-18 HARV (High Angle of Attack Research Vehicle), and the Russian Su-37 projects. The successful industrial productions with thrust vectoring technology used for in-flight control augmentation include the American F-22, the Russian Su-30MKI and Su-35 fighters.

a. X-31
Picture: NASA

b. F-18 HARV
Picture: NASA

c. F-15 ACTIVE
Picture: NASA

d. F-16 MATV
Picture: NASA

e. Su-35
Picture: Wikipedia

f. F-22
Picture: NASA

Figure 2-20 Military tests and implementations of thrust vectoring

The American/German X-31 was an experimental program focusing on agile flight with the post-stall regime between 1990 and 1994, in order to produce flight test data of thrust vectoring augmented maneuvering and give fighter designers a better understanding of the effectiveness of flight controls with thrust vectoring. Thrust vectoring flight control capability was realized by three carbon-fiber composite paddles at the nozzle exit (ETV, External Thrust Vectoring). In November of 1992 X-31 accomplished a roll around the velocity axis of the aircraft at 70 degrees of angle of attack. In April of 1993 it successfully executed a minimum radius 180 degree turning using the post-stall “Herbst Cobra Maneuver”. During the 1994 Paris Airshow X-31completed a maneuver with over 90 degrees of angle of attack. The X-31 successfully demonstrated that thrust vectoring technology was able to improve the maneuverability and post-stall maneuvering capability of a fighter aircraft.

The F-18 HARV project used the same type of thrust vectoring mechanism as the X-31 project, but with metal alloy materials. The original divergent engine nozzle was removed to mount the three metal paddles. The project lasted for more than 9 years from April 1987 until September 1996. During phase II the angle of attack envelop was pushed to 70 degrees. Thrust vectoring was the primary control power for F-18 HARV configuration. From this project it was concluded that controlling the aircraft above 40 degrees of angle of attack could only be accomplished with thrust vectoring flight control. Because the divergent portion of the nozzle was removed, the F-18 HARV project was limited to subsonic flight even while afterburning was still functioned.

The American F-15 ACTIVE and F-16 MATV projects both used 3-D axisymmetric thrust vectoring nozzle. The primary objective of the F-15 ACTIVE project was maturing thrust vectoring technology enable the integration of thrust vectoring technology into the flight control system for industrial application. The project was particularly focused on

- Pitch/Yaw operability and compatibility testing

- Aircraft and nozzle performance testing
- Adaptive aircraft performance technology testing
- Jet interaction effects testing
- Measuring aircraft response to steady-state vectoring

In September of 1996 thrust vectoring was first utilized on F-15 ACTIVE at flight Mach number 2.0 after several supersonic pitch and yaw flight tests.

Two of the production fighter aircrafts with thrust vectoring technology applied are the Russian Su-35 Super Flanker and the American F-22 Raptor. Multi-axis axisymmetric thrust vectoring nozzle is used for 117C engine of Su-35 while pitch-only rectangular thrust vectoring nozzle is used for F-119 engine of F-22. Even though yawing control by thrust vectoring was also developed and tested on F-22, it was later abandoned in favour of the extended vertical tails [6].

2.2.1.4 Civil application researches

Since the emergence of thrust vectoring technology its applications on aircrafts have been mainly focused on military domain. Civil applications of thrust vectoring have only been studied by a few individuals within conceptual levels. Eric carried out researches on the economical and safety benefits from thrust vectoring applications on commercial transports. His results indicated that economic benefits could only be achieved when thrust vectoring technology was integrated with aircraft design from the very beginning. All economic benefits depend on the integrated aircraft/engine configuration. For current wing-mounted engine layout thrust vectoring is not favorable. Safety benefits were considered to be more possible to realize due to increased low speed flight control capability and control system redundancy. However the introduction of new technology system required the guarantee of reliability of thrust vectoring system to keep the benefits of its application [3].

Research results of the economic efficiency of thrust vectoring application on civil transport vary significantly. A research group from University of Texas analyzed the flight performance of a commercial aircraft based on B777-300ER with thrust vectoring application. The configuration with thrust vectoring application had engines moved from wings to rear fuselage in order to improve the moment effects of vectored thrust. Original empennages were removed on the basis of pure thrust vectoring control along with the benefits of weight and drag reduction. Hence the resulted configuration had a lighter MTOW and less drag. Their results show that L/D could be increased by 17%, empty weight reduced by 17%, fuel weight reduced by 27% and direct operational cost (DOC) reduced by 18% with the application of thrust vectoring on their chosen aircraft. However control analysis on this modified configuration showed that with original empennages removed the aircraft was not static stable anymore and had stability problems. Suggestions were therefore given that a combination of thrust vectoring control and smaller aerodynamic control surfaces could be a feasible and beneficial solution [4].

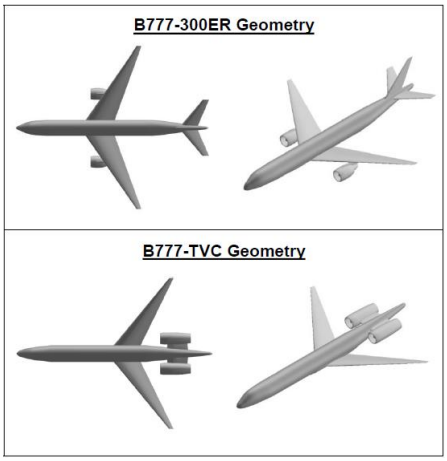

Figure 2-21 Baseline B777-300ER and B777-TVC configurations [4]

A. J. Steer carried out static and dynamic performance researches with integrated control of vectoring thrust and conventional aerodynamic control surfaces on a supersonic commercial transport aircraft. A primary difference between the control power of conventional aerodynamic surfaces and thrust vectoring nozzles is that conventional aerodynamic control surfaces are dependent on dynamic pressure of the coming flow while thrust vectoring nozzles do not. The characteristics of aerodynamic control surfaces introduce some undesired results that during low speed phases the control power of aerodynamic control surfaces are insufficient while the control requirements are relatively high. Thrust vectoring control for a supercruise transport aircraft has its advantage due to the fact that, during low speed flight with high angle of attack the induced drag is high, resulting in high engine thrust and hence thrust vectoring control power. Through Steer's researches, it was found that for the supercruise transport aircraft model used in his project, the pitch control power generated by thrust vectoring was significantly less than that generated by conventional control surfaces. However acceptable pitch rates could be achieved using full engine thrust and total nozzle authority. Using pitching and rolling moments generated by thrust vectoring could release the primary tasks of elevons and enable the implementation of a more efficient low-speed lift-generating flap. An axisymmetric thrust vectoring control could generate additional yawing moments and thus a reduction of fin and rudder size was possible which leads to a reduction of empennage surface area and weight. However in order to achieve the required level of directional stability, a certain magnitude of aerodynamic control power need to be kept [5].

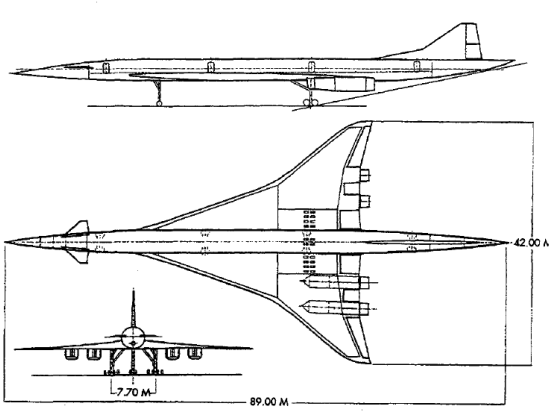

Figure 2-22 Supercruise baseline configuration analysed in Steer's project [5]

Civil application of thrust vectoring has only a short research history since the beginning of 1990s and has only been carried out by a few individuals at conceptual level. One of the main reasons for this lack of researches and applications of thrust vectoring on civil transport configurations is that, since the emerging of thrust vectoring control its main capabilities have been widely recognized as improving the maneuverability and post-stall controllability, which are not the design requirements of civil transports.

2.2.2 Types of thrust vectoring

There are several different ways to classify thrust vectoring. From a mechanism point of view, thrust vectoring nozzles can be sorted into Internal Thrust Vectoring (ITV) and External Thrust Vectoring (ETV). For ITV, the thrust line is deflected by deflecting the engine nozzle directly. This kind of thrust vectoring will need a more complicated engine nozzle with capabilities of controlling the nozzle section area and thrust line direction simultaneously. The ETV thrust vectoring incorporates extra control structures at the end of the original engine nozzle or modified engine nozzle, such as the paddles used in X-31 and F-18 HARV projects. From a controlling authority point of view, thrust vectoring can be sorted into pure thrust vectoring and partial thrust vectoring. For pure thrust vectoring, the conventional aerodynamic control power is fully replaced by engine thrust control, no aircraft trailing edge control surfaces or tails exist on this kind of aircraft configuration. In contrast, for an aircraft with partial thrust vectoring control, conventional aerodynamic control surfaces and engine thrust are working together to control the aircraft. Most of the flight test models, such as those configurations mentioned in 2.2.1.3, incorporated partial thrust vectoring control. The two production fighter aircrafts, the Su-35 and F-22, both uses partial thrust vectoring control as well. However the level of authority of thrust vectoring control in the above mentioned models vary largely among each other.

According to Dr. Erich Wilson's methodology, another way of sorting the thrust vectoring technology is based on the geometrical location of nozzle deflection [6]. Four types of thrust vectoring nozzle can be identified in the following way

- Type I – Nozzles whose baseframe is mechanically rotated before the geometrical throat
- Type II – Nozzles whose baseframe is mechanically rotated at the geometrical throat
- Type III – Nozzles whose baseframe is not rotated. Rather, the addition of mechanical deflection post-exit vanes or paddles enable jet deflection
- Type IV – Jet deflection through counter-flow or co-flowing auxiliary jet streams. Fluid-based jet deflection

2.2.2.1 Type I

The thrust vectoring portion of the nozzle is mechanically deflected before the throat of nozzle. This kind of deflection is able to preserve the axisymmetric shape of the nozzle exit, and therefore dynamic variation of the nozzle section geometry does not come into question and the effective deflection angle is identical with the geometrical deflection angle. Consistency in effective vectoring angle is the primary advantage of Type I nozzle. The drawback of Type I vectoring nozzle is its high cost of additional

weight and hydraulic power. An example of Type I vectoring nozzle is the one used on 117C engine of the Russian Su-35 Super Flanker.

Figure 2-23 Type I vectoring nozzle, picture: NOP Saturn

2.2.2.2 Type II

The vectoring nozzle is rotated mechanically at the geometrical nozzle throat. The advantage of Type II vectoring nozzle over Type I is the less weight penalty and less complicated mechanism for thrust vectoring, and therefore less hydraulic power requirement. The reduced nozzle weight allow faster rotation rates of the nozzle up to 120 °/s. Hinging the vectoring nozzle at the throat of the baseframe gives advantage of thrust vectoring deflection range up to ±30°, while the approximate range for Type I vectoring nozzle is about ±15°. One drawback of Type II vectoring nozzle is the deviation of its effective deflection angle from the geometrical deflection angle. However the loss in deflection efficiency is compensated by the increased rotation range. Examples of Type II vectoring nozzles include the nozzles used on F-15 ACTIVE and F-16 MATV.

Figure 2-24 Type II vectoring nozzle, picture: NASA

2.2.2.3 Type III

The nozzle exit flow is deflected by several additional carbon fiber/metal alloy paddles mounted at the end of the engine nozzle exits. This type of thrust vectoring is the most practical for retrofitting aircraft

with TVC technology. Type III nozzles require the least cost and weight increments and the least modifications of original engine configurations. However a significant disadvantage of this kind of thrust vectoring is the nonuniformly deflection of the nozzle flow, which will lead to a loss in effective thrust deflection angle as well as the thrust coefficient. Examples of Type III thrust vectoring include the X-31 and F-18 HARV projects.

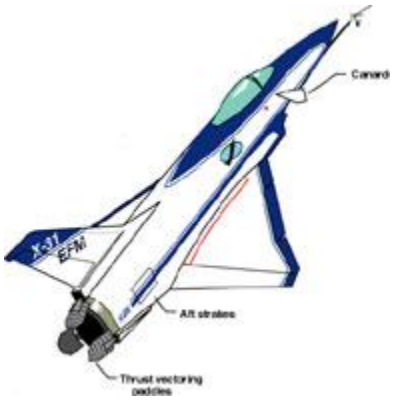

Figure 2-25 Type III vectoring nozzle, picture: NASA

2.2.2.4 Type IV

Instead of mechanically deflecting the nozzle, Type IV vectoring nozzles deflect the core flow by fluidic manipulations. NASA Langley Research Center, in collaboration with the USAF, industry and academic partners, has conducted extensive researches on fluidic thrust vectoring in the 1990s. Fluidic thrust vectoring methods mainly contain three basic categories: shock vector control, throat shifting, and counterflow methods [26].

For the fluidic thrust vectoring with the shock vector control method, a secondary forced, asymmetric flow is injected into the supersonic portion of the primary flow. The interaction between the injection flow and primary supersonic flow will create an oblique shock. This oblique shock diverts the primary flow and therefore large thrust vectoring angles are produced. The high expense of this thrust vectoring method is the loss of thrust efficiency when the primary flow passes the oblique shock, and the loss of thrust performance when the oblique shock impinges the opposing nozzle wall.

The hypothesis of the throat shifting method is that a forced, asymmetric injected secondary flow will change the location of the nozzle throat. In a non-vectored model, the throat (sonic plane) is the geometrical minimum area. In a thrust-vectoring mode, the secondary airflow creates a new skewed aerodynamic minimum area and shifts the throat of the nozzle to a new location from the geometrical minimum area. The resulting asymmetrical pressure loading on the nozzle surfaces causes a thrust vectoring angle of the primary flow. The new aerodynamic throat is ahead of the geometrical throat and in the subsonic region. Subsonic flow turning minimizes thrust losses.

The hypothesis of the counterflow method is that by applying a suction slot between the primary nozzle and an aft collar, the mixing in the shear layers between the primary flow and secondary flow will lead to asymmetric pressure loading on the collar surfaces, and therefore creates thrust vectoring [26].

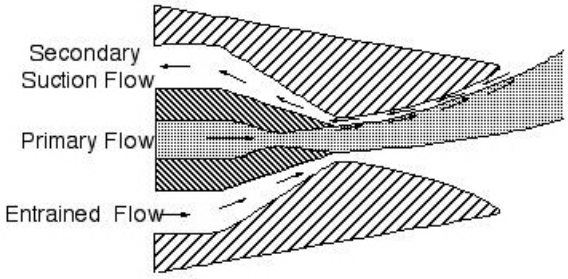

Figure 2-26 Thrust vectoring nozzle with counterflow method [26]

2.2.3 Pros and Cons of thrust vectoring

According to a review of the debates of thrust vectoring technology summarized by Dr. Benjamin Gal-Or from the Israel Institute of Technology, the acceptance of the advantages and effectiveness of thrust vectoring has gone through a long period of refusal and opposition. Opposition came from flight performance engineers, pilots, government departments, as well as industrial investments. It was only after the flight demonstration of the American/German X-31 project that the opposing government department, academia and industry realized the unprecedented potential that thrust vectoring could bring to aircraft control and performance [27]. But thrust vectoring does not come with only advantages. Penalties need to be realized for the application of this novel technology.

Benefits of thrust vectoring technology are:

- Thrust vectoring effectiveness is not aerodynamic dependent, while the efficiency of conventional aerodynamic control surfaces are dependent on the dynamic pressure of coming flow. This characteristic of thrust vectoring provides the opportunity of low speed and high angle of attack application for control augmentation.
- Application of thrust vectoring increases the control power redundancy. While any of the conventional aerodynamic control surface loses its function, thrust vectoring could be used as alternative control power and provides the vital “fly back home” capability.
- Implementation of thrust vectoring technology could reduce the trim drag. Either by providing direct lift force hence reducing the required angle of attack, or by reducing the deflection angles of conventional control surfaces hence reducing the induced drag of the aircraft.
- By applying thrust vectoring control, the control power required on conventional aerodynamic control surfaces are reduced. The reduced control power requirements result in a reduction on the control surface area and therefore the structure weight. The reduction of control surface area also leads to a reduction of friction drag.
- Application of thrust vectoring may result in a possible reduction in the number of conventional aerodynamic control surfaces and associated actuation instruments. Aircraft control could even be achieved purely by thrust vectoring technology with a complete elimination of conventional control surfaces.

Limits and drawbacks of thrust vectoring technology include:

- Implementation of thrust vectoring technology will increase the structural complexity of engine nozzles. The nozzle weight and cost will increase.
- If thrust vectoring is the primary control power of an aircraft, and conventional aerodynamic control surfaces are eliminated or degraded, engine out condition will lead to a reduction of control power and even safety issues. If the aerodynamic control surfaces are designed and sized to be adequate in case of thrust vectoring failures, then the implementation of thrust vectoring will result in an increment of aircraft weight, and a waste of control capability under normal conditions.
- Thrust vectoring control is dependent on the current thrust setting of the engines. Conflictions may occur with low engine thrust while high control power is required.
- Controlling the aircraft with thrust vectoring requires complex integrated flight and propulsion control. Control allocation and control law design becomes more complicated when thrust vectoring control is integrated into the conventional aerodynamic control system.
- Thrust deflection leads to a loss of nozzle thrust. The magnitude of thrust loss depends on the type and design of the vectoring nozzle.

3 Supporting tools and aircraft configuration

The flight mechanics analyses on the thrust vectoring control are carried out with the VELA2 BWB configuration in this project. The effects and effectiveness of thrust vectoring control for trimming the VELA2 aircraft under steady level flight conditions in the longitudinal plane are analyzed with a flight mechanics toolbox called Phalanx. To simulate thrust vectoring controls with Phalanx, all the inputs required by Phalanx for flight mechanics calculations need to be prepared with different tools. This chapter introduces the tools used in this project and the modified VELA2 configuration as the test model of thrust vectoring control.

3.1 Tools utilized

With a geometrical model of the VELA2 configuration provided by DLR, different analysis tools are required to prepare the data needed for flight mechanics simulations of thrust vectoring control. The relative disciplines of tools include aerodynamic performance estimation (including control derivatives), aircraft mass and inertia estimation, and flight mechanics simulation. An engine performance map of another European BWB project, the MOB project, is used directly in this project. Therefore engine performance estimation tool is not required in this project. With four engines used for the MOB project, the total thrust is calculated to be adequate for the VELA2 configuration.

3.1.1 Flight mechanics simulation

The flight mechanics toolbox Phalanx developed by Mark Voskuijl is used for thrust vectoring control simulation, with thrust vectoring modules developed in this thesis project. Phalanx is written in Matlab and makes extensive use of Simulink platform. It is capable of carrying out flight mechanics analysis with different levels of model fidelity. The equations of motion of Phalanx is based on multi-body dynamics which makes the variation of CG and mass within the toolbox feasible. Its capabilities include:

- Aircraft performance analysis (e.g. mission analysis)
- Trim assessment
- Linearization and control law design
- Virtual flight test (time domain simulation, also real-time with a pilot in the loop)
- Handling qualities assessment
- Loads prediction (in-flight maneuvers, landings, …)
- Aircraft response to atmospheric turbulence
- Flexible aircraft dynamics (including aeroelastic effects)

Phalanx constructs a Simulink model for flight mechanics analysis. To construct the Simulink model the aerodynamic performance database and engine performance map need to be prepared in the format of look-up tables as required by Phalanx. For simulations with conceptual fidelity, the information of landing gears may be neglected. Information about control allocation matrix, position and rate limits

of control effectors, aircraft mass and inertia information, as well as locations of engines need to be saved in Matlab scripts as Simulink model inputs.

The Simulink model of Phalanx mainly contains 5 sub-models: aircraft components, flight control system, equations of motion, atmosphere and data storage modules.

3.1.1.1 Aircraft components module

Under a given flight condition, the aircraft component module calculates all the moments and forces produced by all the aircraft components in the body coordinate system, including the aerodynamic forces and moments produced by aircraft main body and ACS as well as the thrust forces and moments produced by vectoring nozzles.

The method that Phalanx uses in this project to calculate the aerodynamic forces and moments of the aircraft main body (AMB, aircraft components excluding ACS) based on the aerodynamic performance database is expressed with the following equations:

$$\begin{cases} C_X = C_X(\alpha,\beta,V) + C_{X_p}(\alpha,\beta,V)\cdot p + C_{X_q}(\alpha,\beta,V)\cdot q + C_{X_r}(\alpha,\beta,V)\cdot r \\ C_Y = C_Y(\alpha,\beta,V) + C_{Y_p}(\alpha,\beta,V)\cdot p + C_{Y_q}(\alpha,\beta,V)\cdot q + C_{Y_r}(\alpha,\beta,V)\cdot r \\ C_Z = C_Z(\alpha,\beta,V) + C_{Z_p}(\alpha,\beta,V)\cdot p + C_{Z_q}(\alpha,\beta,V)\cdot q + C_{Z_r}(\alpha,\beta,V)\cdot r \\ C_l = C_l(\alpha,\beta,V) + C_{l_p}(\alpha,\beta,V)\cdot p + C_{l_q}(\alpha,\beta,V)\cdot q + C_{l_r}(\alpha,\beta,V)\cdot r \\ C_m = C_m(\alpha,\beta,V) + C_{m_p}(\alpha,\beta,V)\cdot p + C_{m_q}(\alpha,\beta,V)\cdot q + C_{m_r}(\alpha,\beta,V)\cdot r \\ C_n = C_n(\alpha,\beta,V) + C_{n_p}(\alpha,\beta,V)\cdot p + C_{n_q}(\alpha,\beta,V)\cdot q + C_{n_r}(\alpha,\beta,V)\cdot r \end{cases} \tag{3.1}$$

$$\begin{cases} X = C_X \cdot qS \\ Y = C_Y \cdot qS \\ Z = C_Z \cdot qS \\ l = C_l \cdot qSc \\ m = C_m \cdot qSc \\ n = C_n \cdot qSc \end{cases} \tag{3.2}$$

in which

$C_X, C_Y, C_Z, C_l, C_m, C_n$: Force and moment coefficients in respective X, Y and Z direction

$(C_X, C_Y, C_Z, C_l, C_m, C_n)_{p,q,r}$: Stability derivatives w.r.t angular rates

X, Y, Z, l, m, n : Aerodynamic forces and moments in respective X Y and Z direction

p, q, r : Rolling, pitching and yawing rate of the aircraft

α : Angle of attack of the aircraft

β : Sideslip angle of the aircraft

V : Airspeed

q : Dynamic pressure

c : Aircraft reference length, normally the MAC of the aircraft

For the problems analyzed in this project, namely the steady level trim flights, the rotation rates are all zero. Equation (3.1) and (3.2) can be simplified for this project as:

$$\begin{cases} X = C_X(\alpha,\beta,V)\cdot qS \\ Y = C_Y(\alpha,\beta,V)\cdot qS \\ Z = C_Z(\alpha,\beta,V)\cdot qS \\ l = C_l(\alpha,\beta,V)\cdot qSc \\ m = C_m(\alpha,\beta,V)\cdot qSc \\ n = C_n(\alpha,\beta,V)\cdot qSc \end{cases} \tag{3.3}$$

Compared to the aerodynamic forces and moments of the aircraft main body, the aerodynamic performance of ACS is also dependent on its deflection angles. Both Tornado and Phalanx are based on linear assumptions of ACS aerodynamic performance, which means that the control derivatives of an ACS at a particular flight condition (α , β and V) are treated as constant values and do not change w.r.t deflection angles. The method Phalanx uses for calculating the aerodynamic forces and moments coefficients of all ACS is:

$$\begin{cases} C_X = \sum_1^n \left[C^i_{X,\delta}(\alpha,\beta,V)\cdot\delta_i \right] \\ C_Y = \sum_1^n \left[C^i_{Y,\delta}(\alpha,\beta,V)\cdot\delta_i \right] \\ C_Z = \sum_1^n \left[C^i_{Z,\delta}(\alpha,\beta,V)\cdot\delta_i \right] \\ C_l = \sum_1^n \left[C^i_{l,\delta}(\alpha,\beta,V)\cdot\delta_i \right] \\ C_m = \sum_1^n \left[C^i_{m,\delta}(\alpha,\beta,V)\cdot\delta_i \right] \\ C_n = \sum_1^n \left[C^i_{n,\delta}(\alpha,\beta,V)\cdot\delta_i \right] \end{cases} \tag{3.4}$$

in which

$C^i_{X,\delta}, C^i_{Y,\delta}, C^i_{Z,\delta}$: Aerodynamic force derivatives of the ith ACS in X, Y and Z direction

$C^i_{l,\delta}, C^i_{m,\delta}, C^i_{n,\delta}$: Aerodynamic moment derivatives of the ith ACS in X, Y and Z direction

δ_i : Deflection angle of the ith ACS

The forces and moments produced by all of the ACS are summations of the forces and moments produced by each ACS as depicted in equation (3.4). The aerodynamic forces and moments of the whole aircraft are then summations of those produced by both AMB and ACS.

The process of calculating the thrust forces and moments with the thrust vectoring Simulink module developed in this thesis project is shown in Figure 3-1. With a given engine control input (including the throttle position and nozzle deflection control input in this project) and a given engine working condition (including the aircraft flight altitude and speed), the engine gross thrust is determined which counts the thrust loss due to nozzle deflections. Considering nozzle deflections the components of net thrust in three directions of the body reference frame can be calculated with the engine drag subtracted from the gross thrust. With the locations of vectoring nozzles, the components of thrust moments for rolling, pitching and yawing control can be calculated.

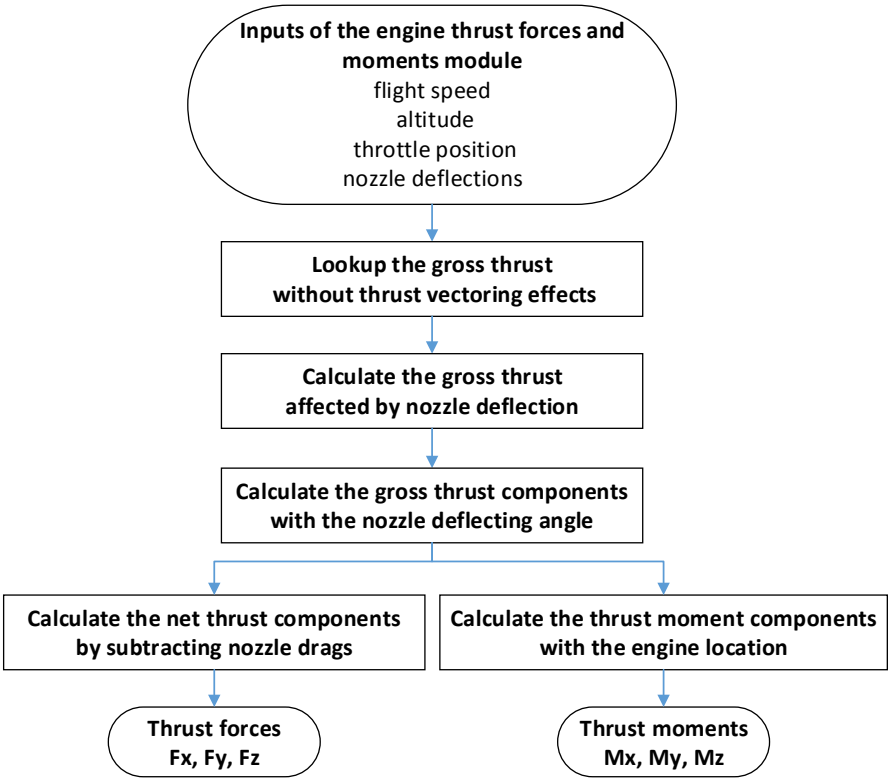

Figure 3-1 Process and hierarchy of calculating thrust forces and moments

The summation of the aerodynamic forces/moments and the propulsive forces/moments constitutes the total forces/moments acting on the analyzed aircraft.

3.1.1.2 Flight control system module

The flight control system module calculates the deflection of every ACS for a given pilot control input, as well as the power lever angle (PLA) of the engines for a given throttle control input. For the updated Phalanx which includes the control of vectoring nozzles, the flight control system module also calculates the deflection of every vectoring nozzle similar to the control of ACS. When calculating the deflections of ACS and vectoring nozzles, the control modules take into account the respective gearing ratio between pilot control inputs and control effector deflections, the control allocation matrix and

the position and rate limits of the control effectors. Represent the control inputs after gearing with a vector $\mathbf{d}$, the control allocation with a matrix $\mathbf{H}$ and the deflection of all control effectors (either every ACS or every vectoring nozzle) with a vector $\boldsymbol{\delta}$, then the calculation of control deflections from control inputs can be expressed with a general control allocation equation:

$$\boldsymbol{\delta} = \mathbf{H}\mathbf{d} \tag{3.5}$$

For an aircraft the control inputs are normally a three by one vector representing the lateral, longitudinal and directional controls. If there are m ACS used for controlling an aircraft equation (3.5) can be written more precisely as:

$$\boldsymbol{\delta}^{m\times 1} = \mathbf{H}^{m\times 3}\mathbf{d}^{3\times 1} \tag{3.6}$$

The process of determining the ACS deflections is shown in Figure 3-2. The range of each of the three control inputs is from -1 to 1 representing the two extreme positons of the pilot stick or pedal. By multiplying the gearing ratio the pilot control input for a particular control moment (rolling, pitching or yawing) is transformed into the desired ACS deflection magnitude. The control inputs after gearing are transferred into deflections of all the utilized ACS by multiplying the control allocation matrix. Saturation check for every used ACS is carried out before the ACS is finally deflected, in order to restrict all the ACS deflections within a feasible range.

Figure 3-2 Control process of ACS deflections

The process of determining the nozzle deflections from the control inputs is similar to the process of calculating the deflections of ACS as summarized in Figure 3-3. During the implementation of thrust vectoring control in Phalanx, thrust vectoring capability is designed to be able to be switched on or off by a control variable of thrust vectoring application. When thrust vectoring is switched off, the control inputs for nozzle deflections are set to constant zero, and the nozzles are forced to work in conventional conditions. A main difference between the control allocation matrix of ACS and axisymmetric vectoring nozzles is there are two rows in a control allocation matrix for controlling one vectoring nozzle, instead of one row for the controlling of every ACS. This is because that an axisymmetric nozzle is capable of deflecting in both lateral and vertical directions. There need to be one row in the control allocation matrix for the control of nozzle deflection in each of the two directions.

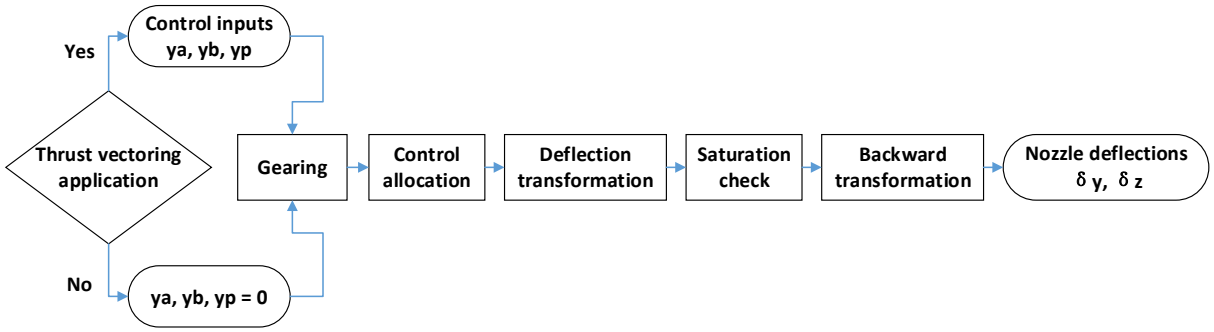

Figure 3-3 Control process of nozzle deflections

Based on the capability of deflecting in two directions simultaneously for an axisymmetric vectoring nozzle, saturation check of a deflected nozzle is also different from the saturation check of an ACS. Under given control inputs of vectoring nozzles, the commanded deflections of every nozzle are calculated through the predefined control allocation matrix. Then the commanded deflections are transformed into absolute deflection angles and deflection azimuths for saturation checking. If the commanded deflection angles exceed the capability limits of nozzle deflections the commanded values are overwritten by the limits, otherwise the commanded deflections are kept for the final values. After checking for the saturations, the confirmed nozzle deflections are transformed back to the form corresponding to the coordinates of the body reference frame, and the nozzles are finally deflected accordingly. The control allocation and saturation check of vectoring nozzles are explained in detail in section 4.2.

3.1.1.3 Equations of motion module

The equations of motion module solves the equation of motion of the aircraft. The moments and forces calculated in the aircraft components module as well as the aircraft mass and inertia information are the inputs of this module. The equation of motion module contains a sub-module of moving mass with inertia. For a commercial aircraft the moving mass and inertia is mainly the fuel and payload. This sub-module allows the variation of CG and aircraft mass within the Phalanx model and enables the capability of analysing the effects of various CG locations.

The equations of motion are set up for rigid-body with Newton's second law [28] and can be expressed as

$$\mathbf{F}_S + \mathbf{W} = \frac{\mathrm{d}}{\mathrm{d}t}\left(m\mathbf{V}\right) + \boldsymbol{\omega} \times \left(m\mathbf{V}\right) \tag{3.7}$$

$$\mathbf{M}_S = \frac{\mathrm{d}}{\mathrm{d}t}\left(\left[\mathbf{I}\right]\boldsymbol{\omega}\right) + \boldsymbol{\omega} \times \left(\left[\mathbf{I}\right]\boldsymbol{\omega}\right) \tag{3.8}$$

where

$\mathbf{F}_S$: net surface force vector in the body reference frame

$\mathbf{W}$: weight vector

m : mass of the aircraft

$\boldsymbol{\omega}$: aircraft angular rate vector

$\mathbf{M}_S$: net moment vector about the CG of the aircraft

$\left[\mathbf{I}\right]$: inertia tensor and is defined by

$$\left[\mathbf{I}\right] = \begin{bmatrix} I_{xx_b} & -I_{xy_b} & -I_{xz_b} \\ -I_{yx_b} & I_{yy_b} & -I_{yz_b} \\ -I_{zx_b} & -I_{zy_b} & I_{zz_b} \end{bmatrix} \tag{3.9}$$

The inertia tensor is defined in the body reference frame. An aircraft is normally symmetrical in y_b in the body reference frame, therefore

$$I_{xy_b} = I_{yx_b} = I_{yz_b} = I_{zy_b} = 0 \tag{3.10}$$

Written in a more detailed form the equations of motion expressed in equation (3.7) and (3.8) can be expanded to the following equation [28]:

$$\begin{bmatrix} W/g & 0 & 0 & 0 & 0 & 0 \\ 0 & W/g & 0 & 0 & 0 & 0 \\ 0 & 0 & W/g & 0 & 0 & 0 \\ 0 & 0 & 0 & I_{xx_b} & 0 & -I_{xz_b} \\ 0 & 0 & 0 & 0 & I_{yy_b} & 0 \\ 0 & 0 & 0 & -I_{zx_b} & 0 & I_{zz_b} \end{bmatrix} \begin{Bmatrix} \dot{u} \\ \dot{v} \\ \dot{w} \\ \dot{p} \\ \dot{q} \\ \dot{r} \end{Bmatrix} = \begin{Bmatrix} F_{x_b} + W_{x_b} + (rv - qw)W/g \\ F_{y_b} + W_{y_b} + (pw - ru)W/g \\ F_{z_b} + W_{z_b} + (qu - pv)W/g \\ M_{x_b} + (I_{yy_b} - I_{zz_b})qr + I_{xz_b}pq \\ M_{y_b} + (I_{zz_b} - I_{xx_b})pr + I_{xz_b}(r^2 - p^2) \\ M_{z_b} + (I_{xx_b} - I_{yy_b})pq - I_{xz_b}qr \end{Bmatrix} \tag{3.11}$$

with the following notation as used in the equations of motion:

u	$\equiv x_b$-component of aircraft translational velocity relative to surrounding air
v	$\equiv y_b$-component of aircraft translational velocity relative to surrounding air
w	$\equiv z_b$-component of aircraft translational velocity relative to surrounding air
p	$\equiv x_b$-component of aircraft rotational velocity (rolling rate)
q	$\equiv y_b$-component of aircraft rotational velocity (pitching rate)
r	$\equiv z_b$-component of aircraft rotational velocity (yawing rate)
F_{x_b}	$\equiv x_b$-component of total pseudo aerodynamic force vector, including thrust
F_{y_b}	$\equiv y_b$-component of total pseudo aerodynamic force vector, including thrust
F_{z_b}	$\equiv z_b$-component of total pseudo aerodynamic force vector, including thrust
M_{x_b}	$\equiv x_b$-component of total pseudo aerodynamic moment vector, including thrust
M_{y_b}	$\equiv y_b$-component of total pseudo aerodynamic moment vector, including thrust
M_{z_b}	$\equiv z_b$-component of total pseudo aerodynamic moment vector, including thrust

For two dimensional longitudinal problems as analyzed in this thesis project,

$$\left(v, \dot{v}, p, \dot{p}, r, \dot{r}, F_{y_b} + W_{y_b}, M_{x_b}, M_{z_b}\right) = 0 \tag{3.12}$$

Then equation (3.11) can be simplified as

$$\begin{bmatrix} W/g & 0 & 0 \\ 0 & W/g & 0 \\ 0 & 0 & I_{yy_b} \end{bmatrix} \begin{Bmatrix} \dot{u} \\ \dot{w} \\ \dot{q} \end{Bmatrix} = \begin{Bmatrix} F_{x_b} + W_{x_b} - qwW/g \\ F_{z_b} + W_{z_b} + quW/g \\ M_{y_b} \end{Bmatrix} \tag{3.13}$$

3.1.1.4 Trim an aircraft with Phalanx

Trim an aircraft with Phalanx is accomplished with Jacobian method [29]. The Jacobian method consists of an iterating process for approaching the final trimmed condition by solving the equations of motion through every iteration step. The objective of the Jacobian method is to calculate the required control vector which ensures that the acceleration vector of the aircraft is close to zero under a specified flight condition.

The flight condition consists of flight altitude h, airspeed V, flight path angle γ, turn rate $\dot{\psi}$, heading angle ψ and angle of sideslip β. In this thesis project when thrust vectoring deflection is set as premise of the trim condition, the pilot control input for nozzle deflections $\left(y_a, y_b, y_p\right)$ is also part of the flight condition vector. The control vector consists of pilot control inputs of ACS deflections $\left(x_a, x_b, x_p\right)$, engine throttle position x_c which is controlled by pilot as well, aircraft pitch attitude θ, roll angle ϕ and flight track angle χ. The aircraft acceleration vector consists of derivatives of three rotational rates $\left(\dot{p}, \dot{q}, \dot{r}\right)$, derivatives of three translational velocities $\left(\dot{u}, \dot{v}, \dot{w}\right)$ and the difference between the achieved sideslip angel and the desired sideslip angle $\beta - \beta_{desired}$.

The flight condition vector, control vector and acceleration vector are denoted respectively by $\mathbf{x}$, $\mathbf{c}$ and $\mathbf{a}$. They can be expressed as:

$$\mathbf{x} = \left(h, V, \gamma, \dot{\psi}, \psi, \beta, y_a, y_b, y_p\right) \tag{3.14}$$

$$\mathbf{c} = \left(x_a, x_b, x_c, x_p, \phi, \theta, \chi\right) \tag{3.15}$$

$$\mathbf{a} = \left(\dot{p}, \dot{q}, \dot{r}, \dot{u}, \dot{v}, \dot{w}, \beta - \beta_{desired}\right) \tag{3.16}$$

When the aerodynamic database, engine performance map, mass and inertia of an aircraft are given, the trimming of the aircraft with Jacobian method becomes a problem that: for a specified flight condition vector, to search for a proper control vector which drives the values of the acceleration vector smaller than a given residual (close to zero) by solving the equations of motion through a process of iterations. For the cases analyzed in this project which are steady level flights in a two dimensional longitudinal plane, the flight condition vector, control vector and acceleration vector become:

$$\mathbf{x} = \left(h, V, \gamma, y_b\right) \tag{3.17}$$

$$\mathbf{c} = \left(x_b, x_c, \theta\right) \tag{3.18}$$

$$\mathbf{a} = \left(\dot{q}, \dot{u}, \dot{w}\right) \tag{3.19}$$

Calculating the acceleration vector with a given flight condition vector and a control vector can be expressed in a general form which represents the process of solving the equations of motion:

$$\mathbf{a} = \mathbf{f}\left(\mathbf{x}, \mathbf{c}\right) \tag{3.20}$$

The procedure of calculating the trim condition of an aircraft with Jacobian method by solving the equations of motion within iterations can be schematically explained with the following flowchart:

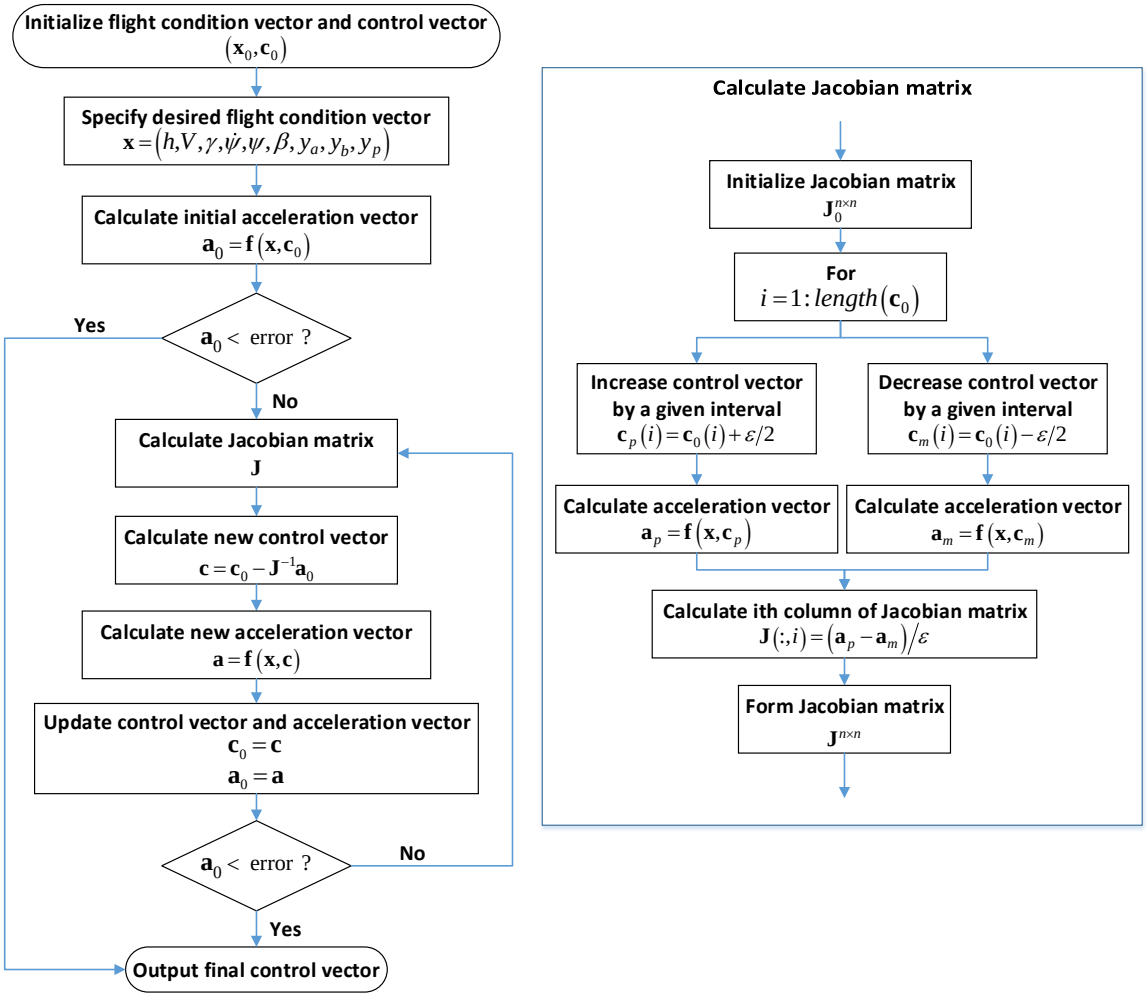

Figure 3-4 Procedure of calculating trim condition with Jacobian method

When the trim condition of an aircraft is calculated with Phalanx the required deflections of ACS and vectoring nozzles, the aircraft attitude, and the throttle position of engines etc. will be known. Then the conditions of aircraft main body, ACS, engines, vectoring nozzles are obtained. The effectiveness of thrust vectoring control can be analysed based on the results simulated with Phalanx.

3.1.1.5 Other Phalanx modules

The atmosphere module calculates all the required parameters concerning the atmosphere, including air temperature, static pressure, air density, and the speed of sound based on given flight altitude. The data storage module saves all the calculate outputs to the workspace of Matlab, including attitude of the aircraft, translational speeds, angular speeds, accelerations, engine working conditions etc.

The capabilities of Phalanx is suitable to be extended with thrust vectoring modules and then carry out simulations on thrust vectoring controls. The outputs of Phalanx simulations are adequate to analyse the effects of thrust vectoring control. The extension of Phalanx with thrust vectoring modules mainly

consists of the thrust vectoring control module and the vectoring nozzle performance module. The modelling of thrust vectoring and its implementation in Phalanx will be discussed in detail in section 4.

3.1.2 Aerodynamic performance

The flight mechanics analysis of Phalanx requires a ready-to-use aerodynamic performance database in the format of look-up tables. For low fidelity analyses proposed in this thesis project, an aerodynamic tool with low fidelity named Tornado is used. This aerodynamic tool is developed by Tomas Melin through his master's thesis project. It is based on the Vortex Lattice Method (VLM) and written in Matlab codes [30]. VLM theorem is based on incompressible and inviscid flow assumptions, therefore the friction drag and wave drag are calculated outside Tornado for a more reliable aerodynamic performance database.

3.1.2.1 VLM and Tornado

Tornado is used in the Department of Integrated Aircraft Design of DLR occasionally for their conceptual aerodynamic performance estimations, and is chosen for the aircraft aerodynamic performance estimations of this project. It is a Matlab implementation of the aerodynamic Vortex Lattice Computational Method. The basis of the VLM is the Prandtl's classical lifting-line theory with upgrades to accommodate the low-aspect-ratio wings. Prandtl's lifting-line theory gives reasonable results for straight wings with moderate to high aspect ratio for incompressible and inviscid flow analysis. It is the first practical theory for predicting the aerodynamic properties of a finite wing developed by Ludwig Prandtl and his colleagues during the period 1911-1918 [31].

The Prandtl's lifting line theory indicates that, a vortex filament of strength Γ which has a fixed position in a flowfield, named a bound vortex, experiences a force from the Kutta-Joukowski theorem. Therefore a finite wing is replaced by a large number of bound vortices with distributed strength, and respective infinite trailing vortices since a vortex filament cannot end in the flow due to Helmholtz's theorem. A bound vortex and the two respective infinite trailing vortex is called a horseshoe vortex base on its shape character. All the bound vortices lie in a same line called the lifting line. A representative finite distribution of bound vortices and trailing vortices is shown in Figure 3-5. $d\Gamma_1$, $d\Gamma_2$ and $d\Gamma_3$ in the following figure represent the respective distributed horseshoe vortices.

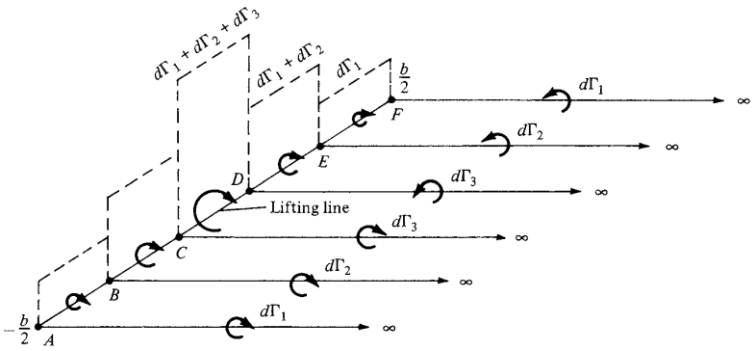

Figure 3-5 Superposition of finite number of horseshoe vortices along the lifting line [31]

If the number of horseshoe vortices are set to infinite while each with a vanishingly small strength, the relevant trailing vortices form a continuous vortex sheet are shown in Figure 3-6. Now the circulation $\Gamma(y)$ along the lifting line becomes a continuous distribution. For an infinitesimally small segment of the lifting line dy located at the coordinate y, the strength of the trailing vortex is $d\Gamma$, and the induced downwash velocity on the lifting line at an arbitrary location y_0 by this segment is calculated by the Biot-Savart law

$$d\omega = -\frac{d\Gamma}{4\pi(y_0 - y)} \tag{3.21}$$

Integrate equation (3.21) over the whole lifting line the total velocity ω_0 induced at y_0 by the entire trailing vortex sheet is obtained

$$\omega(y_0) = -\frac{1}{4\pi}\int_{-b/2}^{b/2}\frac{d\Gamma}{y_0 - y} \tag{3.22}$$

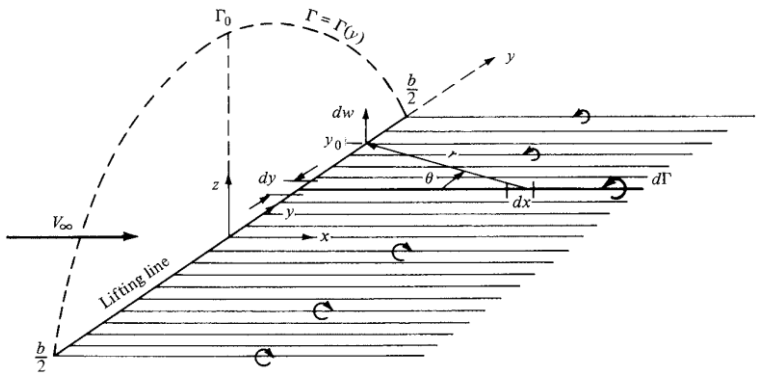

Figure 3-6 Superposition of infinite number of horseshoe vortices along the lifting line [31]

Prandtl's lifting line theory gives reasonable results for straight wings at moderate to high aspect ratio. However for low-aspect-ratio straight wings, swept wings and delta wings, the classical lifting line theory is inappropriate. To apply the classical lifting line theory on these wings, the Prandtl's lifting line model can be extended by a series of lifting lines on the plane of wing from leading edge to trailing edge. This extension forms a lifting surface method as shown in Figure 3-7. The vortex strength along the spanwise direction is denoted by $\gamma = \gamma(x, y)$ and the vortex strength along the chordwise vortex strength is denoted by $\delta = \delta(x, y)$. Following the chordwise vortex behind the trailing edge, the wake vortex has the strength of $\delta_w(y)$ and is equal to the vortex strength at the wing trailing edge. The spanwise vortices and chordwise vortices divide the wing space into panels.

Based on the Biot-Savart law and take the integration over the wing planform, the induced normal velocity at an arbitrary point $P(x, y)$ on the wing planform by both the vortex field of the lifting surface and the wake can be calculated

$$\omega(x,y) = -\frac{1}{4\pi}\iint_S \frac{(x-\xi)\gamma(\xi,\eta)+(y-\eta)\delta(\xi,\eta)}{\left[(x-\xi)^2+(y-\eta)^2\right]^{3/2}} d\xi d\eta$$
$$-\frac{1}{4\pi}\iint_W \frac{(y-\eta)\delta_w(\xi,\eta)}{\left[(x-\xi)^2+(y-\eta)^2\right]^{3/2}} d\xi d\eta \tag{3.23}$$

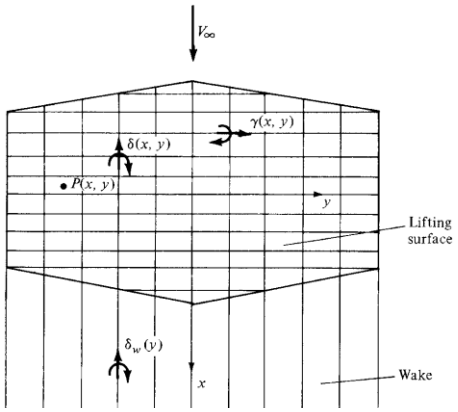

Figure 3-7 Schematic of lifting surface theory [31]

For a computational implementation, finite number of horseshoe vortices hence finite number of panels are considered. The central problem of lifting surface theory is to solve equation (3.23). At any control point P on an arbitrary panel, the normal velocity induced by all the horseshoe vortices can be obtained from the Biot-Savart law. When the flow tangency condition, which means that no normal velocity should be observed for the summation of induced velocity and free flow velocity on each panel, is applied at all the control points, a system of simultaneous algebraic equations is formulated which can be solved for the unknown circulations Γ_n of the distributed horseshoe vortices. With all the circulations solved, the lift distribution is obtained from the Kutta-Joukowski theorem

$$L' = \rho_\infty V_\infty \Gamma \tag{3.24}$$

Based on the implementation routine of VLM method, the aircraft aerodynamic force and moment coefficients can be computed by integrating all the forces and relevant moments over all the panels.

The capability of calculating the stability derivatives, namely the first order derivatives of aerodynamic coefficients, is enabled by Tornado by performing a central difference approximation using the pre-selected state and disturbing it by a small amount, usually 0.5 degrees [32]. To enable the deflections of control surfaces for calculating the control derivatives, the classical horseshoe arrangement with three lines for one horseshoe vortex is replaced with a “vortex-sling” arrangement. Instead of three vortices for a classical horseshoe vortex, the new arrangement has seven vortices for every horseshoe vortex with identical strength as shown in Figure 3-8.

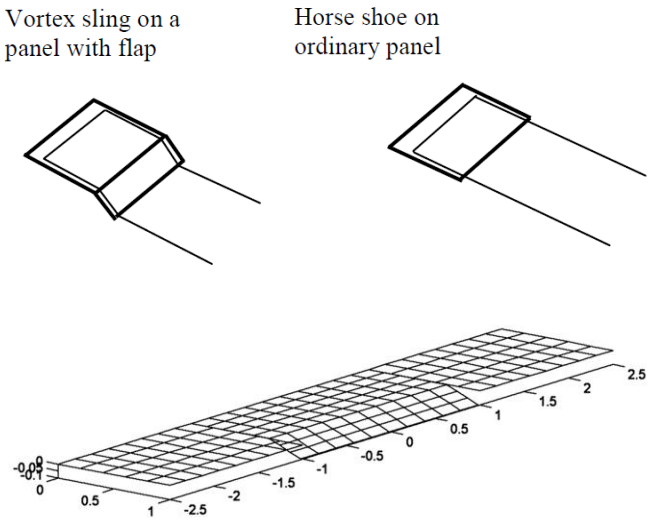

Figure 3-8 Vortex-sling definition and a representative flap deflection [30] [32]

VLM is based on inviscid and incompressible flow, therefore separation over wing and wave drag are not estimated. These simplifications result in linear aerodynamic performance of the analyzed aircraft configuration. Therefore the aerodynamic performance of an aircraft estimated with VLM algorithm is more accurate with small angles of attack under low speed flight conditions than large angles of attack or high speed flight conditions.

The conceptual aerodynamic tool Tornado calculates a set of aerodynamic coefficients based on VLM algorithm. Two main categories of inputs are required for Tornado: the aircraft geometry and the flight condition. The VLM algorithm is based on lifting surface theory and treat the aircraft geometry as a thin surface with camber information but without considering the thickness of the airfoils. Compressibility and viscosity of airflow is not taken into account due to the basis of lifting surface theory. Therefore flight speed and altitude have no influences on the estimated aerodynamic coefficients although they do affect the final aerodynamic forces and moments.

With the given aircraft geometry, Tornado divides the aerodynamic surfaces (including main wings and tails, as well as fuselage if it is geometrically modelled) into spanwise partitions and chordwise panels and applies the lifting surface theory on the generated panel lattice. Based on the way Tornado creates the geometrical model for aerodynamic calculation, the main aircraft geometry information required as inputs for Tornado is summarized in Table 3-1.

Table 3-1 Inputs of Tornado about aircraft geometry

	Aircraft geometry model information
1	Wing span, including number of partitions in spanwise direction
2	Wing chord, including number of panels in chordwise direction
3	Dihedral angles of wing partitions
4	Sweep angles of wing partitions
5	Flap of a wing partition. If flap exists, the dimensions and number of panels
6	Airfoils of wing partitions, including inner section and outer section of each partition

	Aircraft geometry model information
7	Taper ratio of each wing partition
8	Twist angles of each wing partition, including inner section and outer section

Tornado is capable of considering the taper, sweep, dihedral, twist, camber and kinks of a polyhedral wing planform as well as tails and fins. However it considers every aerodynamic surface as a thin plane thus the thickness of a wing is not taken into account. A panel lattice geometrical model of the analysed VELA2 configuration of this project, generated by Tornado, is shown in Figure 3-9.

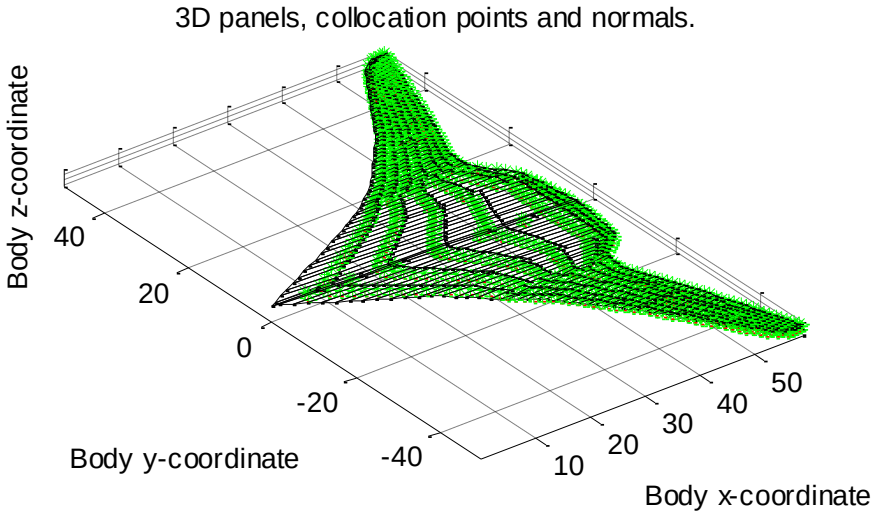

Figure 3-9 Panel lattice model of VELA2 generated by Tornado

The flight condition variables for the aerodynamic performance estimation with Tornado are listed in Table 3-2.

Table 3-2 Inputs of Tornado about flight condition

	Flight condition information
1	Angle of attack α
2	Angle of sideslip β
3	Airspeed V
4	Roll angular rate p
5	Pitch angular rate q
6	Yaw angular rate r

When a series of angles of attack α, sideslip angles β and airspeeds V are selected for the inputs of flight conditions of Tornado analysis, the corresponding outputs consist of all the force and moment coefficients and central difference derivatives w.r.t. three angular rates, angle of attack, sideslip angle, airspeed and the deflection angle of each ACS. For example if there are n_α angles of attack, n_β

sideslip angles, n_V airspeeds set as the flight conditions to be analyzed with an aircraft configuration with n_c control surfaces, the corresponding Tornado outputs are listed Table 3-3.

Table 3-3 Outputs of Tornado

Category	Coefficients	Description
Force and moment coefficients	C_L, C_D, C_S	Matrix, lift/drag/side force coefficient w.r.t each combination of α, β and V
	C_l, C_m, C_n	Matrix, rolling/pitching/yawing moment coefficient w.r.t each combination of α, β and V
	C_X, C_Y, C_Z	Matrix, force coefficient in X/Y/Z direction of the body reference frame w.r.t each combination of α, β and V
Central difference derivatives	$(C_L, C_D, C_S)_{p,q,r,\alpha,\beta,\delta}$	Matrix, lift/drag/side force derivatives for rolling/ pitching/ yawing rate, or α, β, or ACS deflection angle
	$(C_l, C_m, C_n)_{p,q,r,\alpha,\beta,\delta}$	Matrix, roll/pitch/yaw moment derivatives for rolling/ pitching/ yawing rate, or α, β, or ACS deflection angle
	$(C_X, C_Y, C_Z)_{p,q,r,\alpha,\beta,\delta}$	Matrix, force derivatives in X/Y/Z direction for rolling/ pitching/ yawing rate, or α, β, or ACS deflection angle

A representative pressure distribution, one of Tornado's output files, of VELA2 calculated by Tornado is shown in Figure 3-10.

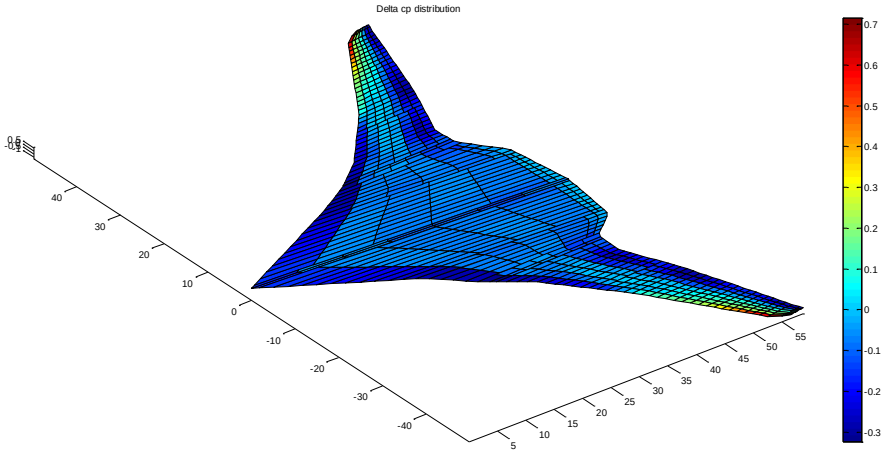

Figure 3-10 Pressure distribution of VELA2 calculated by Tornado

3.1.2.2 Drag estimations

Drag of an aircraft can be divided into several components. A typical drag classification is shown in Figure 3-11. Due to the neglect of compressibility and viscosity, Tornado is not able to estimate all components of the drag. Only induced drag is included in the results of VLM estimation. Therefore

additional drag estimation tools and modules are required for more accurate results, especially when drag is important for the simulation of thrust vectoring effects since the thrust required for steady trimmed flight is directly related to the drag of the corresponding flight condition, and the thrust vectoring moment available is in turn directly related to the thrust of vectoring nozzles. Friction drag, form drag (pressure drag), wave drag need to be estimated separately by separate tools and modules. For aircraft conceptual design and analysis, empirical methods of drag estimation with low fidelity can be used for fast assessment.

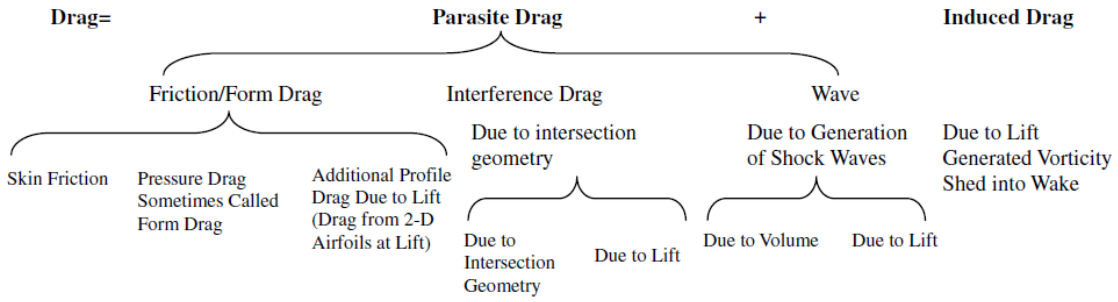

Figure 3-11 Typical drag breakdown terminology [33]

- Friction and form drag

A brief description of the methodology of friction/form drag estimation in this project is given in this section. The friction/form drag can be divided into three components: friction drag, pressure drag, and lift related profile drag. The third component is small and is sometimes neglected. The remaining two parts are addressed simultaneously. The friction /form drag are calculated with every component of the aircraft (wing, fuselage, nacelle etc.) with the following relation [33]

$$C_{D,F} = C_f FF \frac{S_{wet}}{S_{ref}} \tag{3.25}$$

where C_f is the flat-plate skin friction coefficient, FF is the form/shape factor of the component, and S_{wet}, S_{ref} are the respective wetted and reference area. For a BWB configuration the fuselage component is highly blended with the outer wing segments and is treated as part of the wing, therefore only the form factor of wing shape need to be found.

The skin friction coefficient for a flat plate is sorted into two categories [31]. For laminar flow

$$C_f = \frac{1.328}{\sqrt{\mathrm{Re}_c}} \tag{3.26}$$

where Re_c is the Reynolds number based on the chord length c. The MAC is used to calculate Re_c.

For turbulent flow the friction coefficient is given by:

$$C_f = \frac{0.074}{\mathrm{Re}_c^{1/5}} \tag{3.27}$$

For the estimation of friction drag, a combination of the skin friction coefficients of laminar flow and turbulent flow needs to be used, and estimation of the location of transition from laminar flow to turbulent flow needs to be considered.

Form factor FF represents the drag correction due to thickness and pressure drag. There are various ways of calculating the form factor. Some of the most well-known and validated models were developed by Hoerner, Torenbeek, Shevell, and Raymer [33]. Hoerner's wing form factor model is a function of the thickness ratio t/c:

$$FF_{wing} = 1 + 2\frac{t}{c} + 60\left(\frac{t}{c}\right)^4 \tag{3.28}$$

The wing form factor developed by Torenbeek is similar to that developed by Hoerner, only with different constants:

$$FF_{wing} = 1 + 2.7\frac{t}{c} + 100\left(\frac{t}{c}\right)^4 \tag{3.29}$$

In Shevell's model the free stream Mach number and the quarter-chord sweep angle $\Lambda_{c/4}$ is included:

$$FF_{wing} = 1 + \frac{\left(2 - M^2\right)\cos\Lambda_{c/4}}{\sqrt{1 - M^2\cos^2\Lambda_{c/4}}} \cdot \frac{t}{c} + 100\left(\frac{t}{c}\right)^4 \tag{3.30}$$

Raymer suggested a wing form factor model which takes the location of the airfoil maximal thickness $\left(x/c\right)_m$ into account:

$$FF_{wing} = \left[1 + \frac{0.6}{\left(x/c\right)_m} \cdot \frac{t}{c} + 100\left(\frac{t}{c}\right)^4\right] \cdot \left[1.34M^{0.18}\left(\cos\Lambda_m\right)^{0.28}\right] \tag{3.31}$$

where Λ_m is the sweep angle of the maximum thickness line.

A comparison among the above mentioned models of form factor, as shown in Figure 3-12, shows that for a typical airfoil the variation of form factor value from different models is less than a 10% difference. For the drag estimation tool VRaero used in this project, the wing form factor developed by Torenbeek is used.

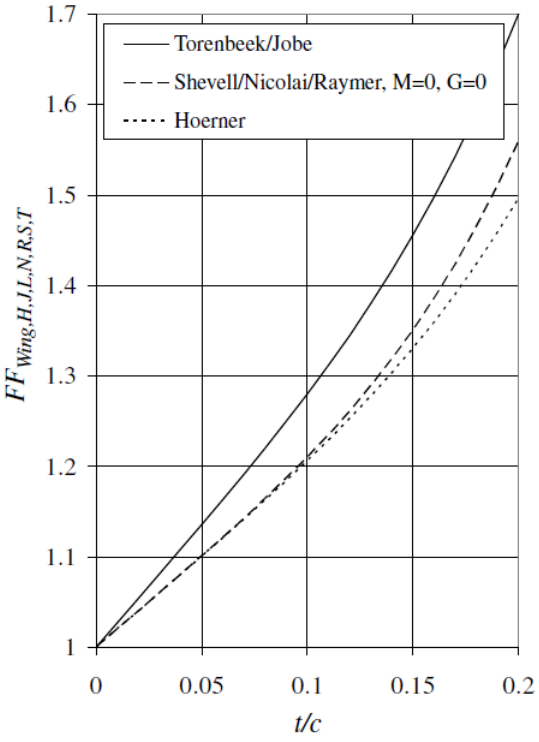

Figure 3-12 Comparison of wing form factors from different models [33]

- Wave drag

When an aircraft is flying above its critical Mach number the compressibility becomes non-negligible, and wave drag needs to be counted. The wave drag calculation in this project uses the following method [33]:

$$C_{dw} = \begin{cases} 0 & M \le M_{cr} \\ 20\left(M - M_{cr}\right)^4 & M > M_{cr} \end{cases} \tag{3.32}$$

where M_{cr} is the critical Mach number. The critical Mach number can be calculated from the drag divergence Mach number M_{DD}, with the following expression:

$$M_{cr} = M_{DD} - \sqrt[3]{\frac{0.1}{80}} \tag{3.33}$$

Equation (3.33) indicates that the critical Mach number is smaller than the drag divergence Mach number by a constant 0.108. The drag divergence Mach number can be calculated with the following equation:

$$M_{DD}\cos\Lambda_{0.5} + \frac{C_l}{10\cos^2\Lambda_{0.5}} + \frac{t/c}{\cos\Lambda_{0.5}} = \kappa_A \tag{3.34}$$

where $\Lambda_{0.5}$ is the mid-chord sweep angle and κ_A is the Korn factor. For supercritical airfoils $\kappa_A = 0.95$, and for conventional airfoils $\kappa_A = 0.87$.

By estimating the friction/form drag and wave drag with separate tools or modules, all the drag components listed in Figure 3-11 except for the interference drag are now considered. Interference drag of a conventional configuration consists of the interference between wings and fuselage, tails and fuselage, struts and wings. For a BWB configuration the interference drag is neglected due to the high blending between wings and fuselage and the absence of tails.

3.1.3 Mass and inertia

The mass prediction of an aircraft configuration during conceptual design phase is of importance for a viable design. However due to a lack of reference data, accurate mass estimation of a BWB configuration is difficult to be achieved. The mass and inertia estimation of the modified VELA2 configuration of this thesis project is carried out with an in-house tool developed by Till Pfeiffer from the Department of Integrated Aircraft Design of DLR, and is named BWBmass.

BWBmass is a conceptual mass and inertia estimation tool specialized for BWB configuration with updates from mass estimation methods for conventional configurations. It is a semi-geometrical tool making use of the component dimension information, and adjusting the results of conventional methods with constant factors. The areas of the wing sections, wing boxes and inner wing cabin are used to determine their masses, and the length of the cabin is used to determine the masses of the pressure walls and the cabin ribs. The mass of systems, furnishing and operator's items are calculated based on the number of passengers. The mass calculation of landing gear, pylon and power unit is based on statistics of existing conventional aircrafts [34].

Another BWB airframe mass prediction method was developed by D Howe [35]. The mass of the BWB airframe is predicted using an empirically weighted theoretical approach. Unlike the classification of conventional airframe components, Howe separates the airframe mass estimation of a BWB configuration into three functional components, the outer wing functional part, the inner wing functional part, and the fuselage functional part. The mass of each part consists of the primary structural mass and the additional penalty mass. Primary structural mass is estimated based on the materials required to resist the structural stress and the consideration of the stiffness. Penalties are added to the primary structural mass for departures from the ideal assumptions of primary structure and for the presence of additional structures such as the high lift devices and landing gears etc.

A comparison of the analysis results on a BWB configuration between the two BWB mass estimation methods shows that they produce very similar results as listed in Table 3-4. Though a full validation of the mass estimation methods of a BWB configuration is not possible at the current stage as no produced or flown BWB aircraft exists for reference, applications of the Howe method to several BWB concepts give reasons to believe that the introduced methods are acceptable for preliminary design purposes.

Table 3-4 Mass estimations with two different mass prediction methods [34]

Method	OEM [kg]	MTOM [kg]	Fuel Mass [kg]	OEM/MTOM
Howe	352550	683240	253510	0.516
BWBmass	355930	688460	255440	0.517

3.2 VELA2 configuration

The digital geometrical model of the VELA2 configuration is provided by the Department of Integrated Aircraft Design of DLR and used as the aircraft platform for the thrust vectoring control analysis in this thesis project. The VELA project is one of the European early research projects on flying wing/BWB configuration in the beginning of the 20th century. The aim of this project was to develop the capabilities of BWB configuration design and assessment in the areas of: aerodynamic performance, stability and control criteria, structure concept and weight, and the cabin design. The objectives of VELA project covers most of the critical disciplines of BWB concepts, and were divided into several work packages and worked out by collaborations among various aircraft manufactures and institutes. Part of the basic top level aircraft requirements (TLAR) are listed in Table 3-5. Like most of the other BWB concepts, the VELA2 configuration is aimed to be a long-haul transport aircraft with large passenger capacity.

Table 3-5 TLAR of VELA configurations [7]

TLAR	Values	Unit
Passenger capacity	~750	[--]
Freight capability	>10	[t]
Range capability	~7650	[nm]
Cruise Mach number	0.85	[--]
Initial cruise altitude	>35000	[ft]
Max operating altitude	>43000	[ft]

In the beginning of the VELA project, two initial BWB configurations, the VELA1 and VELA2, were designed. These two initial designs differ from each other by the level of blending between wing and central body and the longitudinal location of the wing on the central body. VELA1 has a high wing mounted in the front location of the central body, while VELA2 has a middle wing mounted at a very aft location of the central body. Both configurations have four engines mounted under the wing and two vertical tails at the trailing edge of the central body [7].

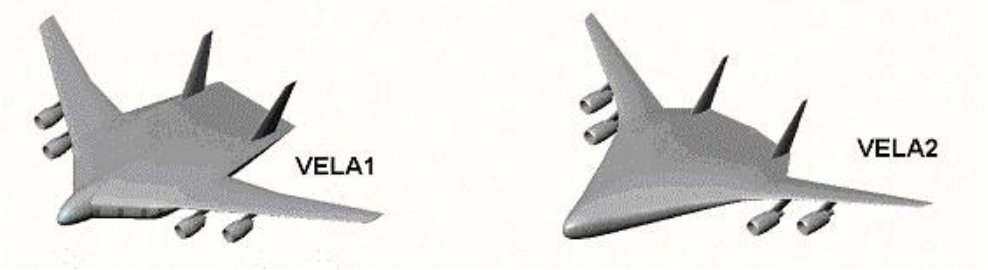

Figure 3-13 Two initial BWB configurations of the VELA project [7]

The initial two configurations are designed to be two extreme conditions with the awareness that stability and controllability may require rather different wing location in between the two extremes. Based on the results of different work packages of the VELA project, several configurations were interpolated between the VELA1 and VELA2 configurations. Integrating the feedbacks and recommendations from the initial two configurations and the interpolated configurations a refined VELA configuration, the VELA3, was designed at the end of the project as shown in Figure 3-14.

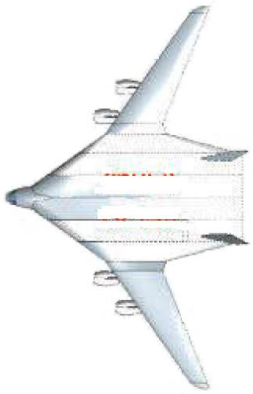

Figure 3-14 Refined VELA configuration: VELA3

The geometry model of VELA2 used in this project is without the components of vertical tails, engine nacelles and struts. The absence of vertical tails of the digital geometry leads to a lack of directional control derivatives and stability derivatives as well as under-estimated aircraft mass and drag. Since this thesis project is focusing on the longitudinal trimming, the lack of directional control derivatives has no significant influences on the control and trimming results. The absence of engine nacelles, struts, and the vertical tails results in a under estimation of the wetted area hence under estimation of drag. However compared to the total wetted are of this aircraft, and due to the requirements of the aerodynamic data with conceptual level, this discrepancy of wetted area is thought to be acceptable.

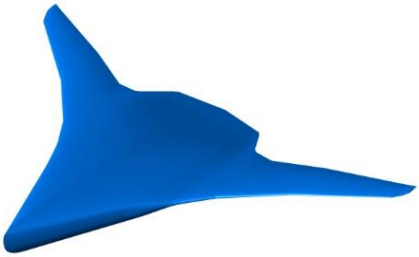

Figure 3-15 VELA2 digital geometry model (without engines, struts and vertical tails)

3.2.1 Initial VELA2 configuration

The VELA2 configuration from the European VELA project has four turbofan engines mounted under its outer wing and two vertical tails at the trailing edge of the inner fuselage as shown in Figure 3-13. Through the design of the initial two BWB configurations of the VELA project, the width of the aircraft and the leading edge sweep angle were prescribed and fixed during the configuration development. Compared to other VELA configurations, the main properties of VELA2 version are the very aft location of the outer wings w.r.t the inner fuselage, and a high level of blending between outer wings and inner fuselage. The main objects of the initial two VELA configurations were the study of aerodynamic effects. The main dimensions of VELA2 configuration is shown in Figure 3-16. The aircraft has a wing span of near 100 m, and length of 55.7 m of the inner fuselage. The CG location under OEM condition is at 34.23 m from the aircraft nose.

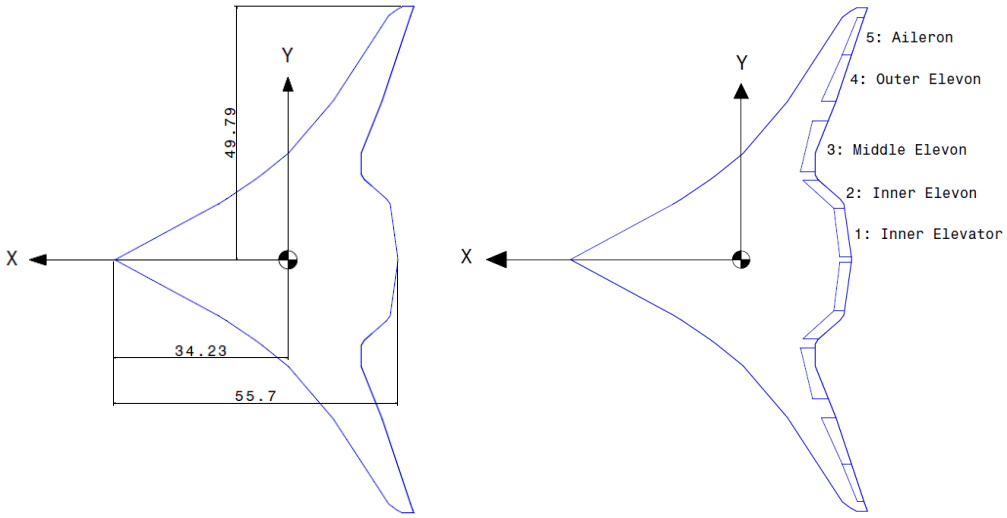

Figure 3-16 Planform dimensions and ACS distributions of VELA2

Without conventional empennages, VELA2 is controlled by control surfaces at the trailing edge of the main wings. There are five trailing edge control surfaces on each side of the main wing. According to the definition of VELA project, the most outer control surface on each side of the aircraft is purely used for rolling control, while the most inner control surface is assigned with only pitching control function. Three of the five control surfaces on each wing are assigned multiple functions for both pitching and rolling controls. The distribution of the trailing edge control surfaces is shown in Figure 3-16.

3.2.2 Modified VELA2 configuration

Thrust vectoring moments produced by vectoring nozzles are determined by both the thrust magnitude and the moment arms between vectoring nozzles and the CG of the aircraft. The initial VELA2 configuration from the VELA project has four engines mounted under the outer wings. Wing mounted engines result in a very short moment arms of the vectoring nozzles. Therefore in this thesis project the main modification of the VELA2 configuration is the relocation of the engines. Referring to

the Boeing's BWB project, with engines mounted above the trailing edge of the inner fuselage there are several advantages. The primary purpose of Boeing's project to have the engines installed above the trailing edge of the inner fuselage is to utilize the engine inlets for boundary layer suction in order to improve the aerodynamic performance of the upper surface of the inner fuselage [20]. Being installed above the trailing edge of the inner fuselage allows the engines to be closer to the symmetry plane of the aircraft, thus reduces the undesired moments under engine out conditions. For VELA2 configuration used in this thesis project, with engines moved to the upper surface of the trailing edge of the inner fuselage from under the wings, it is possible to get the maximal available moments from vectoring nozzles, therefore maximize the thrust vectoring efficiency for control analysis.

Base on the availability of engine performance map which is required for the flight mechanics analyses, an engine performance model of the MOB project is used in this thesis project. In the MOB project, an engine performance map of the scaled Pratt & Whitney JT9D turbofan engine is used. The engine performance map is calculated with Gas turbine Simulation Program (GSP) developed by the Dutch Aerospace Center (NLR). When the engine PLA is set to be 1.15 times of the maximum PLA position of the initial JT9D engine, the scaled engine has a maximum gross thrust of 350.47 kN as shown in Figure 3-17.

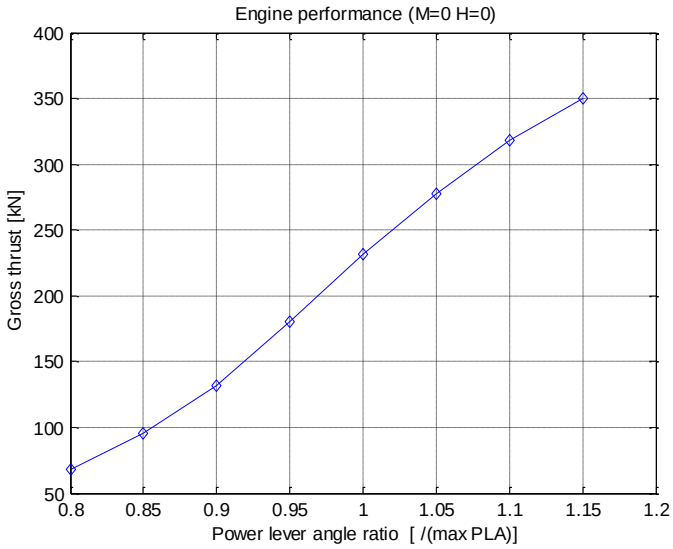

Figure 3-17 Ground performance of the scaled JT9D

When the scaled JT9D turbofan engine model is selected for the modified VELA2 configuration, the number and location of engines need to be determined. Determination of the number of engines is based on the estimation of required thrust-to-weight ratio at take-off using a method given by Jan Roskam [36]. According to Roskam's theorems, there are several ways for preliminarily sizing the takeoff thrust of an aircraft. For example, the aircraft needs to be designed to meet the performance requirements in following categories:

- Stall speed
- Takeoff field length
- Landing field length
- Cruise speed (sometimes maximum speed)
- Climb rate (all engines operating (AEO) and one engine inoperative (OEI))

- Time to climb to some altitude
- Maneuvering

The takeoff field length requirement from the Federal Aviation Regulations Part 25 (FAR 25) is chosen to calculate the required takeoff thrust of VELA2 for the determination of engine number with a given engine performance map.

The takeoff field length s_{TOFL} of an airplane is proportional to its respective takeoff wing loading $(W/S)_{TO}$, takeoff thrust-to-weight ratio $(T/W)_{TO}$ and maximum takeoff lift coefficient $(C_{L,\max})_{TO}$. The relation between the takeoff field length and the above mentioned parameters can be expressed as:

$$s_{TOFL} \propto \frac{(W/S)_{TO}}{\sigma (C_{L,\max})_{TO} (T/W)_{TO}} = TOP_{25} \tag{3.35}$$

where TOP_{25} is the takeoff parameter for FAR 25 certified airplanes, and σ is the air density ratio compared to the air density at sea level.

The takeoff field length of A380, which has the closest MTOW to the VELA configurations among the existing transports, is 2880 m [37]. Statistical data shows that for conventional transports the takeoff distance is normally around 2000m, as shown in Figure 3-18.

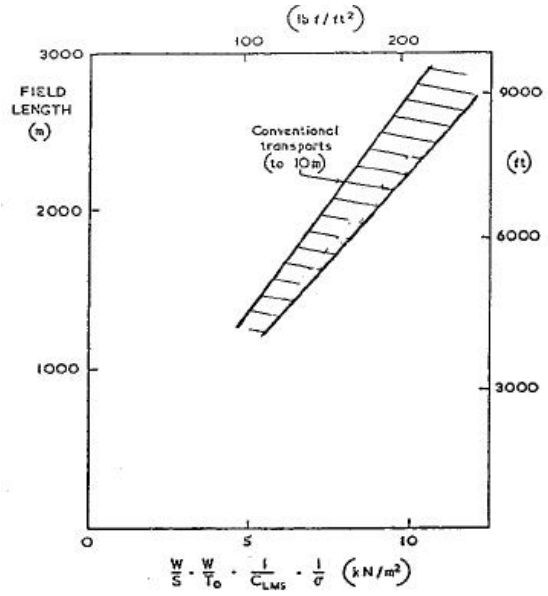

Figure 3-18 Takeoff distance of conventional transports [38]

Based on the statistical data, an approximate takeoff field length of 2000 m is chosen for the conceptual thrust requirement analysis of VELA2 in this project.

$$s_{TOFL} < 2000 \ \ m \tag{3.36}$$

The proportion between the takeoff field length and the takeoff parameter can be found from Figure 3-19. The slope of the interpolated line is 37.5.

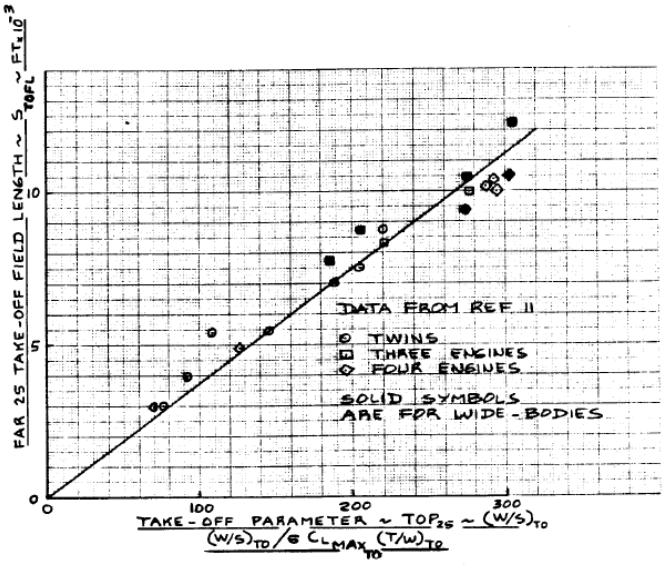

Figure 3-19 Effect of takeoff parameter on takeoff field length [36]

Therefore equation (3.35) can be written as:

$$s_{TOFL} = 37.5\frac{(W/S)_{TO}}{\sigma(C_{L,\max})_{TO}(T/W)_{TO}} = 37.5TOP_{25} \tag{3.37}$$

At sea level, the air density ratio σ is 1.0. Typical values for the maximum takeoff lift coefficient $(C_{L,\max})_{TO}$ of different aircraft types can be found from Table 3-6, where $(C_{L,\max})_L$ is the maximum landing lift coefficient.

Table 3-6 Typical values of maximum lift coefficient [36]

Airplane Type	$C_{L,\max}$	$(C_{L,\max})_{TO}$	$(C_{L,\max})_L$
1. Homebuilts	1.2 - 1.8	1.2 – 1.8	1.2 – 2.0
2. Single Engine Propeller Driven	1.3 - 1.9	1.3 – 1.9	1.6 – 2.3
3. Twin Engine Propeller Driven	1.2 - 1.8	1.4 – 2.0	1.6 – 2.5
4. Agricultural	1.3 - 1.9	1.3 – 1.9	1.3 – 1.9
5. Business Jets	1.4 - 1.8	1.6 – 2.2	1.6 – 2.6
6. Regional Turboprop	1.5 - 1.9	1.7 – 2.1	1.9 – 3.3
7. Transport Jets	1.2 - 1.8	1.6 – 2.2	1.8 – 2.8
8. Military Trainers	1.2 - 1.8	1.4 – 2.0	1.6 – 2.2
9. Fighters	1.2 - 1.8	1.4 – 2.0	1.6 – 2.6
10. Military Patrol, Bomb and Transports	1.2 - 1.8	1.6 – 2.2	1.8 – 3.0
11. Flying Boats, Amphibious and Float	1.2 - 1.8	1.6 – 2.2	1.8 – 3.4
12. Supersonic Cruise Airplanes	1.2 - 1.8	1.6 – 2.0	1.8 – 2.2

The maximum takeoff weight of VELA2 is calculated by BWBmass to be 616698 kg as will be discussed in section 5.3. Attention needs to be paid to the value of wing planform area for calculating the wing loading. Since for a BWB configuration both the outer wing and the inner fuselage are lift generating surfaces, the wing loading needs to be calculated based on the entire planform area of a BWB aircraft. The planform area of VELA2 is 1922.23 m^2.

A conservative maximum takeoff lift coefficient of VELA2 is chosen to be 1.8 based on the statistical data given in Table 3-6. Equation (3.37) can be written as:

$$TOP_{25} = s_{TOFL}/37.5 = \frac{(W/S)_{TO}}{\sigma (C_{L,\max})_{TO} (T/W)_{TO}} \tag{3.38}$$

Note that the unit of TOP 25 is lbs/ft^2 in equation (3.38).

Based on the FAR 25 requirements, the takeoff parameter is calculated to be

$$TOP_{25} = s_{TOFL}/37.5 = 2000 \times 3.28/37.5 = 174.93 \ lbs/ft^2 = 854.11 \ kg/m^2 \tag{3.39}$$

Substitute equation (3.39) into equation (3.38), the takeoff thrust-to-weight ratio of VELA2 is

$$(T/W)_{TO} = 0.209 \tag{3.40}$$

Figure 3-20 shows the range of values of takeoff wing loading, takeoff thrust-to-weight ratio and takeoff maximum lift coefficient for which the field length requirement is satisfied. From Figure 3-20 it can be seen that the calculated takeoff thrust-to-weight ratio of VELA2 is well within the range of the values of existing aircrafts.

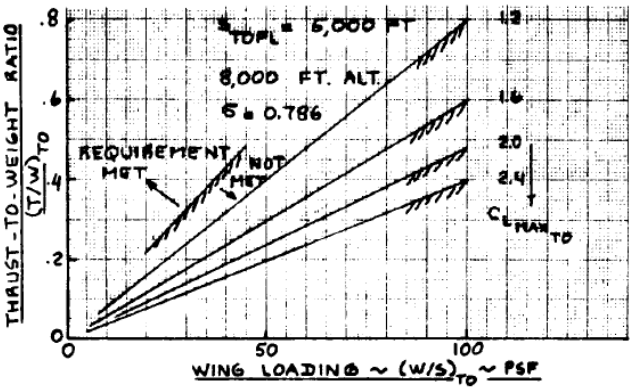

Figure 3-20 Thrust-to-weight ratio w.r.t. wing loading and max take-off lift coefficient [36]

Then the required thrust for takeoff, which is also the maximum thrust requirement of a transport aircraft, of VELA2 is:

$$T_{TO,required} = (T/W)_{TO} \cdot MTOW = 128692.97 \ kgf = 1261.19 \ kN \tag{3.41}$$

With four scaled JT9D turbofan engines from the MOB project with a maximum ground thrust of 350.47 kN, the total available thrust for takeoff is

$$T_{TO,available} = 1401.88 \ kN \tag{3.42}$$

The available takeoff thrust shows that four scaled JT9D turbofan engines are adequate for VELA2 configuration. Therefore the number of scaled JT9D engines for the modified VELA2 configuration of this thesis project is set to 4.

As has been mentioned previously, the location of the engines are moved from under the wings of the initial VELA2 configuration to be above the trailing edge of the inner fuselage. For calculating the moments of vectoring thrust the locations of engines need to be quantified. This process is directly based on the objective of maximizing the moment arms of vectoring nozzles, while taking into account the feasibility of engine installations. Considering the dimensions of VELA2 and JT9D turbo engines while ensuring that the hot exhausts from nozzle exits do not damage the fuselage structure, the resulting engine locations are determined as shown in Figure 3-21 and Figure 3-22.

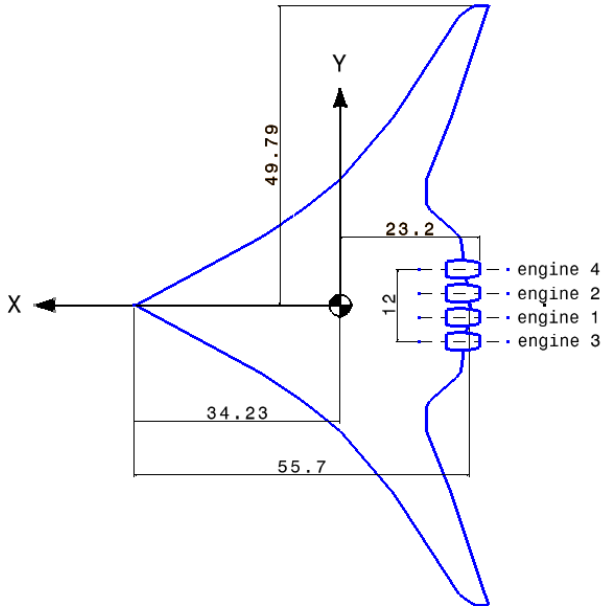

Figure 3-21 Relocation of the engines, top view

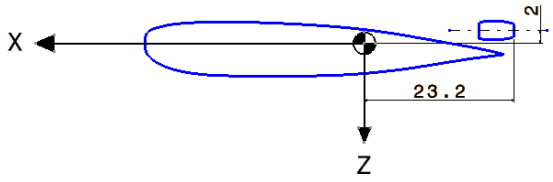

Figure 3-22 Relocation of the engines, side view

The engines are located above the upper surface of the trailing edge of the inner fuselage. Distance between engine nozzle exits and the CG of the aircraft is 23.2 m. The nozzle exits are about 1.7 m aft from the trailing edge of the inner fuselage for protecting the fuselage structure. The centerlines of the engines are 2 meters above the center line of fuselage based on the consideration of isolating the boundary layer influences on the uniformity of engine inlet flow. Although higher centerlines of the engines cause negative effects on thrust vectoring controls as they produce inherent nose down pitching moments which may lead to penalties on trim drag and a compensation of nose up thrust vectoring controls, the relatively small vertical distance between the engine centerlines and aircraft fuselage centerline is acceptable. Lateral distances between engines are not strict when lateral thrust

vectoring control is not considered in this project. The lateral locations are arranged in the way that the engines are within the area of flat trailing surface of the inner fuselage.

The engine type and engine locations are the only modifications to the initial VELA2 configuration without regard to the absence of vertical tails of the digital model provided for this thesis project. The aerodynamic control surfaces and their effectiveness are kept identical to their initial designs.

4 Thrust vectoring modelling

The flight mechanics modeling of thrust vectoring is essential for the performance analyses of thrust vectoring controls. In a flight mechanics toolbox the modeling of thrust vectoring contains two parts, one is the vectoring nozzle performance and the other one is the control of vectoring nozzles.

The first part of thrust vectoring modeling is the nozzle thrust calculation considering nozzle deflections. When engine nozzles are mechanically deflected, the internal flow field of the engine nozzle is forced to change. The change of the exhausting flow path will result in a loss of nozzle performance, i.e. thrust loss. For most of the thrust vectoring types as listed in section 2 the effective thrust deflection angle is smaller than the geometrical deflection angle of the nozzle. The loss in nozzle thrust and the deviation of effective deflection angle from geometrical deflection angle both have influences on the performance of thrust vectoring control. Therefore these two factors need to be examined before carrying out the thrust vectoring control analysis. When the relationship between thrust loss and nozzle deflection angle, as well as the relationship between effective thrust deflection angle and geometrical nozzle deflection angle are found, they will be mathematically modeled in the Phalanx flight mechanics toolbox for thrust vectoring control analysis.

The mass increment of engine nozzles due to the application of thrust vectoring technology is neglected in this thesis project. No published papers and materials have been found on the topic of nozzle mass penalty due to the application of thrust vectoring technology. Compared to the tremendous maximum take-off weight of the VELA2 and total weight of the engine, the weight increment of engine nozzle due to thrust vectoring application is a small amount and is negligible for conceptual analysis. For detailed flight mechanics analysis it is necessary to take the mass increment of vectoring nozzles into account.

The second part of thrust vectoring modeling is the control of vectoring nozzles. Similar to the control of aerodynamic control surfaces, when multiple vectoring nozzles are deflected simultaneously a proper control allocation algorithm needs to be applied on the distribution of nozzle deflections. When proper integrated control of aerodynamic control surfaces and vectoring nozzles are to be developed, separated control of the two control forces and comparisons between their effectiveness become a primary choice of examining the effects and effectiveness of thrust vectoring control. Therefore an independent module for thrust vectoring control from the module for ACS control is developed and implemented in Phalanx. Different combinations between ACS and vectoring nozzles are tested for trimming VELA2 under various steady trimmed flight conditions in order to extensively test the effectiveness of thrust vectoring control.

4.1 Thrust forces and moments modeling

There are several ways of analyzing the engine thrust loss due to nozzle deflections, including CFD, experiment tests and analytical calculation. For real time implementation in a flight mechanics toolbox analytical modeling is the most appropriate choice among the three methods due to its cheap costs and fast calculation. Erich Wilson from the Israel Institute of Technology has worked out an analytical solution of thrust coefficient calculation of vectoring nozzles. This method is based on an analytical

nozzle performance model which takes into account the nozzle section areas and the surface roughness. With the mechanical deflections of vectoring nozzles, the section areas will change simultaneously. The variation of section area parameters in the nozzle thrust coefficient equation reflects the effects of thrust deflections on nozzle thrust coefficients [6].

4.1.1 Thrust coefficient

Erich's theorem of thrust coefficient of vectoring nozzles is based on an analysis of the compressible flow equations of the nozzle internal flow, taking into account the friction and area change driving potentials [39]. Application of compressible flow equations in nozzles allows the generalized differential equations to be reduced to two driving potential terms, the area change and friction. The differential form of internal compressible flow equations concerning the Mach number, section areas, velocities while taking into account the friction of nozzle walls are:

$$\frac{\mathrm{d}M^2}{M^2} = -\frac{2\zeta}{1-M^2}\frac{\mathrm{d}A}{A} + \frac{\gamma M^2 \zeta}{1-M^2}\frac{4f}{D}\mathrm{d}x \tag{4.1}$$

$$\frac{\mathrm{d}V}{V} = -\frac{1}{1-M^2}\frac{\mathrm{d}A}{A} + \frac{\gamma M^2}{2\left(1-M^2\right)}\frac{4f}{D}\mathrm{d}x \tag{4.2}$$

where $\zeta = 1 + \frac{\gamma - 1}{2}M^2$, and

A : nozzle section area

D : nozzle section diameter

f : friction factor of the nozzle wall

M : Mach number of the nozzle internal flow

V : velocity of nozzle internal flow

γ : ratio of specific heat

Consider the throat of an axisymmetric nozzle to be at the origin along nozzle axis x, any given cross-section area can be referenced to the nozzle throat radius r_0 through the divergence angle α, which becomes negative if the duct is converging towards the throat [39],

$$A = \pi\left(r_0 + x\tan\alpha\right)^2 \tag{4.3}$$

Note that the nozzle divergence angle along the length of the nozzle does not have to be a constant. It can be either constant, or linear, or any other forms w.r.t the section location of the nozzle.

The differential form of the nozzle section area is

$$\mathrm{d}A = 2\pi\left(r_0 + x\tan\alpha\right)\left(\tan\alpha\cdot\mathrm{d}x + x\,\mathrm{d}\left(\tan\alpha\right)\right) \tag{4.4}$$

Equation (4.4) is difficult to be used in analytical integrations. Simplifications need to be considered. For a small $\mathrm{d}x$,

$$\mathrm{d}x \gg \mathrm{d}(\tan\alpha) \tag{4.5}$$

Then equation (4.4) can be reconstructed as

$$\begin{aligned}\mathrm{d}A &= 2\pi\left(r_0 + x\tan\alpha\right)\tan\alpha\cdot\mathrm{d}x \\ &= 2\pi\left(r_0 + x\tan\alpha\right)^2\frac{\tan\alpha\cdot\mathrm{d}x}{r_0 + x\tan\alpha} \\ &= 2A\frac{\tan\alpha\cdot\mathrm{d}x}{r_0 + x\tan\alpha}\end{aligned}$$

The differential form of the relation between nozzle section area and nozzle divergence angle is

$$\frac{\mathrm{d}A}{A} = \frac{2\tan\alpha}{r_0 + x\tan\alpha}\mathrm{d}x \tag{4.6}$$

By substituting equation (4.6) into equation (4.1) and equation (4.2), the respective analytical solutions can be derived as:

$$\frac{A_2}{A_1} = \frac{M_1}{M_2}\left(\frac{\zeta_2}{\zeta_1}\right)^{(\gamma+1)\tan\alpha/(2\phi)}\left(\frac{\psi_2}{\psi_1}\right)^{(f\gamma-2\tan\alpha)/(2\phi)} \tag{4.7}$$

$$\frac{V_2}{V_1} = \frac{M_2}{M_1}\left(\frac{\zeta_1}{\zeta_2}\right)^{\frac{1}{2}} \tag{4.8}$$

where $\phi = f\gamma + (\gamma - 1)\tan\alpha$.

The reason that the analytical solutions of nozzle section area, Mach number and flow velocity of compressible flow with friction influences are introduced here is that, the conventional nozzle thrust coefficient is related to the nozzle exit area and exhaust flow velocity as given in equation (4.9), and nozzle deflections will change the effective section areas of an engine nozzle and consequently change the internal flow Mach number and flow velocity, therefore in this way it is possible to connect the nozzle thrust coefficient with nozzle deflections. The mechanical implementation of nozzle deflections are not the focus of this project and will not be discussed here. It is simply assumed that the realization of nozzle deflections are technically possible without much nozzle mass penalties.

It is necessary to introduce the influences of nozzle deflections on effective nozzle section areas. As the flight mechanics analysis of this thesis project is conducted on a transport aircraft with turbofan engines, the engine nozzles are assumed to have fixed geometrical areas, but the positions of nozzle throat and exit are controllable on both lateral (δ_y) and vertical (δ_z) directions. With the nozzle deflections the effective section areas are changed and the nozzle thrust are affected in this way. The geometrical area and effective area of an engine nozzle are defined by Erich [6]:

Geometrical: the geometrical attributes include the shape, size, pattern, or measure of any physically existing part of the hardware such as flaps, rings, levers, actuators, etc. In other words, it is physically tangible and solid.

Effective: the effective attributes are not solid components of the nozzle. These are the characteristics describing the actual path and behavior of the fluid in a nozzle.

The geometric and effective section areas of a convergent-divergent (CD) nozzle is represented in a schematic diagram below. In which A_8 and A_9 represent the respective geometrical throat and exit areas, A_8' and A_9' represent the respective effective throat and exit areas. δ_v and δ_y are the nozzle deflection angles in Z and Y directions of the aircraft body coordinate system. In this report δ_v and δ_z both refers to the nozzle deflections in the Z direction of aircraft body coordinate system.

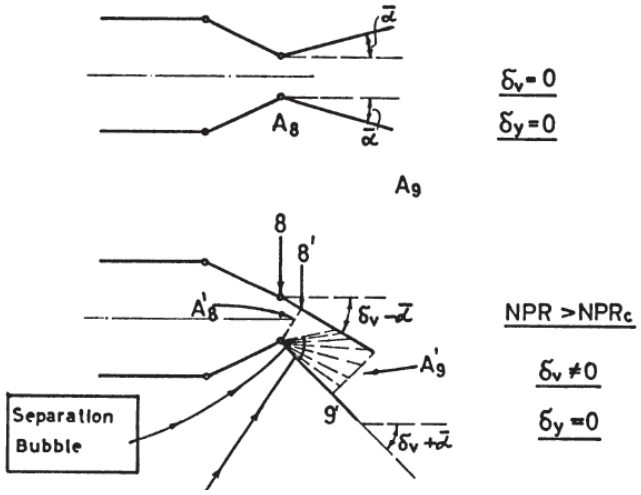

Figure 4-1 Geometrical and effective nozzle section areas [40]

The gross thrust coefficient equation of a conventional turbo engine is given by:

$$C_{fg} = \frac{F_a}{F_i} = \frac{\dot{m}_a V_e + A_e \left(P_e - P_0 \right)}{\dot{m}_i V_{ei}} \tag{4.9}$$

where

A_e : geometrical nozzle exit area

F_a : actual thrust

F_i : ideal thrust

$\dot{m}_a$: actual nozzle mass flow rate

$\dot{m}_i$: ideal nozzle mass flow rate

V_e : actual internal flow velocity at nozzle exit section

V_{ei} : ideal internal flow velocity at nozzle exit section

With the introduction of geometrical and effective nozzle section areas, and by substituting the relations of section areas, Mach numbers, velocities of the nozzle internal flow as depicted in equation (4.7) and (4.8) into the gross thrust coefficient equation of a conventional nozzle as recalled in equation (4.9) and with derivations, an important formulation of the thrust coefficient, which takes into account the geometrical and effective areas as well as the flow Mach numbers of nozzle sections is constructed by Erich as shown in equation (4.10) [39].

$$C_{fg} = \frac{A_t^E}{A_t^G}\left[\frac{M_{a,e}}{M_{i,e}}\sqrt{\frac{\zeta_i}{\zeta_a}} + \frac{A_e^E}{A_t^E}\frac{\sqrt{\zeta_i\left(\frac{\gamma+1}{2}\right)^{\frac{\gamma+1}{\gamma-1}}}}{\gamma M_{i,e}}\left(\frac{p_e}{p_0}-1\right)\right] \tag{4.10}$$

where

A_t^E : effective area at nozzle throat section

A_t^G : geometrical area at nozzle throat section

$M_{a,e}$: actual Mach number at nozzle exit section

$M_{i,e}$: ideal Mach number at nozzle exit section

p_e : static pressure at nozzle exit section

p_0 : ambient static pressure

In order to quantify the effects of nozzle deflections on the thrust coefficient of engine nozzles, the relations between effective and geometrical areas of nozzle sections are given by Benjamin Gal-Or [40] as given in equation (4.11). This simple relation is easy to understand when examining Figure 4-1.

$$\begin{cases} \dfrac{A_t^E}{A_t^G} = \cos\delta_y \cdot \cos\delta_z \\ \dfrac{A_e^E}{A_e^G} = \cos\delta_y \cdot \cos\delta_z \end{cases} \tag{4.11}$$

The reason that the relation indicated in equation (4.11) applies to both the throat and exit sections is that, it is intended to maintain the predetermined area ratio during nozzle deflections for keeping the initial optimized nozzle performance. Therefore the effective area ratio when nozzle is deflected is equal to the geometrical area ratio when nozzle is not deflected.

$$A_e'/A_t' = A_e/A_t \tag{4.12}$$

A more robust and accurate relation is introduced by V. Sherbaum, by multiplying a factor S [41]

$$\begin{cases} \dfrac{A_t^E}{A_t^G} = \cos\delta_y \cdot \cos\delta_z \cdot S \\ \dfrac{A_e^E}{A_e^G} = \cos\delta_y \cdot \cos\delta_z \cdot S \end{cases} \tag{4.13}$$

$$S = \left(\cos^2\delta_y + \sin^2\delta_y \cos^2\delta_z\right)^{-\frac{1}{2}} \tag{4.14}$$

Substituting equation (4.13) into (4.10), the thrust coefficient considering nozzle deflection angles becomes:

$$C_{fg} = \left[\frac{M_{a,e}}{M_{i,e}}\sqrt{\frac{\zeta_i}{\zeta_a}} + \frac{A_e^E}{A_t^E}\frac{\sqrt{\zeta_i\left[(\gamma+1)/2\right]^{\gamma+1/\gamma-1}}}{\gamma M_{i,e}}\left(\frac{p_e}{p_0}-1\right)\right]\cdot\cos\delta_y\cdot\cos\delta_z\cdot S \tag{4.15}$$

Finally the nozzle thrust coefficient is analytically connected to the nozzle deflection angles. The thrust coefficient introduced in equation (4.15) is applicable to nozzles no matter thrust vectoring is utilized or not. When nozzles are not deflected, the condition simply goes back to a conventional nozzle and can be treated as a particular thrust vectoring condition with nozzle deflection angles equal to zero.

Erich made comparisons among the analytical results derived by himself, numerical results and experiment results as shown in Figure 4-2. The comparisons show satisfactory accuracy of the analytical modeling method. Under low nozzle pressure ratio (NPR) conditions, the deviation of analytical results from the experimental results is about 2%, while under high NPR conditions the deviation is less than 1%. Three nozzle deflection angles (10°, 20° and 30°) are analyzed. The decrement of thrust coefficient w.r.t the increment of deflection angle is observed with the analytical modeling results in Figure 4-2.

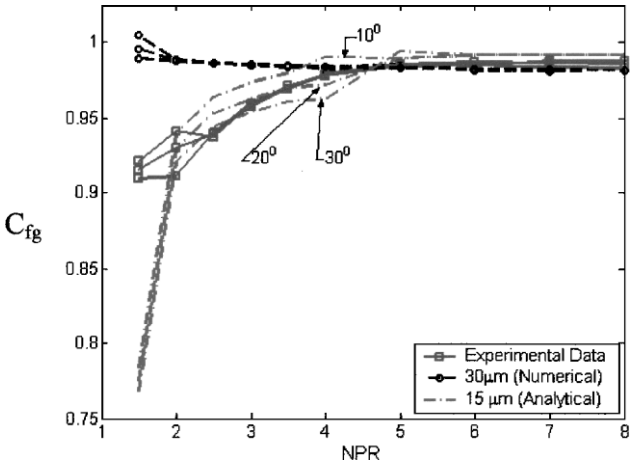

Figure 4-2 Verification of the analytical solution [39]

Equation (4.15) is derived for a convergent-divergent nozzle and is also valid for a pure convergent nozzle. For a pure convergent nozzle as shown in Figure 4-3, which is implemented on most of the civil transport aircrafts, the throat section is also the exit of the nozzle and the thrust coefficient equation becomes

$$C_{fg} = \left[\frac{M_{a,e}}{M_{i,e}} \sqrt{\frac{\zeta_i}{\zeta_a}} + \frac{\sqrt{\zeta_i \left[(\gamma+1)/2 \right]^{\gamma+1/\gamma-1}}}{\gamma M_{i,e}} \left(\frac{p_e}{p_0} - 1 \right) \right] \cdot \cos\delta_y \cdot \cos\delta_z \cdot S \tag{4.16}$$

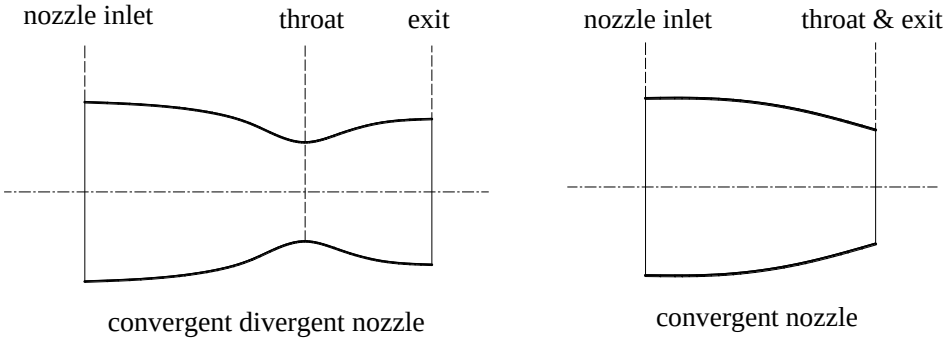

Figure 4-3 Convergent-divergent and pure convergent nozzles

With the engine performance map of scaled JT9D from the MOB project for this thesis project, the information available within the performance map contains the engine gross thrust, net thrust, fuel consumption etc. w.r.t a set of working ambient altitude, Mach number and PLA. The requirements of nozzle exit actual Mach number, ideal Mach number and nozzle exit static pressure for calculating the thrust coefficient with equation (4.15) complicate the problem. Therefore a simplification is made to equation (4.16). It is assumed that the Mach number and static pressure of the internal flow of a pure convergent nozzle are not affected by the nozzle deflections. With this assumption the terms within the square brackets of equation (4.16) is identical to that of a conventional convergent nozzle. Then equation (4.16) can be expressed simply as a multiplication between the thrust coefficient of a conventional convergent nozzle and the deflection factor, which is

$$C_{fg,TV} = C_{fg,C} \cdot \xi \tag{4.17}$$

Where ξ represents the deflection factor and is given by:

$$\xi = \cos\delta_y \cdot \cos\delta_z \cdot S \tag{4.18}$$

and

$C_{fg,C}$: nozzle thrust coefficient of a conventional nozzle

$C_{fg,TV}$: nozzle thrust coefficient of a vectoring nozzle

With the simplified relation, the thrust loss due to nozzle deflections is shown in Figure 4-4. The thrust loss at 20 degrees of nozzle deflection is around 6%, which is close to Erich's results for a nozzle with NPR around 2.0 and deflection angle of 20° as shown in Figure 4-2.

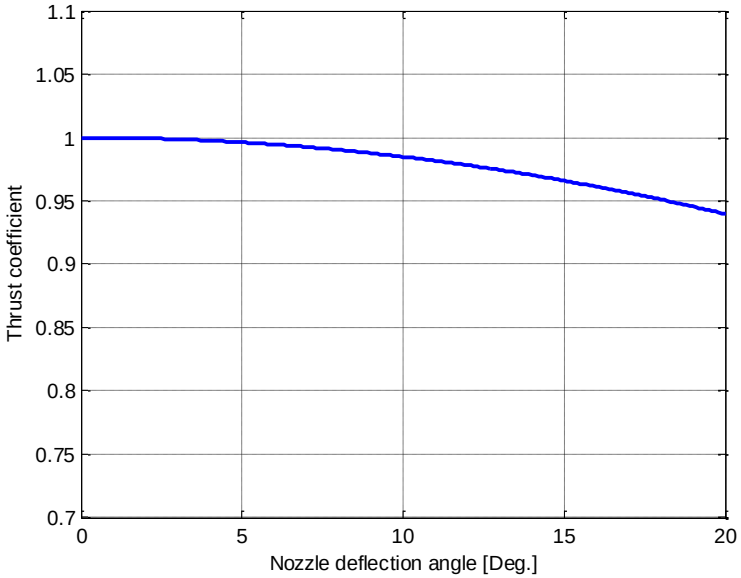

Figure 4-4 Thrust coefficient w.r.t nozzle deflection angle

With equation (4.17) it is now possible to calculate the gross thrust of a vectoring nozzle based on the gross thrust of a conventional nozzle by multiplying the deflection factor ξ.

$$F_{g,TV} = F_{g,C} \cdot \xi \tag{4.19}$$

where

$F_{g,C}$: gross thrust of conventional nozzle

$F_{g,TV}$: gross thrust of vectoring nozzle

4.1.2 Effective vectoring angle

During nozzle deflections the thrust deflection angle is not identical to the geometrical nozzle deflection angle similar to the flow over an airfoil. The stream line of the flow over an airfoil deviates from the shape of an airfoil due to the increment of boundary layer thickness and flow separation downstream the flow direction. For a convergent-divergent nozzle, Erich Wilson gives an equation for effective vectoring angle prediction in axisymmetric nozzles:

$$\delta^E = \arccos\left(\frac{r_e^E}{r_e^G}\right) \tag{4.20}$$

where

δ^E : effective nozzle deflection angle

r_e^E : effective nozzle exit radius

r_e^G : geometrical nozzle exit radius

The equation is not based on boundary layer thickness and flow separation estimation. It just simply builds the relation between the effective deflection angle and effective nozzle section area. With the equation given by Erich, the effective deflection angle has a slight deviation from the geometrical deflection angle as can be observed from Figure 4-5.

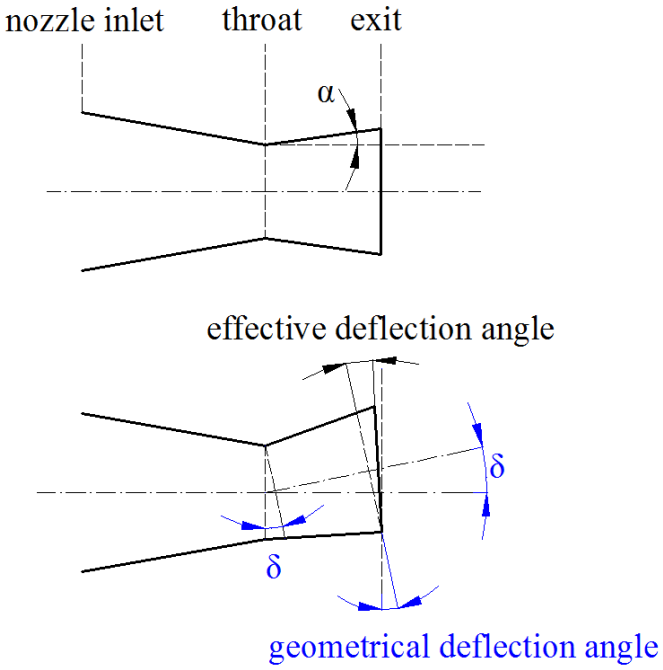

Figure 4-5 Definition of nozzle deflection angles

However, the analytical approximation of the effective vectoring angle derived by Erich Wilson has several simplifications. A credible relation between the effective deflection angle and geometrical deflection angle needs to be built up by experimental tests or high fidelity CFD results. Benjamin indicated that for the 2D-CD (2 Dimensional Convergent-Divergent) type of nozzles the difference between effective deflection angle and geometrical deflection angle is quite small and consequently negligible in conceptual design estimations. For instance the difference between effective deflection angles and geometrical deflection angles varies from 4 degrees, at internal subsonic conditions, to 1 degree in supersonic conditions [40]. Some experimental results on the effective deflection angles of vectoring nozzles w.r.t various NPR are shown in Figure 4-6. Under high NPR conditions the deviation of deflection angle is smaller than the deviation under low NPR conditions. Since the flight mechanics analysis in this thesis project is with conceptual fidelity level, the differences between effective vectoring angles and geometric vectoring angles are neglected.

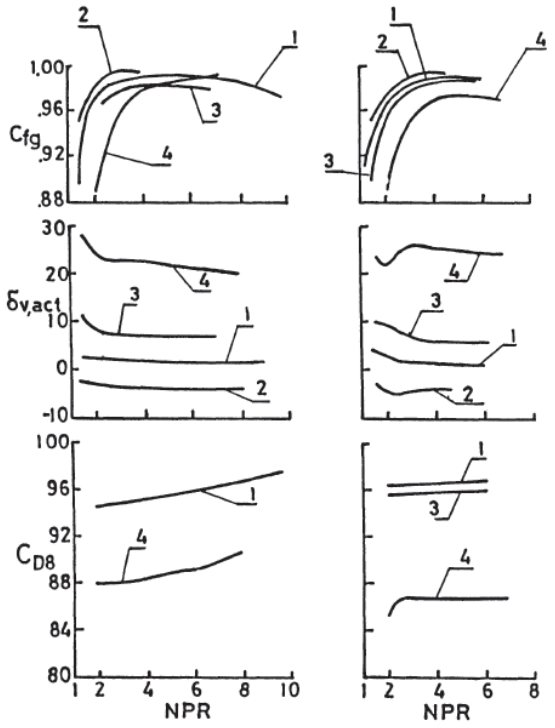

Figure 4-6 Actual nozzle deflection angle w.r.t. NPR [40]

4.1.3 Thrust forces and moments

Forces and moments produced by every aircraft component in three directions of the aircraft coordinate system, including thrust forces and moments produced by engines, need to be calculated for solving the equations of motion during the flight mechanics analyses. The components of gross thrust of the vectoring nozzles in three directions of the body coordinate system are calculated with the following equations:

$$\begin{cases} F_{g,x} = F_{g,TV} \cdot \cos\delta_y \cdot \cos\delta_z \cdot S \\ F_{g,y} = F_{g,TV} \cdot \sin\delta_y \cdot \cos\delta_z \cdot S \\ F_{g,z} = F_{g,TV} \cdot \cos\delta_y \cdot \sin\delta_z \cdot S \end{cases} \tag{4.21}$$

where $F_{g,x}$, $F_{g,y}$ and $F_{g,z}$ are the respective gross thrust components in X, Y and Z direction of the body coordinate system. The database of the gross thrust of conventional nozzle is already prepared in the format of lookup table for different engine working conditions. The effects of nozzle deflections are added to the initial engine thrust. Then the resulted vectoring thrust components and the corresponding moments are calculated.

The thrust and drag forces acting on a thrust vectoring engine in the longitudinal plane of the aircraft body coordinate system are schematically shown in Figure 4-7. The aerodynamic drag acting on an engine is represented with D_e.

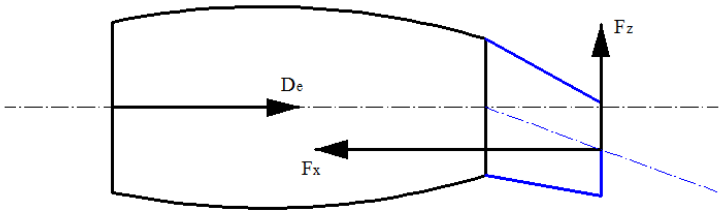

Figure 4-7 Thrust and drag forces acting on an engine (longitudinal plane)

Aerodynamic drag of an engine includes ram drag, inlet spillage drag, exhaust nozzle drag, as well as nacelle and pylon profile drag [42]. The engine drag component is calculated within Phalanx. The direction of engine drag can be approximated to be along with the engine axis. Then the engine net thrust can be calculated with the following equation and is used for solving the aircraft equations of motion:

$$\begin{cases} F_{n,x} = F_{g,x} - D_e \\ F_{n,y} = F_{g,y} \\ F_{n,z} = F_{g,z} \end{cases} \tag{4.22}$$

The moments produced by vectoring thrust w.r.t the CG of the aircraft are calculated with the engine gross thrust. As a matter of fact, engine drag component also produces a certain amount of moment w.r.t aircraft CG. However this part of moment is neglected in the current project since the moment arm of engine drag w.r.t aircraft CG is relatively small. With the location of an engine defined in section 3.2.2, which is represented by a vector $\mathbf{r}$ containing the distances from the engine nozzle to the aircraft CG in all three directions of aircraft reference frame, the moments produced by the vectoring nozzle can be calculated with the following equation:

$$\mathbf{M}_e = \mathbf{F}_g \times \mathbf{r} \tag{4.23}$$

where $\mathbf{F}_g$ is the gross thrust matrix and is defined as:

$$\mathbf{F}_g = \begin{bmatrix} 0 & F_{g,z} & -F_{g,y} \\ -F_{g,z} & 0 & F_{g,x} \\ F_{g,y} & -F_{g,x} & 0 \end{bmatrix} \tag{4.24}$$

and

$\mathbf{M}_e$: a column vector representing the components of moment produced by vectoring thrust

$\mathbf{r}$: a column vector representing the location of an engine w.r.t the aircraft CG

The gross thrust components in an aircraft body reference frame is shown in Figure 4-8. Note that in an aircraft body coordinate system, in which the positive X direction is pointing forward along the

aircraft symmetrical plane and the positive Z direction is pointing downward, an engine mounted aft the aircraft CG has a negative X coordinate, and an engine mounted higher than the aircraft CG has a negative Z coordinate.

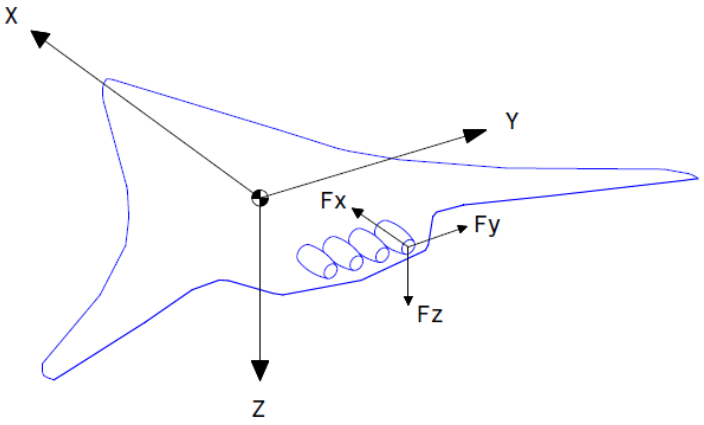

Figure 4-8 Thrust components in an aircraft body coordinate system

The moments produced by vectoring thrust components can then be expressed by:

$$\mathbf{M}_e = \begin{bmatrix} 0 & F_{g,z} & -F_{g,y} \\ -F_{g,z} & 0 & F_{g,x} \\ F_{g,y} & -F_{g,x} & 0 \end{bmatrix} \begin{Bmatrix} x \\ y \\ z \end{Bmatrix} = \begin{Bmatrix} F_{g,z} \cdot y - F_{g,y} \cdot z \\ -F_{g,z} \cdot x + F_{g,x} \cdot z \\ F_{g,y} \cdot x - F_{g,x} \cdot y \end{Bmatrix} \tag{4.25}$$

With equation (4.22) and equation (4.25) the forces and moments produced by vectoring nozzles can be calculated and substituted into the aircraft equations of motion system for flight mechanics analyses. From equation (4.25) it can be observed that each component of the moment produced by vectoring thrust is determined by two components of vectoring thrust. Only the thrust component in the same direction of the calculated moment axis is not contributing to this component of moment. Take the moment in Y direction for instance, an engine located aft, above and to the right of the aircraft CG has both negative X and Z coordinates, and positive Y coordinate. When the nozzle is deflected upward and inward for a certain amount of angle (within the deflection limits, for example maximum 20°), which produces forward, downward and outward thrust components as shown in Figure 4-8, the downward and positive vectoring thrust in Z direction with a negative X coordinate will produce nose up hence positive pitching moment. Simultaneously the forward and positive vectoring thrust in X direction with a negative Z coordinate will produce nose down hence negative pitching moment. This moment result is corresponding to the expression $M_y = -F_{g,z} \cdot x + F_{g,x} \cdot z$ in equation (4.25). This example explains that when nose up control moment is required for trimming a static stable aircraft, a high location of engine installation is not desired from the trimming point of view. However due to practical constraints the choice of high engine locations is sometimes inevitable.

4.2 Nozzle control modelling

When thrust vectoring is expected to be used as part of the control power of an aircraft, a proper control allocation of combined ACS and vectoring thrust controls needs to be developed. However this integrated control allocation is based on the premise that the effectiveness as well as the side effects and penalties of thrust vectoring control are well studied and understood. The objective of this thesis project is to examine the effects and effectiveness of thrust vectoring control under steady trimmed flight conditions of a BWB configuration. Therefore vectoring nozzles are controlled separately from ACS.

The algorithm of testing thrust vectoring controls proposed in this thesis project works like that there are two independent pilots in the cockpit of VELA2 controlling the respective ACS and vectoring nozzles. At a given flight Mach number and altitude, “Pilot TV” makes his decisions on how much thrust vectoring control he wants to use within the allowed range (from -20° to 20° in this project) and then pulls the “TV stick”. The separate control allocation of thrust vectoring calculates the deflection angle of every vectoring nozzle and the relative nozzle is deflected. Thrust forces and moments are produced by the vectoring nozzles and exerted on VELA2 aircraft. Then it is the responsibility of “Pilot ACS” to find the corresponding deflection angles of ACS by trials and errors to keep the aircraft in the desired steady trimmed flight condition (the trimming algorithm used in Phalanx). When the aircraft finally reaches the required trim condition, the consequent ACS deflections, nozzle deflections, aerodynamic forces and moments produced by each aircraft component, as well as the aircraft attitudes and engine fuel consumptions are tested and recorded.

It is already realized before carrying out the flight mechanics analysis, that the maximum moments produced by the ACS of VELA2 are much larger than the maximum moments that vectoring nozzles could produce, even though the engines have been moved to the trailing edge of the inner fuselage and the moment arms of vectoring nozzles have been maximized. Therefore thrust deflection is chosen to be the initial control of the trim analysis, and ACS deflection is the next control to trim the aircraft. This is because that if the dominating control power (the ACS of VELA2 in this project) is chosen to be the initial deflection and the control input is relatively large, then the next control power may not be able to trim the aircraft, and a final trimmed condition will never be accomplished, which means that the trim calculation will not converge. In short the selection of initial deflection power depends on the dominating control power of the analyzed aircraft configuration.

After a whole process of trim analysis from nozzle deflection to variables recording is finished, “Pilot TV” makes his next decision on the magnitude of thrust vectoring control and the whole trim routine is carried out again. The cooperation of ACS and TV is examined in a various range of nozzle deflections, flight conditions, CG and mass conditions. In this way the effects and effectiveness of thrust vectoring control are extensively studied and compared with the conventional control power. To implement the analysis process described above, the control of nozzle deflections by “Pilot TV” needs to be built up. The design of the control of nozzle deflections is discussed in this section.

4.2.1 Nozzle deflection control

Although the flight mechanics analyses carried out in this thesis project are within the 2-dimensional longitudinal plane, the control of vectoring nozzles is designed to have the capability of simulating nozzle deflections in both vertical and lateral directions. With multiple engines working together the vectoring thrust is capable of producing all the control moments in three directions, namely the pitching, rolling and yawing moments. Similar to the control module of ACS as defined in Phalanx, there are three control inputs for nozzle deflections, i.e. the longitudinal stick input, the lateral stick input and the pedal input, referring to the respective pitching control, rolling control and yawing control. With an arbitrary thrust vectoring control input, the distribution of nozzle deflections of all the engines is determined by a predefined control allocation matrix. Different from the control effectiveness matrix $\mathbf{B}$ introduced in section 5.4, which refers to the control derivatives of control effectors w.r.t the deflection of control effectors, the control allocation matrix directly connects the control inputs to the deflections of control effectors. The relation is expressed with the following equation:

$$\boldsymbol{\delta} = \mathbf{H} \cdot \mathbf{d} \tag{4.26}$$

where

$\boldsymbol{\delta}$: control effectors deflection vector, i.e. the nozzle/ACS deflections in this project

$\mathbf{H}$: control allocation matrix

$\mathbf{d}$: desired controlled variable vector, i.e. the pilot control inputs (a vector with three elements) in this project

To be more specific, the control allocation matrix of four axisymmetric thrust vectoring nozzles used in this project is of the following form:

$$\mathbf{H}_{TV} = \begin{bmatrix} \eta_{y,a}^{1} & \eta_{y,b}^{1} & \eta_{y,p}^{1} \\ \eta_{z,a}^{1} & \eta_{z,b}^{1} & \eta_{z,p}^{1} \\ \eta_{y,a}^{2} & \eta_{y,b}^{2} & \eta_{y,p}^{2} \\ \eta_{z,a}^{2} & \eta_{z,b}^{2} & \eta_{z,p}^{2} \\ \eta_{y,a}^{3} & \eta_{y,b}^{3} & \eta_{y,p}^{3} \\ \eta_{z,a}^{3} & \eta_{z,b}^{3} & \eta_{z,p}^{3} \\ \eta_{y,a}^{4} & \eta_{y,b}^{4} & \eta_{y,p}^{4} \\ \eta_{z,a}^{4} & \eta_{z,b}^{4} & \eta_{z,p}^{4} \end{bmatrix} \tag{4.27}$$

where the superscript refers to the nth nozzle, the first letter of the subscript refers to the direction of nozzle direction, and the second letter of the subscript refers to the pilot control input (a refers to lateral stick control input, b refers to longitudinal stick control input and p refers to pedal control input). The difference between the control allocation matrix of a vectoring nozzle and the control allocation matrix of an ACS is that there are two rows for the control of one nozzle, while there is only one row in the corresponding control allocation matrix for controlling one ACS. The reason for this difference is that an ACS normally has deflections in one direction w.r.t its hinge line, namely up and

down or left and right deflections, while the axisymmetric thrust vectoring nozzle in this thesis project is capable to deflect in both the lateral and vertical directions simultaneously. Therefore two rows in a control allocation matrix need to be used to control the nozzle deflections separately in both directions. Not all vectoring nozzles are designed to deflect in both lateral and vertical directions. One typical example is the 2D-CD vectoring nozzle used on the Pratt & Whitney F119 afterburning turbofan engine designed for the Lockheed Martin F-22 Raptor. Even though yawing controllability was tested in the early developing phase of F119 turbofan engine, this capability was abandoned later and only pitching controllability was kept for the thrust vectoring control. In the case of the F119 turbofan engine the control allocation matrix of vectoring nozzles would be similar to that of the ACS. Figure 4-9 shows a combined deflection of thrust line in both y and z direction of the aircraft body reference frame. It is the separate controls and hence deflections in the two mentioned directions which results in the final position of the thrust line.

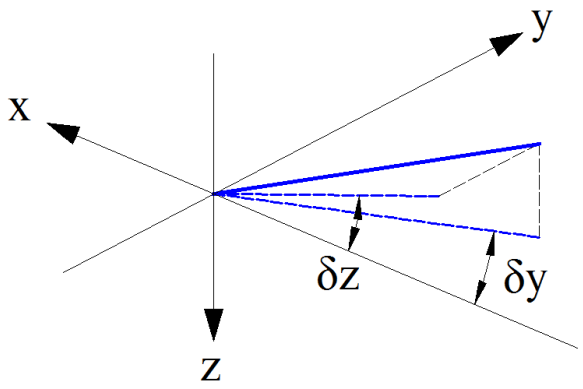

Figure 4-9 Combined deflections in both y and z directions

The nozzle control equation (4.26) can then be written in a more detailed form:

$$\begin{Bmatrix} \delta_y^1 \\ \delta_z^1 \\ \delta_y^2 \\ \delta_z^2 \\ \delta_y^3 \\ \delta_z^3 \\ \delta_y^4 \\ \delta_z^4 \end{Bmatrix} = \begin{bmatrix} \eta_{y,a}^1 & \eta_{y,b}^1 & \eta_{y,p}^1 \\ \eta_{z,a}^1 & \eta_{z,b}^1 & \eta_{z,p}^1 \\ \eta_{y,a}^2 & \eta_{y,b}^2 & \eta_{y,p}^2 \\ \eta_{z,a}^2 & \eta_{z,b}^2 & \eta_{z,p}^2 \\ \eta_{y,a}^3 & \eta_{y,b}^3 & \eta_{y,p}^3 \\ \eta_{z,a}^3 & \eta_{z,b}^3 & \eta_{z,p}^3 \\ \eta_{y,a}^4 & \eta_{y,b}^4 & \eta_{y,p}^4 \\ \eta_{z,a}^4 & \eta_{z,b}^4 & \eta_{z,p}^4 \end{bmatrix} \cdot \begin{Bmatrix} y_a \\ y_b \\ y_p \end{Bmatrix} \tag{4.28}$$

in which

δ_y^i, δ_z^i: nozzle deflection angle of the ith engine in y/z direction

y_a, y_b, y_p: control inputs of "pilot TV" in respective lateral, longitudinal and directional directions

With a predefined control allocation matrix and an arbitrary control input (within the given control range) the deflection of every nozzle in both lateral and vertical directions can be calculated directly with equation (4.28).

4.2.2 Check for saturation

The separate controls of a vectoring nozzle in lateral and vertical directions may lead to deflection saturations for an axisymmetric vectoring nozzle. From a mechanics point of view, an axisymmetric vectoring nozzle has the same maximum deflection capability in all combinations of lateral and vertical directions. In other words, the maximum thrust deflections in all possible directions should form a circle as shown in Figure 4-10. Limitations for pilot control inputs of nozzle deflections are predefined separately for each of the lateral, longitudinal and directional control input. However when a pilot control input of nozzle deflection reaches the limits of both lateral and longitudinal direction simultaneously, the control command shown with red line in Figure 4-10 will exceed the capability of nozzle deflection shown with blue line. The thrust vectoring control module needs to check the saturation of nozzle deflections and ensure that the final deflection commands after checking are within the capability range of nozzle deflections.

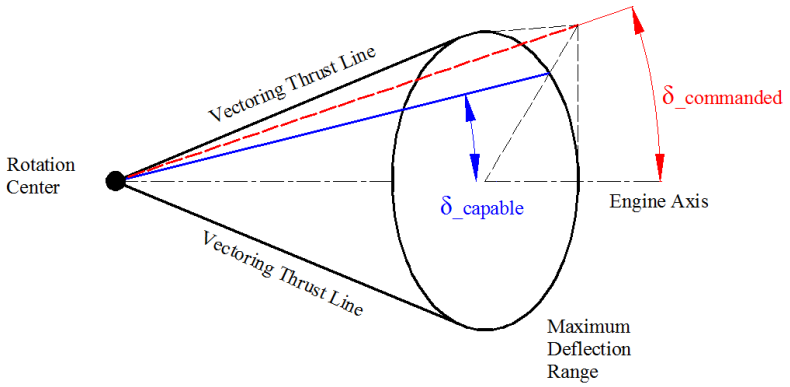

Figure 4-10 Check for nozzle deflection saturation

In order to perform the saturation checking, the commanded nozzle deflections δ_y and δ_z in the body coordinate system, which are calculated from the pilot control inputs and the control allocation matrix, are transformed in to a combination of so called absolute deflection angle δ_n and deflection azimuth θ_n defined in this project. The absolute deflection angle is defined to be the angle between the deflected thrust line and the engine axis, and the deflection azimuth is defined to be the angle between the thrust deflection direction and the Y axis of the body reference frame, varying from 0 to 2π in radian. The definition is schematically shown in Figure 4-11.

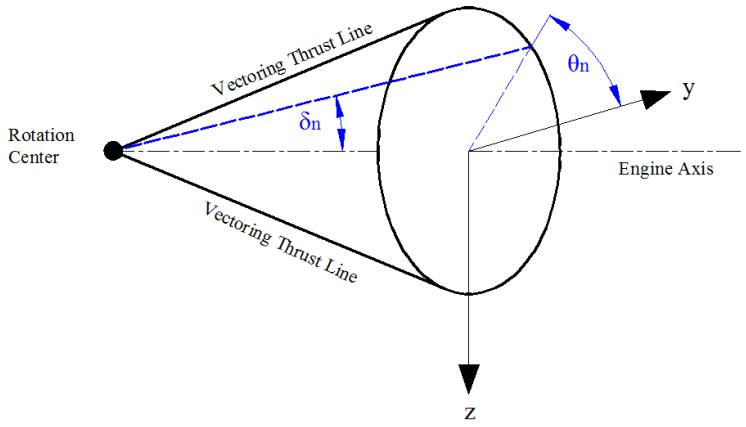

Figure 4-11 Definition of absolute deflection and deflection azimuth

The difference between the definitions of (δ_y, δ_z) and (δ_n, θ_n) can be easily distinguished from Figure 4-9 and Figure 4-11. The formulae of calculating (δ_n, θ_n) from (δ_y, δ_z) are:

$$\delta_n = \arccos\left(\cos\delta_y \cdot \cos\delta_z \cdot S\right) \tag{4.29}$$

and

$$\theta_n = \begin{cases} \arctan\left(\tan\delta_z / \tan\delta_y\right) & \delta_y > 0, \delta_z \geq 0 \\ 2\pi + \arctan\left(\tan\delta_z / \tan\delta_y\right) & \delta_y > 0, \delta_z < 0 \\ \pi/2 & \delta_y = 0, \delta_z \geq 0 \\ \pi 3/2 & \delta_y = 0, \delta_z < 0 \\ \pi + \arctan\left(\tan\delta_z / \tan\delta_y\right) & \delta_y < 0, \delta_z \geq 0 \\ \pi + \arctan\left(\tan\delta_z / \tan\delta_y\right) & \delta_y < 0, \delta_z < 0 \end{cases} \tag{4.30}$$

Due to the characteristics of inverse tangent function, different conditions need to be considered for different combinations of δ_y and δ_z since the range of deflection azimuth is defined to be from 0 to 2π in radian.

After the transformation from (δ_y, δ_z) to (δ_n, θ_n), the commanded absolute deflection angle of a vectoring nozzle will be checked for its saturation condition. If the commanded δ_n exceeds the maximum allowed deflection it will be overwritten by the deflection limit and a corrected absolute deflection angle will be used in the following control process. Unlike an axisymmetric vectoring nozzle, a 2D-CD vectoring nozzle doesn't need such a transforming process since its commanded deflection angle and absolute deflection angle are of the same dimension, similar to that of ACS when the deflection of control effectors are only in one direction.

It needs to be noticed that the transformation is only used for saturation check, and the nozzle control effectors are still controlled by control inputs in the form of (δ_y, δ_z), but with corrected values when

saturations exist. Therefore after checking the saturation of nozzle deflections, the absolute deflection angle and azimuth angle $\left(\delta_n, \theta_n\right)$ need to be transformed back to $\left(\delta_y, \delta_z\right)$ for nozzle deflection controls. The equations of transforming backwards are given by:

$$\begin{cases} \delta_y = \arctan\left(\tan\delta_n \cdot \cos\theta_n\right) \\ \delta_z = \arctan\left(\tan\delta_n \cdot \sin\theta_n\right) \end{cases} \tag{4.31}$$

5 Preparing inputs for Phalanx

Carrying out flight mechanics analysis with Phalanx is based on solving the equations of motion of the analyzed aircraft. A Jacobian method [29] is used in Phalanx to calculate the trim condition of an aircraft. To carry out the flight mechanics analysis including trim analysis, all the forces and moments acting on the analyzed aircraft as well as the mass and inertia of the aircraft need to be prepared for solving the equations of motion. As has been discussed in section 3.1, different tools are utilized to calculate the required information. The theory basis of the utilized tools are already introduced in section 3.1. The inputs of Phalanx trim calculation, i.e. the outputs of the supporting tools as well as the calculations of the respective forces and moments of every aircraft component based on the outputs of utilized tools are discussed in this section.

5.1 Aerodynamic performance database

The aerodynamic performance database of the modified VELA2 configuration is estimated with Tornado and VRaero as introduced in section 3.1.2. The geometrical model and flight conditions of the analyzed aircraft are the two main inputs of aerodynamic tools including Tornado and VRaero. The aerodynamic estimation results are wrapped with the format required by Phalanx, i.e. lookup tables. For a particular analyzed flight condition given by the aircraft angle of attack α, sideslip angle β, airspeed V and flight altitude, Phalanx determines the corresponding aerodynamic coefficients and calculate the respective aerodynamic forces and moments. Therefore the aerodynamic database that Tornado produces needs to be corresponding to the requirements of Phalanx.

To estimate the aerodynamic performance of an aircraft with Tornado two categories of inputs are required, namely the geometry model of the aircraft and the flight conditions to be analysed. For thrust vectoring control analysis with VELA2 configuration in this thesis project, a geometry model of the VELA2 configuration is provided by the Department of Integrated Aircraft Design of DLR. Only particular flight conditions need to be specified according to the requirements of the project. For this thesis project, it is interesting to know the effectiveness of thrust vectoring control in a wide range of flight conditions which represent a typical flight envelop of a transport aircraft. Although Tornado is more accurate on low speed flight conditions when compressibility effect of flow is not strong, high speed flight conditions are still analysed with Tornado results for coarse investigations on the qualitative behaviors of thrust vectoring control.

Since the analysis of thrust vectoring control conducted in this project is focusing on steady trimmed flights in longitudinal direction, therefore the sideslip angle and the angular rates for aerodynamic database construction are set to zero. Only the angles of attack and airspeeds are varied for various flight conditions. Sixteen angles of attack varying from -5° to 12.5° and thirteen airspeeds varying from about 65 m/s to about 270 m/s are set as the flight conditions to be calculated with Tornado.

The set of airspeeds selected for the aerodynamic performance database of this project is based on combinations of a series of flight Mach numbers and Reynolds numbers aiming to cover a typical flight envelop of a transport aircraft. The combinations of selected Mach numbers and Reynolds numbers for aerodynamic performance analysis and the corresponding true airspeeds (TAS) are shown in Table

5-1. The Tornado aerodynamic results corresponding to the relevant TAS shown in bold and italic font in Table 5-1 are chosen to build the aerodynamic database of the VELA2 configuration. Interpolations or extrapolations of the aerodynamic performance are carried out by Phalanx when flight conditions of the flight mechanics simulations are amongst or out of range of the flight conditions of the aerodynamic database.

Table 5-1 TAS for every combination of Mach number and Reynolds number

TAS [m/s]		Reynolds number						
		1.20E+08	1.60E+08	2.00E+08	2.40E+08	2.80E+08	3.20E+08	3.60E+08
Mach number	0.2	***65.35***	67.72					
	0.3	93.94	97.35	99.66	***101.59***			
	0.4	***121.52***	125.93	128.92	***131.41***	133.56	135.45	
	0.5		***153.76***	157.41	160.46	163.08	***165.39***	167.45
	0.6		***181.01***	185.31	***188.89***	191.98	194.69	***197.12***
	0.7			212.72	216.83	***220.38***	223.49	226.28
	0.8			***239.72***	244.36	248.35	251.86	255.00
	0.85				***257.98***	262.19	265.90	***269.21***

The corresponding flight altitudes for every combination of Mach number and Reynolds number is shown in Table 5-2.

Table 5-2 Flight altitude for every combination of Mach number and Reynolds number

Altitude [m]		Reynolds number						
		1.20E+08	1.60E+08	2.00E+08	2.40E+08	2.80E+08	3.20E+08	3.60E+08
Mach number	0.2	***3011***	435					
	0.3	6388	4022	2086	***435***			
	0.4	***8615***	6388	4565	***3011***	1650	435	
	0.5		***8127***	6388	4905	3606	***2447***	1396
	0.6		***9489***	7815	***6388***	5138	4022	***3011***
	0.7			8980	7598	***6388***	5308	4329
	0.8			***9958***	8615	7438	6388	5437
	0.85				***9067***	7906	6869	***5929***

Different airspeed and flight altitude conditions have influences on the results of aerodynamic estimations when the aerodynamic tool takes into account the compressibility and viscosity effects of airflow. As a matter of fact for Tornado used in this project, based on the VLM algorithm its results do not depend on the flight speed and altitude. The VELA2 aerodynamic performance under two of the flight conditions analysed by Tornado are schematically shown in the following figures. Except for the

friction drag estimated with a semi-empirical method as introduced in section 3.1.2.2 which is dependent on the flight Mach number, the aerodynamic results of different flight conditions estimated with Tornado are identical as can be seen from Figure 5-1 to Figure 5-3.

Figure 5-1 shows the lift coefficients of VELA2 estimated with Tornado w.r.t various angles of attack under two of the analysed flight conditions. It can be observed that without considering the compressibility and viscosity of airflow, the lift coefficients of VELA2 analysed with Tornado under different flight conditions are identical and are linear w.r.t the changing of angle of attack. The simplifications on airflow compressibility and viscosity by VLM algorithm for aerodynamic performance estimations are more acceptable for small angles of attack under low speed flight conditions when the effects of flow separation and shock wave are not obvious.

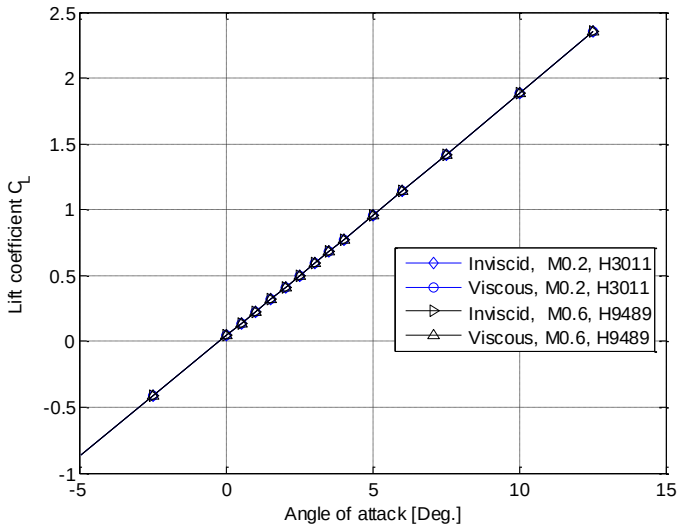

Figure 5-1 Lift coefficients of VELA2 analysed with Tornado

The drag coefficients (excluding wave drag) of VELA2 under two different flight conditions are shown in Figure 5-2. Similar to the characteristics of lift coefficients, the induced drag calculated by Tornado with different flight conditions are identical. The calculation of skin friction drag coefficient in this thesis project is accomplished with the in-house developed tool VRaero which is dependent on the Reynolds number hence the flight condition as indicated in equation (3.26) and (3.27). Therefore slight differences can be observed from the friction/form drags as well as the final total drags of different flight conditions from Figure 5-2.

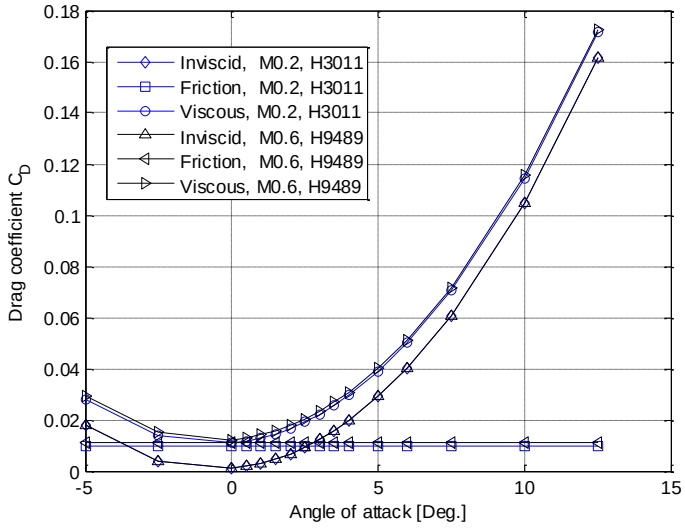

Figure 5-2 Drag coefficients of VELA2 analysed with Tornado and VRaero

The pitching moment coefficients of VELA2 under the same two flight conditions discussed above are shown in Figure 5-3. Negative slopes of the pitching moment coefficient lines indicate that VELA2 is designed to be statically stable. The pitching moment coefficient reaches zero at around 2° of angle of attack. This characteristic makes it possible for VELA2 to fly with minimum induced drag under cruise flight conditions with all trailing edge control surfaces faired.

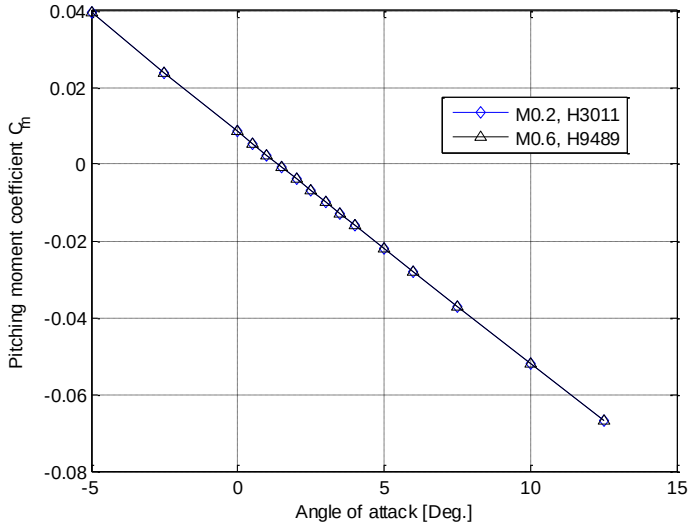

Figure 5-3 Pitching moment coefficients of VELA2 analysed with Tornado

The control derivatives of pitching moment coefficient of VELA2 ACS ($\dot{C}_{m,ACS}$) are shown in Figure 5-5. The control derivatives of the two ailerons, among all the trailing edge control surfaces as repeated in Figure 5-4, are not shown here as this control surface is not used for pitching control of VELA2. All the pitching control surfaces produce negative pitching moments with positive deflections (trailing edge down) but with different magnitudes. The differences of pitching control efficiency among different

ACS can be explained in a similar way as the tail volume coefficient. The volume coefficient of an ACS $\bar{V}_{ACS}$ can be calculated with the same equation as that of a horizontal tail:

$$\bar{V}_{ACS} = \frac{S_{ACS} \cdot l_{ACS}}{S \cdot \bar{c}_{mac}} \tag{5.1}$$

in which

S_{ACS} : planform area of an ACS

l_{ACS} : moment arm of an ACS

S : planform area of the aircraft

$\bar{c}_{mac}$: mean aerodynamic chord of the aircraft

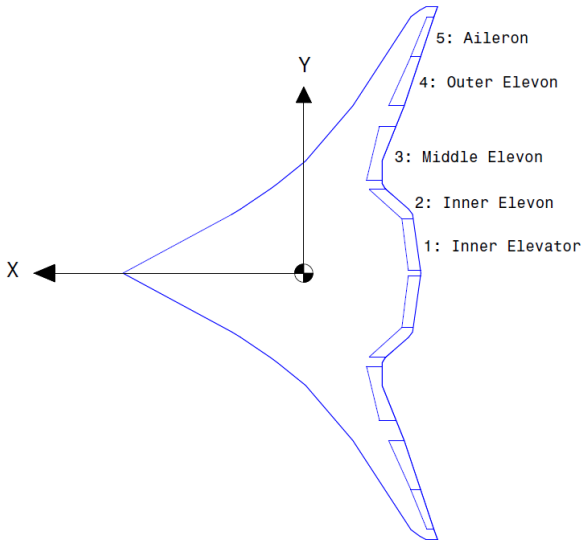

Figure 5-4 Control surface distribution at the wing trailing edge of VELA2

The volume coefficients of the four pitching control surfaces of VELA2 are listed in Table 5-3.

Table 5-3 Volume coefficients of four pitching ACS of VELA2

ACS	Planform area (m^2)	Moment arm (m)	Volume coefficient
Inner elevator	21.36	19.53	417.16
Inner elevon	17.11	16.38	280.26
Middle elevon	25.62	14.03	359.45
Outer elevon	33.28	17.52	583.07

From both Table 5-3 and Figure 5-5 it can be noticed that the outer elevon is most effective in pitching control as is has the largest planform area and has a relative long moment arm. The inner elevon has the least planform area and a relative short moment arm, and is therefore the least effective ACS for pitching control.

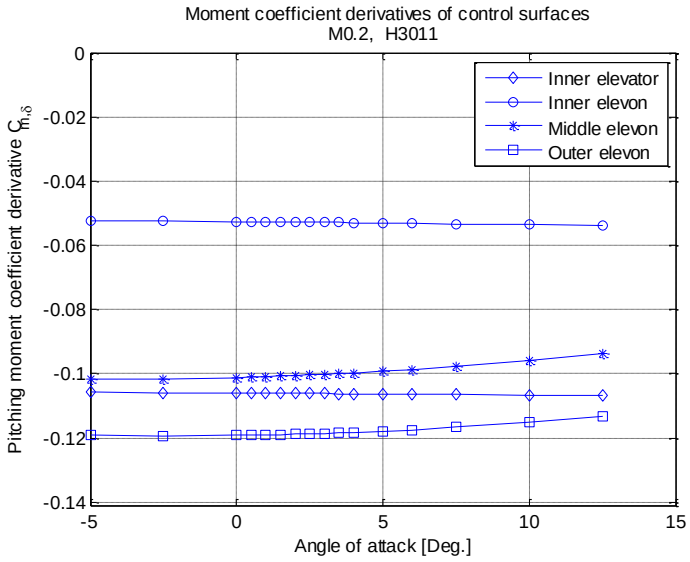

Figure 5-5 Derivatives of pitching moment coefficient of VELA2 ACS

5.2 Engine performance map

According to the infrastructure of Phalanx the forces and moments produced by engines are calculated from a prepared engine performance map which is similar to the aerodynamic database. An engine performance map of the scaled JT9D turbofan engine is used directly from the European MOB project. It is formatted as lookup tables which can be directly used by Phalanx. The engine performance map contains engine gross thrust, net thrust, fuel consumption rate etc. under a set of engine working conditions. A particular engine working condition consists of the ambient altitude, Mach number of the coming flow (i.e. the aircraft flight Mach number), and the throttle setting (i.e. PLA of the engine). The engine working conditions prepared for the engine performance map are listed in Table 5-4. The value of PLA in the engine performance map is a ratio of the current PLA to the maximum PLA of the design condition of the scaled JT9D.

Table 5-4 Engine working conditions of the engine performance map

Parameter	Value												
Altitude (km)	0	1	2	3	4	5	6	7	8	9	10	11	12
Mach number	0	0.1	0.2	0.3	0.4	0.5	0.6	0.7	0.8	0.9			
PLA	0.8	0.85	0.9	0.95	1.0	1.05	1.1	1.15					

For every combination of the ambient altitude, Mach number and PLA as listed above a corresponding engine performance value can be picked up directly from the look-up tables of the engine performance map. For engine working conditions amongst the prepared working conditions or outside the range of the prepared performance map, interpolations or extrapolations will be carried out by Phalanx Simulink modules. The gross thrust of the scaled JT9D under four different working conditions from the engine performance map are shown in Figure 5-6.

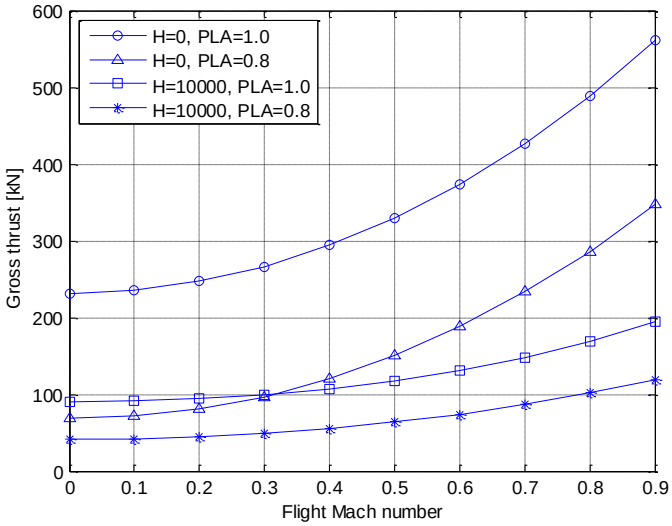

Figure 5-6 Gross thrust of the scaled JT9D for four working conditions

PLA determines the fuel ejection rate in engine combustor hence the energy production rate of the engine, while ambient altitude determines the air density hence the mass flow rate of the engine. Therefore it can be seen from Figure 5-6 that the engine working condition with ground altitude and maximum design PLA has the most gross thrust, while the engine working condition with cruise altitude and 80% of the maximum design PLA has the least gross thrust.

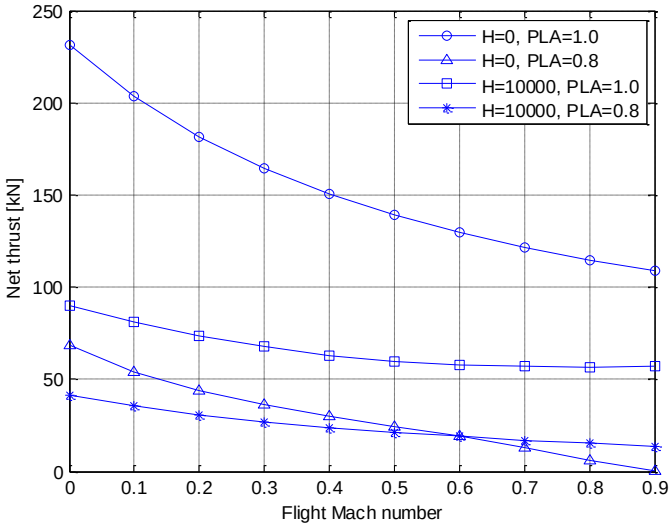

Figure 5-7 Net thrust of the scaled JT9D for four working conditions

The engine net thrust is engine gross thrust subtracted by engine drag as already discussed in section 4.1.3. The main difference between the characteristics of engine gross thrust and net thrust under various engine working conditions is their variation tendency w.r.t the change of flight Mach number. With the increase of flight Mach number the engine gross thrust increases accordingly as can be observed from Figure 5-6 since the engine inlet mass flow has an increase w.r.t the increase of flight Mach number. However the engine ram drag which contributes most part of the engine drag is directly related to aircraft flight speed and engine inlet mass flow, and has a rapider increase than engine gross

thrust w.r.t the increase of flight Mach number. The resulted engine net thrust is thus decreasing w.r.t the increase of aircraft flight Mach number under a given flight altitude and throttle setting. The difference between the characteristics of engine gross thrust and net thrust has a direct influence on the effects of thrust vectoring control for trimming an aircraft in a way that: with the increase of aircraft flight speed, the thrust force which is corresponding to engine net thrust has a consequent decrease, while the control moment produce by engine thrust which is corresponding to engine gross thrust will have a consequent increase.

The fuel consumption rate of the scaled JT9D with the same working conditions as discussed above are shown in Figure 5-8. It should be aware that the fuel consumption rates of the engine performance map are the total fuel mass consumed per second but not the thrust specific fuel consumption. By comparing Figure 5-6 and Figure 5-8 it can be observed that the influences from PLA on engine fuel consumption rate is stronger than the influences on engine gross thrust.

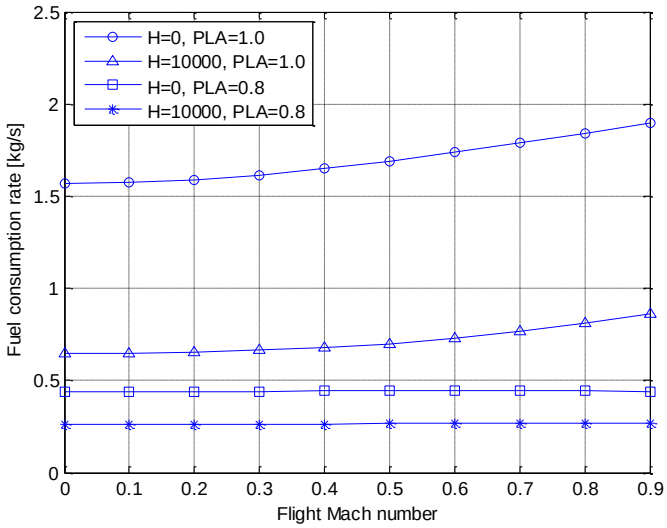

Figure 5-8 Fuel consumption rate of the scaled JT9D for two engine working conditions

With a given engine working condition, which is relative to the requirements of the specified flight condition of an analyzed aircraft, the fuel consumption rate and engine gross thrust are calculated by Phalanx through look-up tables. The fuel consumption rate is recorded for further analysis, while the engine gross thrust is used to calculate the forces and moments produced by all the utilized engines with the nozzle deflection angles and calculation algorithms explained in section 4.1.3.

5.3 Aircraft mass and inertia

To solve the equations of motion of an aircraft the information about aircraft mass and inertia needs to be prepared as well. The mass and inertia of VELA2 used in this thesis project is calculated with an in-house developed mass estimation tool, namely the BWBmass specialized for BWB configurations. The structural mass and inertia of the aircraft is calculated based on semi-geometrical methods. The masses of aircraft systems, payload and mission fuel are estimated based on statistical data of existing conventional transport aircrafts and the design requirements of VELA2. Aircraft systems, payload and

fuel are treated as point mass by BWBmass therefore inertia of these components are ignored. The neglect of inertia of aircraft components has influences on flight dynamics performance of the analyzed aircraft. However for the steady trimmed flight simulations conducted in this thesis project, the simplification of inertia estimation is acceptable. The masses of VELA2 components estimated with BWBmass are listed in Table 5-5.

Table 5-5 Mass breakdown of VELA2 estimated with BWBmass

Category	Aircraft component	Mass (kg)
OEM	Structure	244853
	Power units	18880
	Systems	25524
	Furnishing	45284
	Operator items	40172
Payload	Passenger	86664
	Cargo	10730
Fuel		144591
MTOM		**616698**

The inertia of VELA2 estimated with BWBmass, which only contains the inertia of the aircraft structure, is listed in Table 5-6.

Table 5-6 Moment of inertia of the airframe of VELA2

Component	Value (kg·m^2)
I_{xx}	80685507.53
I_{yy}	559021969.15
I_{zz}	639528798.65

As explained in precedent sections, thrust vectoring control analysis of this thesis project is carried out with various aircraft mass and CG combinations. Three aircraft CG locations with OEM, one aircraft CG location with half of the payload and fuel mass, and three aircraft CG locations with MTOM are analyzed through this project. With OEM conditions, the aircraft CG locations are varied by changing the relative aircraft CG locations to the origin of the forces and moments coordinate system in Phalanx. With MTOM conditions, the combination of payload and fuel mass is considered as a movable point mass. By changing the relative locations of the point mass to the location of aircraft OEM CG, the CG locations of the fully loaded aircraft are varied.

In total there are seven combinations of masses and CG locations analyzed in this project as listed in Table 5-7. The CG locations indicated in the table are the distances of aircraft CG from the nose of the center fuselage. As described in section 1.3, the variation of CG is based on a desired magnitude of CG range from statistic data of transport aircrafts. Eighteen percent of the MAC of VELA2 (MAC of VELA2: 36 m) is selected as the CG range of this project, which represents the distance between the most forward and most aft CG. The aerodynamic center of VELA2 is located at 35.43 m aft the nose of center

fuselage in the X direction of the body reference frame. Static margin of -9% MAC (-3.24 m) and +9% MAC (3.24 m) are selected evenly from the desired CG range for the distribution of CG locations w.r.t the aircraft aerodynamic center. Note that in Table 5-7 the middle CG locations refer to the OEM CG and has a positive static margin of 1.2 m.

Table 5-7 Mass and CG variations

Mass condition	Aircraft mass (kg)	CG location		
		Most forward	Middle	Most aft
OEM	374714	32.19	34.23	38.67
Half payload and fuel	495707	----	34.23	----
MTOM	616698	32.19	34.23	38.67

5.4 Control allocation

It is already mentioned in precedent sections that the calculation of the forces and moments of ACS and vectoring nozzles are dependent on the respective deflection angles of ACS and nozzles such as the deflection angles of ACS in equation (3.4) and the deflection angles of nozzles in equation (4.21). Therefore before the calculation of control forces and moments produced by either ACS or vectoring nozzles, the deflection angles of the control effectors need to be determined. For aircraft configurations with redundant control effectors, a proper distribution of control deflections needs to be worked out. The distribution of deflections of control effectors is called control allocation.

Control allocation is a general term that describes a process used to determine how to employ a number of control effectors to achieve a desired reaction from a system. When a system is equipped with more control effectors than controlled variables, the system may be over-actuated. The control allocation problem aims to achieve some desired objectives by allocating, blending or mixing these redundant control effectors. As the number of control effectors increases, the determination of specific control allocation schemes becomes more difficult and the requirement for systematic control allocation algorithms increases [43].

However it is not the aim of this project to employ a comprehensive control allocation analysis on the integration of conventional ACS and vectoring nozzles. The objective of this project is to investigate the effects and effectiveness of thrust vectoring control on longitudinal steady trimmed flight conditions compared to conventional ACS control. Separate controls are implemented on ACS and vectoring nozzles to extensively compare the effectiveness between the two control powers. For the independent controls of ACS and vectoring nozzles, separate control allocations are required for the respective control distributions of ACS and vectoring nozzles. In this project the two control allocations are based on a brief investigation on various control allocation algorithms especially the preferred control allocation algorithms for a BWB configuration.

5.4.1 Brief introduction to control allocation

For a conventional aircraft, there are mainly 5 control effectors (two elevators, two ailerons, and one rudder) and 3 controlled variables (pitching, rolling, and yawing). With cables and pulleys connecting the pilot stick and rudder pedals to the control surfaces the movement of two elevators are constrained by ganging to move symmetrically while the movement of two ailerons are constrained to move differentially by ganging. The number of control effectors is reduced from 5 to 3 and is equal to the number of controlled variables. Therefore for a conventional control system the allocation of control tasks among the three effective control surfaces is straightforward. However for a modern aircraft design there may be much more control effectors than controlled variables for control redundancy (for an aircraft the controlled variables are the three rotation moments). Some of these control effectors may be difficult to determine a suitable ganging scheme like conventional elevators or ailerons. In these cases, a control allocation algorithm is necessary to systematically determine the control settings to produce a desired response.

Generally, a constrained control allocation problem is to find the control effector deflection vector $\boldsymbol{\delta} \in \mathbb{R}^n$, such that

$$\mathbf{f}(\boldsymbol{\delta}) = \mathbf{d}_{des} \tag{5.2}$$

subject to the constraints of control deflections:

$$\begin{aligned} \boldsymbol{\delta}_{\min} \le \boldsymbol{\delta} \le \boldsymbol{\delta}_{\max} \\ \left|\dot{\boldsymbol{\delta}}\right| \le \dot{\boldsymbol{\delta}}_{\max} \end{aligned} \tag{5.3}$$

where $\mathbf{d}_{des} \in \mathbb{R}^m$ is a vector of desired controlled variables (for example the desired control moments, or the pilot control inputs which is directly related to the desired control moments), $\mathbf{f}(\boldsymbol{\delta}) \in \mathbb{R}^m$ is a vector of linear and/or nonlinear functions of the control effectors, and

$\boldsymbol{\delta}_{\min}$, $\boldsymbol{\delta}_{\max}$: lower and upper limit of control deflections

$\dot{\boldsymbol{\delta}}$, $\dot{\boldsymbol{\delta}}_{\max}$: control deflection rate and its corresponding upper limit, the lower limit is naturally zero

When the limitations of control deflections depicted in equation (5.3) are neglected, the constrained control allocation problem becomes an unconstrained control allocation problem.

There are several control allocation algorithms with different mathematical approaches to find a proper solution for the control effectors by solving equation (5.2). Due to the linearity of sub-equations in equation (5.2), control allocation can be divided into linear control allocation problems with all linear sub-equations to be solved, and nonlinear control allocation problems when nonlinear equations are included in $\mathbf{f}(\boldsymbol{\delta})$. From another point of view, whether the rate and position limits of the effectors are included in the control allocation problems, control allocation algorithms can be divided into unconstrained control allocation and constrained control allocation. Main algorithms for solving the unconstrained control allocation problems include matrix inverse, explicit ganging, pseudo inverse, pseudo control et al. Algorithms for solving constrained control allocation problems include redistributed pseudo inverse, daisy chain, direct allocation, linear programming, quadratic

programming, as well as affine control allocation and nonlinear programming specialized for nonlinear control allocation problems [43] [44].

The simplest cases for control allocation problems are those when the rate and position limits are not taken into account and all the sub-equations in equation (5.2) are linear. The unconstrained linear control allocation problems can be expressed in the form of:

$$\mathbf{B}\boldsymbol{\delta} = \mathbf{d}_{des} \tag{5.4}$$

where $\mathbf{B} \in \mathbb{R}^{m \times n}$ is the control effectiveness matrix. For aircraft inner-loop control laws, the control effectiveness matrix is typically of the form:

$$\mathbf{B} = \begin{bmatrix} \dfrac{\partial L}{\partial \delta_1} & \dfrac{\partial L}{\partial \delta_2} & \cdots & \dfrac{\partial L}{\partial \delta_n} \\ \dfrac{\partial M}{\partial \delta_1} & \dfrac{\partial M}{\partial \delta_2} & \cdots & \dfrac{\partial M}{\partial \delta_n} \\ \dfrac{\partial N}{\partial \delta_1} & \dfrac{\partial N}{\partial \delta_2} & \cdots & \dfrac{\partial N}{\partial \delta_n} \end{bmatrix} \tag{5.5}$$

In equation (5.5) L, M and N represent the respective rolling, pitching and yawing moment. Control allocation algorithms aim to search for a proper solution for equation (5.4) based on the desired controlled variables such as the rotation speeds of the aircraft, and the control effectiveness matrix.

When the control effectiveness matrix $\mathbf{B}$ is square and invertible, which means that the number of control effectors is equal to the number of controlled variables, the control allocation solution is a standard inverse:

$$\boldsymbol{\delta} = \mathbf{B}^{-1}\mathbf{d}_{des} \tag{5.6}$$

The inverse of the control effectiveness matrix $\mathbf{B}^{-1}$ is equally functioned as the control allocation matrix $\mathbf{H}$ introduced in equation (4.26) for nozzle control allocation. The relation could be expressed as:

$$\mathbf{H} = \mathbf{B}^{-1} \tag{5.7}$$

For over-actuated system there are more control effectors than the controlled variables. The control effectiveness matrix $\mathbf{B}$ is not square and hence has no inverse. There are several techniques to reduce the control space dimension, and to transform a non-square matrix into a square one. Ganging is one of those techniques. By ganging, several physical control effectors are connected to one effective control effector. For instance, the cable and pulley connected control system of a conventional aircraft transforms the two differential aileron effectors into a single lateral stick control input, and the two symmetrical elevator effectors into a single longitudinal stick control input. The single rudder effector is connected to a single rudder pedal control. By this ganging method the five physical control effectors are transformed into three effective control effectors and result in a square control effectiveness matrix. The goal of explicit ganging method is to find a ganging matrix such that

$$\boldsymbol{\delta} = \mathbf{G}\boldsymbol{\delta}_{pseudo} \tag{5.8}$$

where

$\mathbf{G}$: the explicit ganging matrix

$\boldsymbol{\delta}_{pseudo}$: the control effector deflection vector after ganging

An explicit ganging strategy is designed offline when it is obvious how to combine redundant control effectors. Then equation (5.4) becomes

$$\mathbf{BG}\boldsymbol{\delta}_{pseudo} = \mathbf{d}_{des} \tag{5.9}$$

With an explicit ganging matrix the control effectiveness matrix becomes a square matrix and the solution to equation (5.9) is by directly multiplying an inverse of the new control effectiveness matrix on each side of equal sign. Then equation (5.9) can be written as

$$\boldsymbol{\delta}_{pseudo} = \left(\mathbf{BG}\right)^{-1}\mathbf{d}_{des} = \mathbf{H}\mathbf{d}_{des} \tag{5.10}$$

where $\mathbf{H} = \left(\mathbf{BG}\right)^{-1}$ is the control allocation matrix for ganged control effectors.

Due to the simplicity of explicit ganging algorithm and the relative simple requirements on control allocation of this thesis project, explicit ganging algorithm is used for the control allocation of the ACS and vectoring nozzles of the modified VELA2 configuration in this project. The comparison results of different control allocations on a BWB configuration discussed in the subsequent section are used as the basis and guidance of setting up the control allocation matrix $\mathbf{H}$ of equation (5.10). The mathematic theorems of other control allocation algorithms are not discussed in this report.

5.4.2 BWB Control allocation investigations

The control allocation of a BWB is complicated because of the high redundancy and coupling of control surfaces, the lack of long coupled pitch effectors, and the lack of dedicated trim devices of this novel configuration. A poorly designed control allocator will hamper the performance and capability of the control system to stabilize, control and trim the aircraft. In contrast, an efficient control allocator may improve the overall configuration and minimize control surfaces sizes, deflection limits, deflection rates and bandwidth requirements. For example, a poorly control allocator may utilize only part of the available control surfaces resulting in higher deflection angles. The higher deflections lead to larger deflection rates and hence more secondary power requirements from engines.

An investigation on the consequences of control allocation algorithm selection for early design stages (conceptual/preliminary) of a blended wing body was conducted by Waters and Voskuijl from Delft University of Technology [45]. With given control requirements including pure rolling moments, pure pitching moments and combined rolling and pitching moments, the control surface deflections of a BWB wind tunnel model were calculated with four different control allocation algorithms: an l_1-norm Linear Programming method (LP-1), a Weighted Pseudo-Inverse (WPI) method, a Fixed-Point Iteration (FXP) method, and a Direct Allocation Linear Programming (LP-DA) method. Different algorithms produced substantially different control outputs for the three given required control moments (small, medium and large command magnitude), as shown in Figure 5-9.

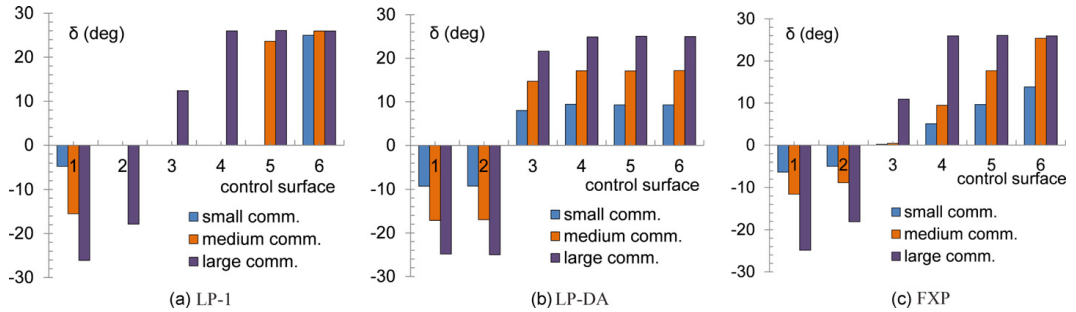

Figure 5-9 Control outputs of three different control allocation algorithms [45]

Wind tunnel test was carried out with the control surfaces of the BWB wind tunnel model configured in the order calculated with the chosen control allocation algorithms, and the tested moments produced by the calculated control deflections were compared with those expected from control allocations. Results showed that the actual tested control performance dropped with increasing control commands due to the actual non-linearity of control moments which was not considered in the linear control allocation algorithms. LP-1 algorithm had the largest average performance loss, while LP-DA had the best average performance among the four tested control allocation algorithms. One reason of the different performance among the four algorithms is that LP-1 control allocation algorithm uses the most efficient control power first and then refers to the less efficient ones, which leads to larger non-linear effects for those most deflected control surfaces. In the contrast, LP-DA utilizes all the available control surfaces with almost the same magnitude and hence reduces the largest deflections as well as the non-linear effects [45].

Another investigation about the impact of control allocation on trim drag of blended wing body aircraft was also carried out in Delft University of Technology by Huijts and Voskuijl [46]. The main objective of this research work was to determine the potential impacts of control allocation algorithms on the trim drag of blended wing body configuration by means of wind tunnel tests. The control surface deflections of a BWB wind tunnel model (same as the model mentioned in the preceding research project) were calculated with three different control allocation algorithms: daisy chain method, direct allocation method and fixed point iteration method for a set of trimming conditions with the aerodynamic database obtained with wind tunnel tests. The resulted control deflections were then implemented on the BWB wind tunnel model manually and actual control moments as well as aircraft lift and drag were tested with wind tunnel tests. The drag of final trimmed condition was tested and compared to the drag of clean untrimmed condition. In this way the trim drag of different control allocation algorithms were obtained and compared.

The results of the drag comparisons showed that different control allocation algorithms resulted in different trim drag. For the three control allocation algorithms examined in this project, the daisy chain method resulted in the most trim drag and the direct allocation method had the least trim drag penalty. This difference on trim drag is due to the fact that the daisy chain method uses the most efficient control surface first while the direct allocation and fixed point iteration methods use all the available control surfaces more or less evenly. For the trimming conditions considered in this project, no control saturation was encountered but the control deflections of daisy chain method were quite large, resulting in stronger separation on the deflected control surface and hence more trim drag penalty [46].

Based on the two research projects on BWB control allocations mentioned above, it can be seen that among all the control allocation algorithms investigated in these two projects the direct allocation method achieved the best control performance and had the least trim drag penalty. The main reason for the superiority of direct allocation method over the other methods is its even distribution of control deflections. The even distribution of all the available control effectors reduces the maximum deflection angles of those most effective control effectors therefore reduces the nonlinear effects and flow separation over the utilized control surfaces. From this point of view the way that direct allocation method utilizes all the available control effectors is implemented in the control allocation calculation of the modified VELA2 configuration of this project.

5.4.3 Control allocation of modified VELA2

The initial VELA2 configuration has 10 trailing edge ACS with 8 of them used for pitching control. The modified VELA2 has 4 thrust vectoring engines mounted above the trailing edge of the center fuselage. For the thrust vectoring control analysis under steady level flight conditions of this project, the ACS and vectoring nozzles are controlled separately. Therefore separate control allocations need to be built up for both ACS and vectoring nozzles.

Based on the discussion in the precedent section, the way that direct allocation method utilizes all the available control effectors for a certain controlled variable is used as the basis and guidance for the control allocation of ACS and vectoring nozzles, which means that for controlling the modified VELA2 by either ACS or vectoring nozzles all the available control effectors are designed to deflect evenly with the same magnitudes. This treatment of the deflection distributions greatly simplifies the control allocation problem of this project. According to the premise of evenly distributing all the available control effectors for a certain controlled variable, simple control allocation matrices can be easily built up for control effectors including both ACS and vectoring nozzles despite their control effectiveness matrices. The control allocation problem of this project then becomes the searching of two proper matrices $\mathbf{H}$ which drive the respective even deflections of ACS and vectoring nozzles under their separate pilot control inputs.

$$\mathbf{H} \cdot \mathbf{d}_{des} = \boldsymbol{\delta} \tag{5.11}$$

where

$\mathbf{H}$: control allocation matrix of either ACS or vectoring nozzles

$\mathbf{d}_{des}$: control inputs from either “pilot ACS” or “pilot TV”

$\boldsymbol{\delta}$: deflection angles of either ACS or vectoring nozzles, evenly distributed on every utilized control effector

The implementation of even distribution on the deflections of utilized control effectors works in a way that a particular ganging matrix is introduced to the explicit ganging control allocation algorithm. The ganging matrix eliminates the differences among the effectiveness of all control effectors, and forces all the available control effectors to deflect with the same magnitude, either in the same direction for pitching and yawing control effectors or in the opposite direction for rolling control effectors. The

ganging matrix therefore virtually combines all the available control effectors into one single control effector for a certain controlled variable. For the modified VELA2 configuration of this project there are 10 trailing edge ACS in total with the absence of 2 vertical tails. If the yawing control of the initial vertical tails is assumed to be accomplished by part of the remaining trailing edge ACS, with a proper ganging design of all the redundant ACS three pseudo deflections could generate the desired three controlled variables which refer to the three pilots inputs in this project (lateral control input x_a, longitudinal control input x_b, and directional control input x_p). The generating of the desired three controlled variables by the ganged 10 control effectors of the modified VELA2 could be expressed with the following equation:

$$\mathbf{B}^{3\times10}\mathbf{G}^{10\times3}\boldsymbol{\delta}_{pseudo}^{3\times1} = \mathbf{d}_{des}^{3\times1} \tag{5.12}$$

in which

$\mathbf{B}^{3\times10}$: 3 by 10 matrix, control effectiveness matrix of the 10 trailing edge ACS on 3 rotation directions

$\mathbf{G}^{10\times3}$: 10 by 3 matrix, ganging matrix of the 10 trailing edge ACS for 3 control inputs

$\boldsymbol{\delta}_{pseudo}^{3\times1}$: 3 by 1 vector, pseudo deflections for 3 control inputs, varying from -1 (lower deflection bound) to +1 (upper deflection bound) for each item

$\mathbf{d}_{des}^{3\times1}$: 3 by 1 vector, 3 controlled variables, i.e. the 3 pilot control inputs, varying from -1 (lower bound of control input) to +1 (upper bound of control input)

Then the calculation of deflections of the 3 pseudo control effectors can be expressed as a multiplication of a 3 by 3 pseudo control allocation matrix $\mathbf{H}_{pseudo}^{3\times3}$ and the controlled variable vector:

$$\boldsymbol{\delta}_{pseudo}^{3\times1} = \mathbf{H}_{pseudo}^{3\times3}\mathbf{d}_{des}^{3\times1} \tag{5.13}$$

where

$$\mathbf{H}_{pseudo}^{3\times3} = \left(\mathbf{B}^{3\times10}\mathbf{G}^{10\times3}\right)^{-1} \tag{5.14}$$

From equation (5.12) and (5.14) it is shown that a ganging matrix transforms a non-square control effectiveness matrix into a square one and makes it invertible. The calculation of the control allocation matrix becomes a standard matrix inverse control allocation algorithm.

When attention is turned back to the real conditions of the modified VELA2 ACS, it can now be realized that two group of pseudo control effectors exist with the absence of vertical tails. One group is the 8 trailing edge ACS (including 2 inner elevator, 2 inner elevons, 2 middle elevons, and 2 outer elevons) for pitching control, and the other group is the 8 trailing edge ACS (including 2 inner elevons, 2 middle elevons, 2 outer elevons, and 2 ailerons) for rolling control. No ACS are dedicated for yawing control when vertical tails are not included in the geometry model. The condition of the modified VELA2 can be explained with equation (5.13) as:

$$\begin{bmatrix} 0 & 1 & 0 \\ 1 & 0 & 0 \end{bmatrix} \begin{Bmatrix} x_a \\ x_b \\ x_p \end{Bmatrix} = \begin{Bmatrix} \delta_M \\ \delta_L \end{Bmatrix} \tag{5.15}$$

in which

$$\mathbf{H}_{ACS,pseudo} = \begin{bmatrix} 0 & 1 & 0 \\ 1 & 0 & 0 \end{bmatrix} \tag{5.16}$$

and

x_a, x_b, x_p : pilot control inputs in lateral, longitudinal and directional axes for ACS deflections

δ_M, δ_L : deflections of the ACS for longitudinal and lateral rotation controls

Expand the 2 by 3 pseudo control allocation matrix of the ACS of modified VELA2, which refers to the control authority of two groups of ACS on three rotation axes, to a control allocation matrix which refers to the control authority of each ACS on three rotation axes, the full control allocation matrix of the ACS of modified VELA2 in this project is obtained:

$$\mathbf{H}_{ACS} = \begin{array}{c} \begin{matrix} x_a & x_b & x_p \end{matrix} \\ \begin{bmatrix} 0 & 1 & 0 \\ 0 & 1 & 0 \\ 1 & 1 & 0 \\ -1 & 1 & 0 \\ 1 & 1 & 0 \\ -1 & 1 & 0 \\ 1 & 1 & 0 \\ -1 & 1 & 0 \\ 1 & 0 & 0 \\ -1 & 0 & 0 \end{bmatrix} \end{array} \begin{matrix} \text{left inner elevator} \\ \text{right inner elevator} \\ \text{left inner elevon} \\ \text{right inner elevon} \\ \text{left middle elevon} \\ \text{right middle elevon} \\ \text{left outer elevon} \\ \text{right outer elevon} \\ \text{left aileron} \\ \text{right aileron} \end{matrix} \tag{5.17}$$

where

$\mathbf{H}_{ACS}$: control allocation matrix for ACS deflections

By definition the trailing edge down deflection of ACS is positive. Similar to the control distribution of ACS, the deflected nozzles of the four engines for a certain control input are designed to deflect with the same magnitude. With the same method, the control allocation matrix of the four vectoring nozzles of the modified VELA2 of this project is:

$$\mathbf{H}_{TV} = \begin{matrix} y_a & y_b & y_p & \\ \end{matrix} \begin{bmatrix} 1 & 1 & 0 \\ 0 & 0 & 1 \\ -1 & 1 & 0 \\ 0 & 0 & 1 \\ 1 & 1 & 0 \\ 0 & 0 & 1 \\ -1 & 1 & 0 \\ 0 & 0 & 1 \end{bmatrix} \begin{matrix} \text{engine 1, Z axis} \\ \text{engine 1, Y axis} \\ \text{engine 2, Z axis} \\ \text{engine 2, Y axis} \\ \text{engine 3, Z axis} \\ \text{engine 3, Y axis} \\ \text{engine 4, Z axis} \\ \text{engine 4, Y axis} \end{matrix} \tag{5.18}$$

where

$\mathbf{H}_{TV}$: control allocation matrix for thrust vectoring nozzle deflections

y_a, y_b, y_p : pilot control inputs in lateral, longitudinal and directional axes for nozzle deflections

As explained in section 4.2.1 for the control allocation matrix of axisymmetric vectoring nozzles, every two rows in the control allocation matrix $\mathbf{H}_{TV}$ are used to control the respective deflections in longitudinal plane and lateral plane for every single vectoring nozzle. In this project, the first row of every two rows is used for longitudinal control while the second row is used for lateral control. The deflection angle of a vectoring nozzle has the same sign as an ACS when they are deflected in the same direction. The sequence number of the four engines is shown in Figure 3-21.

With the two separate control allocation matrix set up, the deflection angles of both ACS and vectoring nozzles of the modified VELA2 can be calculated under their respective control inputs, by multiplying an gearing ratio matrix which indicates the actual deflecting angle of each control effector w.r.t its control input. The forces and moments produced by the deflected ACS and vectoring nozzles can then be determined. This process is essential for solving the equations of motion to calculate the trim condition with particular pilot control inputs.

6 Analyses and results

When the aerodynamic performance database, engine performance map, mass and inertia of an aircraft is estimated and prepared for the updated Phalanx which has embedded thrust vectoring modules, it is ready to calculate the trim condition of the selected aircraft configuration controlled by both ACS and vectoring thrust under specified flight conditions. The analyses on the effects and effectiveness of thrust vectoring control with VELA2 BWB configuration in this thesis project are focused on longitudinal trimmed level flight conditions. Different combination of nozzle deflections and ACS deflections are tested under a set of flight condition. Mass and CG is varied to investigate the effects of aircraft mass and static margin on thrust vectoring control.

6.1 Nozzle deflections variation

The first set of flight mechanics simulations of the modified VELA2 configuration with thrust vectoring controls are under a fixed flight condition as well as fixed mass and CG location. The nozzle deflection angles of the four scaled JT9D turbofan engines are controlled manually from -20° to 20° in the longitudinal plane as shown in Figure 6-1. The definition of positive deflections of vectoring nozzles is the same as ACS which is defined to be positive with trailing edge down. Therefore the simulations start with maximum upward nozzle deflections and end with maximum downward nozzle deflections. The limitation of maximum nozzle deflections is arbitrarily determined by the author of this project and there are no theoretical constraints for this limit value. Practical constraints of maximum nozzle deflections may exist due to mechanical capabilities, but these constraints are dependent on particular designs and no identical limitations may exist. The step length of nozzle deflections is chosen to be 2°. Under the given flight condition there are 21 nozzle deflections tested hence 21 trimmed conditions simulated.

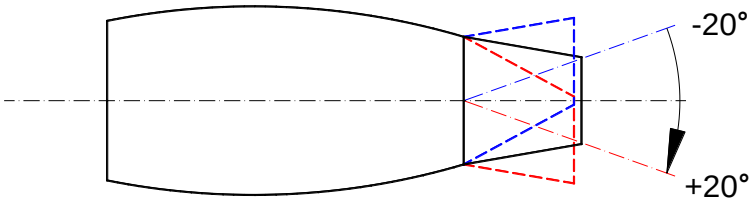

Figure 6-1 Nozzle deflections variation in longitudinal plane

When choosing one fixed flight condition as well as aircraft mass and CG condition for level trimmed flight simulations, the condition close to the cruise flight of VELA2 is of most interest. Therefore the flight altitude is set to be 9000 meters and a relatively moderate flight Mach number of 0.6 is chosen. The mass is set to be the OEM of VELA2 plus half of the movable mass which consists of the fuel mass and payload mass. The CG location is set to be identical with that of the OEM condition. Thus an aircraft mass of 495707 kg and CG location of 34.23 meters from the aircraft nose (which corresponds to a positive static margin of 1.2 meters) is set for the first set of flight simulations.

The moment coefficients of different aircraft components under the trimmed level flight conditions with 21 nozzle deflections are shown in Figure 6-2. The two thin blue lines represent the two control moments produced by ACS and thrust vectoring. The thick blue line is the total control moments, i.e. summations of moment coefficients produced by ACS and thrust vectoring. The black thick line is the moment coefficients of the aircraft main body which need to be trimmed by the control power. The magnitude of moment coefficient produced by the aircraft main body is always equal to that produced by all the aircraft controls under every trimmed condition, and with opposite signs.

Under the given simulation condition (aircraft flight condition together with mass and CG condition), the angles of attack variation w.r.t the change of nozzle deflections is shown in Figure 6-3. It can be observed that that the variation of angles of attack is very little from about 3.32° to 3.43° with a slight increment. Recalling the moment coefficient behavior of VELA2 main body shown in Figure 5-3 it is clear that the main body is producing negative pitching moments (nose down) within the calculated range of angles of attack. The combination of two control powers therefore needs to produce positive pitching moments (nose up) to trim the aircraft. At the starting point of the simulations when all four vectoring nozzles are deflected upward by 20°, the vectoring thrust are able to produce all the required trimming moments, hence the trimming moments left for ACS is almost zero. With the downward movement of nozzle deflections the trimming moments produced by vectoring thrust are decreasing and requirements for ACS are therefore increasing. At around -5° of nozzle deflections the thrust lines of four vectoring nozzles are crossing the CG of VELA2 and do not produce control moments, thus all the control moments are produced by ACS under this condition as can be seen from Figure 6-2. When the nozzles continue to move downwards the vectoring thrust start to produce nose down pitching moments in the same direction as aircraft main body. As shown in the figure that the trimming moments produced by ACS are more than the total control moments produce by the combination of ACS and vectoring thrust, with part of the ACS pitching moments counteracted by negative control moments produced by thrust vectoring.

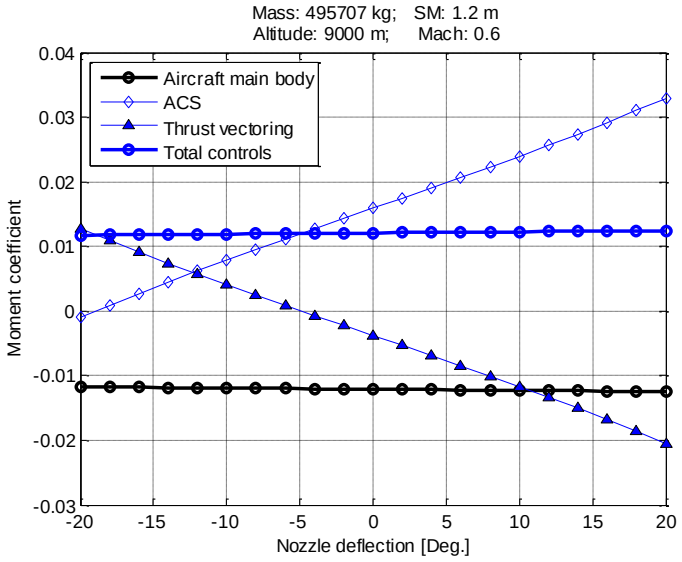

Figure 6-2 Moment coefficients variation w.r.t nozzle deflections

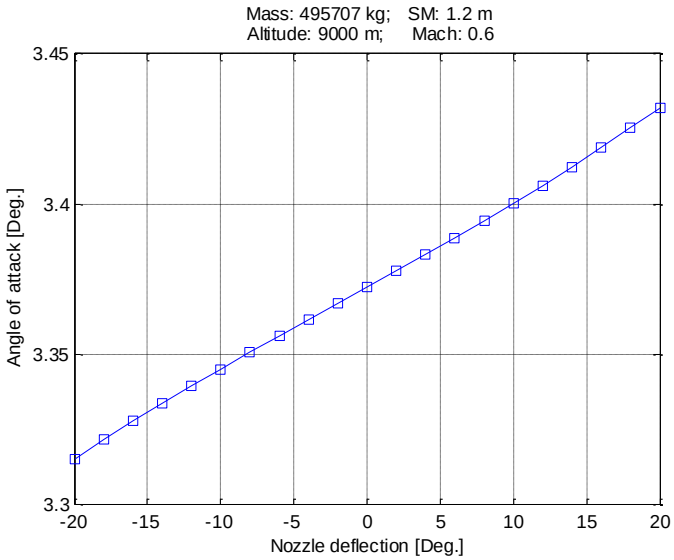

Figure 6-3 Angles of attack variation w.r.t nozzle deflections

The variation of aircraft angles of attack through the changing of nozzle deflections shown in Figure 6-3 can be explained with the lift coefficients produced by two control powers as shown in Figure 6-4. Under a given flight condition with fixed altitude and fight speed, the angle of attack of an aircraft is determined by the required lift coefficient. The lift coefficient of the modified VELA2 consists of the lift coefficients produced by main body, ACS and vectoring thrust. Engine thrust in the direction of lift can be considered as direct lift which also contributes to part of the total lift. For the modified VELA2 configuration, vectoring nozzles have relatively long moment arms than those of ACS. For a same amount of control moment the ACS needs a relatively larger amount of control force than vectoring nozzles. Therefore when vectoring nozzles are moving downwards through the simulations an increasing amount of downward control forces are produced when ACS are moving upwards simultaneously. The aircraft main body hence needs to produce an increasing amount of lift to keep the total lift of all aircraft components at a nearly fixed level as shown in Figure 6-4.

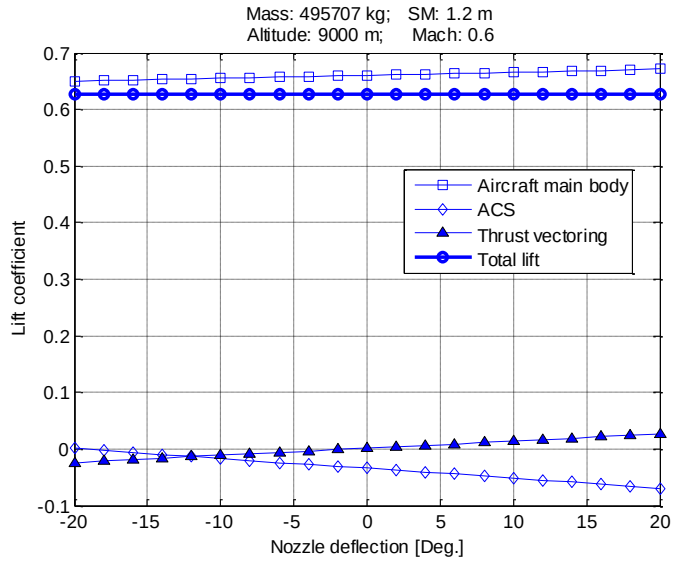

Figure 6-4 Lift coefficients variation w.r.t nozzle deflections

However it can also be observed that compared to the lift coefficient of the aircraft main body the lift contributions of control powers are significantly smaller, and the increment of lift coefficient of the aircraft main body is within small magnitude through the variation of nozzle deflections. This is the reason that when nozzle deflections varies from -20° to 20° the angles of attack of VELA2 only change by about 0.1°.

Drag of the aircraft comes from two components: the aircraft main body and the ACS, while drag of the engines is already counted when calculating engine net thrust. The drag coefficients through the variation of nozzle deflections are shown in Figure 6-5. The thick blue line represents the total drag of the aircraft including induced drag and profile drag. Wave drag is not included in this figure since at Mach number 0.6 the wave drag is negligible. Attention needs to be paid to the sign of the drag coefficient of the ACS. In Figure 6-5 it can be seen that the sign of ACS drag coefficient is negative. This is due to the method that Tornado uses to calculate the control derivatives of ACS. To calculate the first order derivatives of ACS, Tornado performs a central difference calculation using the pre-selected state and disturbing it by a small amount of deflection angle (usually 0.5 degrees) [32]. In this way the force and moment coefficients of ACS are the changes in the respective coefficients of the whole aircraft made by ACS deflections. Since Tornado is based on lifting surface theory, the estimation of induced drag is directly related to the amount of lift produced by the aircraft. Therefore if an ACS is deflected upward while the aircraft has a positive lift coefficient, the ACS deflection is contributing to a reduction of lift generation and a corresponding reduction in the drag of the aircraft, and the resulted contribution to the aircraft total drag from ACS deflection is with a negative sign as shown in Figure 6-5.

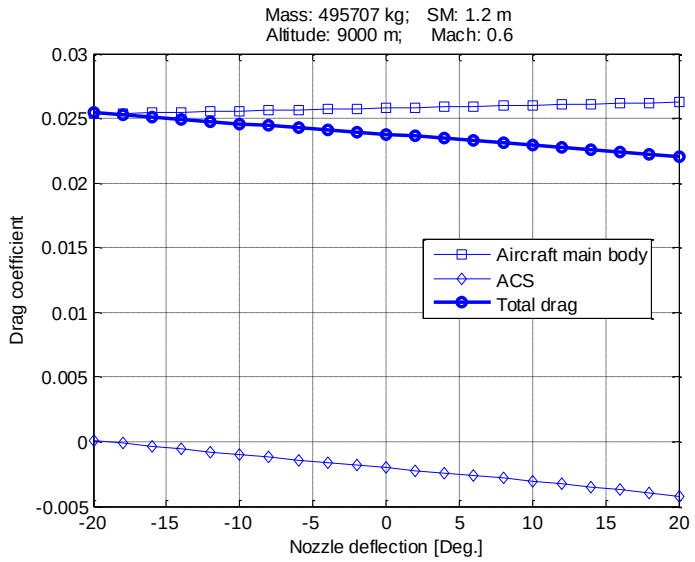

Figure 6-5 Drag coefficients variation w.r.t nozzle deflections

As already stated, at the starting point of this simulation condition the vectoring thrust is producing almost all of the required trimming moment, thus the ACS are not deflected and there is no change in the aircraft drag coefficient caused by ACS deflections. When nozzles are moving downwards, ACS are moving upwards correspondingly, and the consequent total drag of the aircraft is decreasing. This result shows that the application of thrust vectoring may result in a drag reduction during trimmed level flight conditions. For example it could be observed from both Figure 6-5 and Figure 6-6 that

through the downward changing of nozzle deflections, the ACS deflections are moving upward continuously (by definition upward deflection is negative) which results in a continuous decreasing of the aircraft total drag. Compared to the aircraft total drag with zero nozzle deflections, the aircraft total drag with maximum downward nozzle deflections is reduced by 18 counts from 0.0238 to 0.0220, which is about 7.6% of the aircraft total drag with zero nozzle deflections.

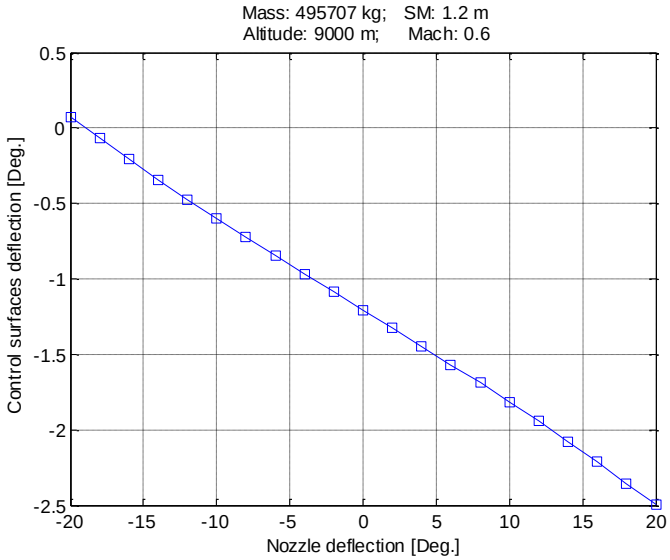

Figure 6-6 ACS deflections variation w.r.t nozzle deflections

However it is necessary to be aware that the drag calculation of the modified VELA2 configuration in this project is based on an aerodynamic tool with low fidelity level. Several factors including flow compressibility, viscosity and components interferences are not taken into account. Therefore the advantages in drag reduction may not be as obvious as observed here. At the same time the penalties of using thrust vectoring need to be realized as well. One main penalty of using thrust vectoring control is the increase of required total gross thrust. Both upward and downward nozzle deflections will lead to the increase of the required gross thrust as shown in Figure 6-7.

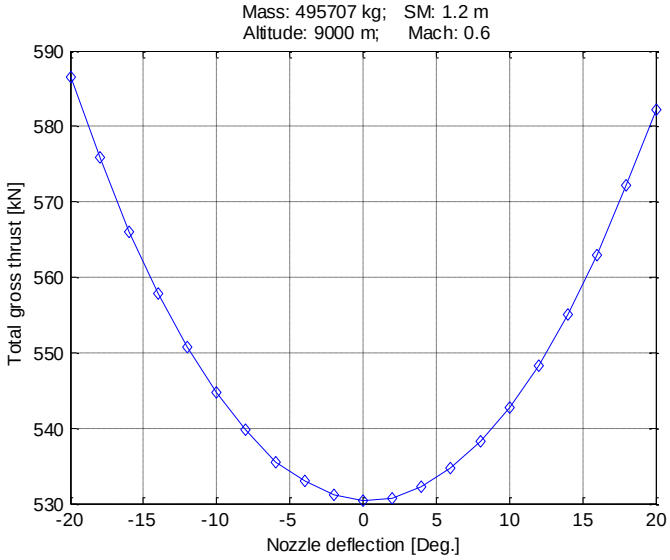

Figure 6-7 Total gross thrust variation w.r.t nozzle deflections

The increase of the required gross thrust due to nozzle deflections could be explained from this point of view: in order to keep the aircraft in a given trimmed level flight condition, a more or less fixed amount of total level thrust is required which counteracts with the total drag of the aircraft. When an engine nozzle is deflected, a gross thrust loss is encountered as explained in section 4.1.1, while only part of the reduced gross thrust is acting in the level flight direction. If the magnitude of the gross thrust component in the direction of flight speed is to be kept, the larger the nozzle deflection angle is, the more the total gross thrust of the engine is required.

The fuel consumption is directly related the total gross thrust of the engines. Therefore along with the increase of nozzle deflections, the total fuel consumption rate is also increasing to keep the trimmed level flight condition. As shown in Figure 6-8, compared to the fuel consumption rate with zero deflections, the total fuel consumption rate of four engines at +20° (maximum downward) of nozzle deflections is increased by up to 40.7% from 2.5522 kg/s to 3.5914 kg/s despite that the total aircraft drag is reduced by 7.6% under the same condition.

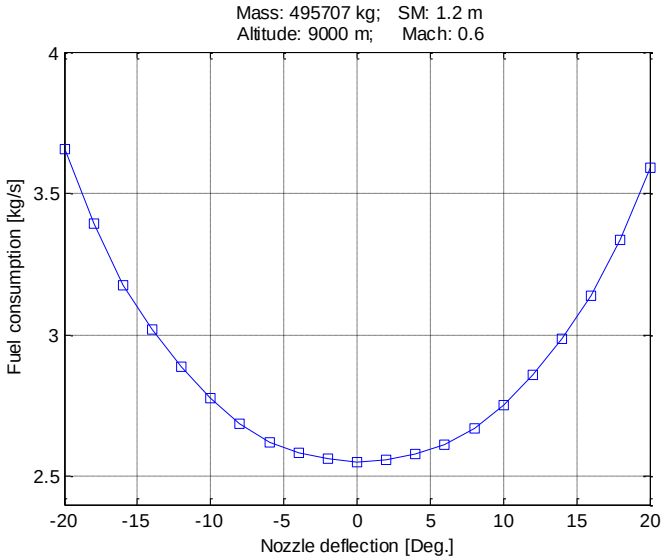

Figure 6-8 Fuel consumptions variation w.r.t nozzle deflections

6.2 Flight conditions variation

It is noticed from Figure 6-6 in the preceding section that when the vectoring nozzles are varying from -20° to 20° the variation of ACS deflections is only about 2.6° from 0.1° to -2.5°. The difference between the variation ranges of nozzle deflections and ACS deflections indicates a significant difference between the effectiveness of the two utilized control powers. It is clear that the control power of ACS is related to the flight conditions i.e. the flight altitude and flight speed, while the control power of vectoring thrust is related to the gross thrust of the engine. The gross thrust of engines is related to the drag of the aircraft for trimmed level flight and therefore is also related to the flight conditions. Thus it is necessary to compare the effectiveness of two control powers under different flight conditions. A more general term representing a flight condition which includes the effects of flight altitude and flight Mach number is the dynamic pressure q:

$$q = \frac{1}{2}\rho(h)\left[M \cdot a(h)\right]^2 \tag{6.1}$$

where the air density ρ and speed of sound a are functions of flight altitude. Dynamic pressure is therefore a representative parameter of combined effects of flight altitude and Mach number.

A series of flight conditions which cover a simplified typical flight envelop of civil transport aircrafts are chosen for thrust vectoring control analyses. The selected flight conditions cover a flight altitude range from sea level to 9000 m, and a Mach number range from 0.3 to the designed cruise Mach number of VELA2 which is 0.85. All the selected flight conditions are listed in Table 6-1 in the order of corresponding dynamic pressures, and are shown in a contour plot of varying dynamic pressure levels in Figure 6-9.

Table 6-1 Dynamic pressure of the analysed flight conditions

Index	Dynamic pressure (kg/m·s²)	Altitude (m)	Mach number	Index	Dynamic pressure (kg/m·s²)	Altitude (m)	Mach number
1	4416.842	3000	0.3	11	12269.01	3000	0.5
2	5284.28	6000	0.4	12	13772.63	9000	0.8
3	5379.935	9000	0.5	13	15548.01	9000	0.85
4	6383.48	0	0.3	14	16183.11	6000	0.7
5	7747.107	9000	0.6	15	17667.37	3000	0.6
6	7852.163	3000	0.4	16	17731.89	0	0.5
7	8256.687	6000	0.5	17	21137.12	6000	0.8
8	10544.67	9000	0.7	18	24047.25	3000	0.7
9	11348.41	0	0.4	19	25533.92	0	0.6
10	11889.63	6000	0.6				

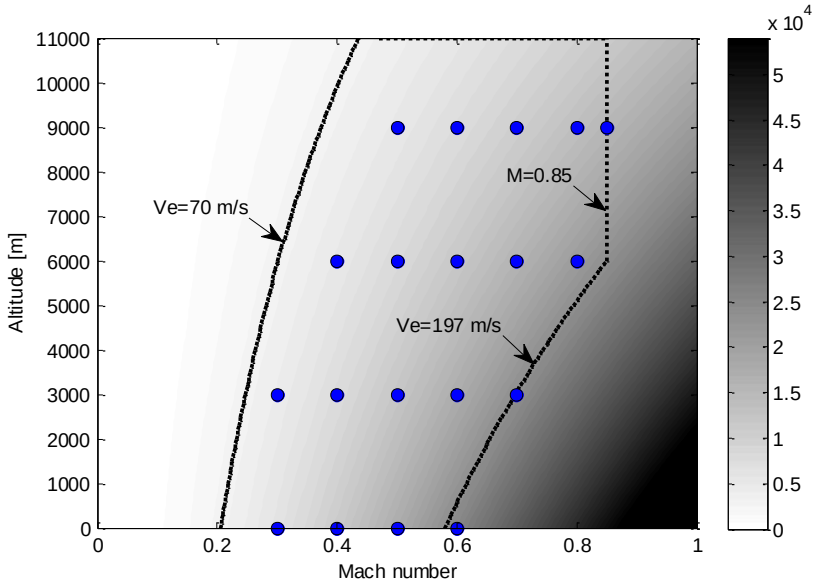

Figure 6-9 Flight conditions distribution w.r.t dynamic pressure contours

The dark area close to the right and bottom of Figure 6-9 represents the flight conditions with high dynamic pressure, while the light area close to the left and top represents the flight conditions with low dynamic pressure. The selected flight conditions are evenly distributed and enclosed in an envelope with minimum equivalent airspeed of 70 m/s, maximum equivalent airspeed of around 200 m/s, maximum flight altitude of 11000 m and maximum Much number of 0.85, which represent a more or less typical flight envelope of civil transport aircrafts.

When comparing the effectiveness of thrust vectoring control to conventional ACS control, a parameter named control efficiency ratio is defined in this thesis project. The control efficiency ratio is defined to be the ratio between the control derivatives of thrust vectoring and the control derivatives of conventional ACS. Similar to the ACS the coefficients of thrust vectoring controls are defined as:

$$\begin{cases} C_{x_{TV}} = \dfrac{F_{x_{TV}}}{q \cdot S} \\ C_{y_{TV}} = \dfrac{F_{y_{TV}}}{q \cdot S} \\ C_{z_{TV}} = \dfrac{F_{z_{TV}}}{q \cdot S} \\ C_{l_{TV}} = \dfrac{L_{TV}}{q \cdot S \cdot \bar{c}} \\ C_{m_{TV}} = \dfrac{M_{TV}}{q \cdot S \cdot \bar{c}} \\ C_{n_{TV}} = \dfrac{N_{TV}}{q \cdot S \cdot \bar{c}} \end{cases} \tag{6.2}$$

with the parameters defined by

$F_{x_{TV}}$	$\equiv x_b$-component of vectoring thrust force vector
$F_{y_{TV}}$	$\equiv y_b$-component of vectoring thrust force vector
$F_{z_{TV}}$	$\equiv z_b$-component of vectoring thrust force vector
L_{TV}	$\equiv$ vectoring thrust rolling moment
M_{TV}	$\equiv$ vectoring thrust pitching moment
N_{TV}	$\equiv$ vectoring thrust yawing moment
$C_{x_{TV}}$	$\equiv x_b$-component of vectoring thrust force coefficient
$C_{y_{TV}}$	$\equiv y_b$-component of vectoring thrust force coefficient
$C_{z_{TV}}$	$\equiv z_b$-component of vectoring thrust force coefficient
$C_{l_{TV}}$	$\equiv$ vectoring thrust rolling moment coefficient
$C_{m_{TV}}$	$\equiv$ vectoring thrust pitching moment coefficient
$C_{n_{TV}}$	$\equiv$ vectoring thrust yawing moment coefficient

The derivatives of thrust vectoring moment coefficients are calculated in the same way as the control derivatives of conventional ACS with central difference method. The pitching moment coefficients produced by vectoring thrust with nozzle deflection angles of -2° and 2° are taken for the calculation of control derivatives of vectoring thrust. Control derivatives of vectoring thrust is representative of its relevant control effectiveness. The control derivatives of a control effector show the magnitude of moment the control effector is capable to produce with a unit amount of deflection. The equation of calculating the control derivatives of vectoring thrust is given in equation (6.3).

$$C_{m_{TV},\delta} = \frac{C^2_{m_{TV}} - C^1_{m_{TV}}}{\delta^2_{TV} - \delta^1_{TV}} \tag{6.3}$$

In order to compare the effectiveness of thrust vectoring control and conventional ACS control, the effectiveness of ACS controls is of importance. When the eight pitching control ACS of the modified VELA2 are ganged together as one control effector, the summation of the control derivatives of all eight pitching control ACS is shown in Figure 6-10. Due to the calculation method the pitching control derivatives of control surfaces are normally negative. The absolute value of the summation represents the effectiveness of pitching control with the conventional ACS of the VELA2 configuration. It can be observed that based on the aerodynamic tools used for this project, which does not take the compressibility and viscosity effects of flow into account, the control derivatives of ACS are only relative to the aircraft angle of attack and are independent of the flow conditions.

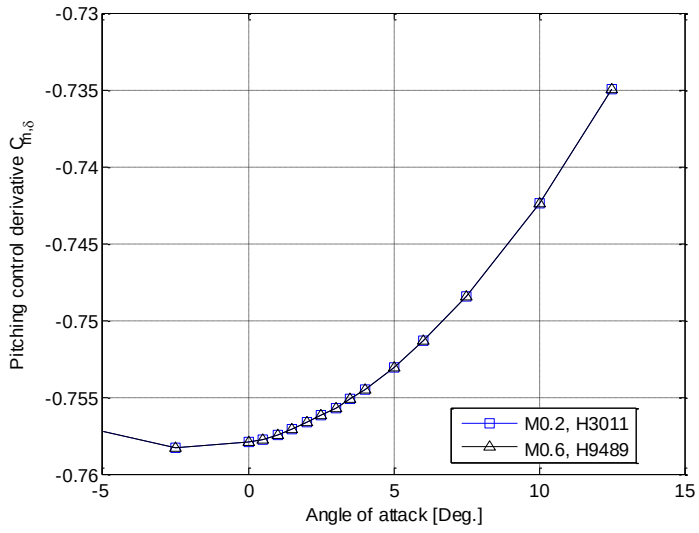

Figure 6-10 Control derivatives of the ganged pitching control ACS of VELA2

It is already noticed in Figure 6-3 that the angle of attack of the aircraft is varying very slightly when the vectoring nozzles deflect from maximum upward angle to maximum downward angle. The variations of the aircraft angle of attack under the two extreme analyzed conditions, one with the minimum analyzed dynamic pressure and the other one with the maximum analyzed dynamic pressure, are shown in Figure 6-11. The variation of angle of attack of the first condition is about 0.16° and the variation of the second condition is about 0.09°. Therefore for every analyzed flight condition it is acceptable to take the control derivatives of ACS under one nozzle deflection condition as the representative ACS control effectiveness. In this project the control derivatives of ACS with zero nozzle

deflections under every analyzed flight condition is used for the comparisons with the effectiveness of thrust vectoring control.

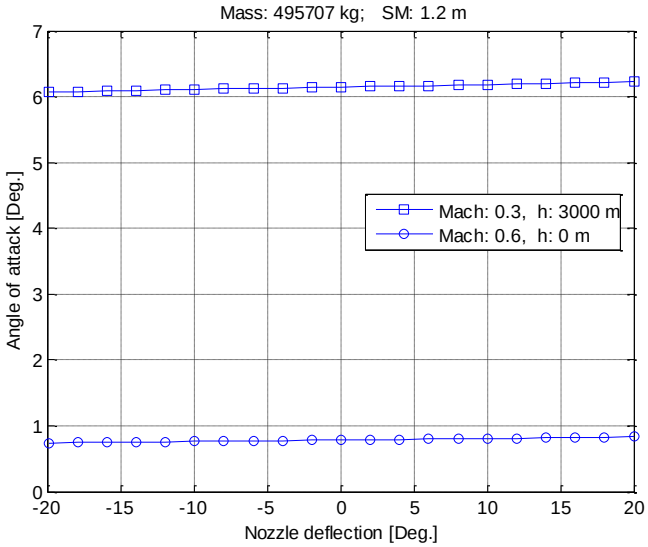

Figure 6-11 Aircraft angle of attack variations under two analysed flight conditions

The aircraft angles of attack with zero nozzle deflections under the analyzed flight conditions are shown in Figure 6-12. For level trimmed flight of an aircraft under various flight conditions with the same mass condition, a flight condition with lower dynamic pressure requires a higher angle of attack i.e. higher lift coefficient. With the increase of dynamic pressure the required lift coefficient hence angle of attack is reduced. Combining the characteristics of VELA2's pitching control derivatives given in Figure 6-10, the pitching control effectiveness of VELA2's ACS (the absolute value of the pitching control derivatives) is increasing along with the increase of flight dynamic pressure as shown in Figure 6-13. However the pitching control effectiveness of thrust vectoring (the absolute value of the pitching control derivatives of thrust vectoring) is decreasing along with the increase of flight dynamic pressure.

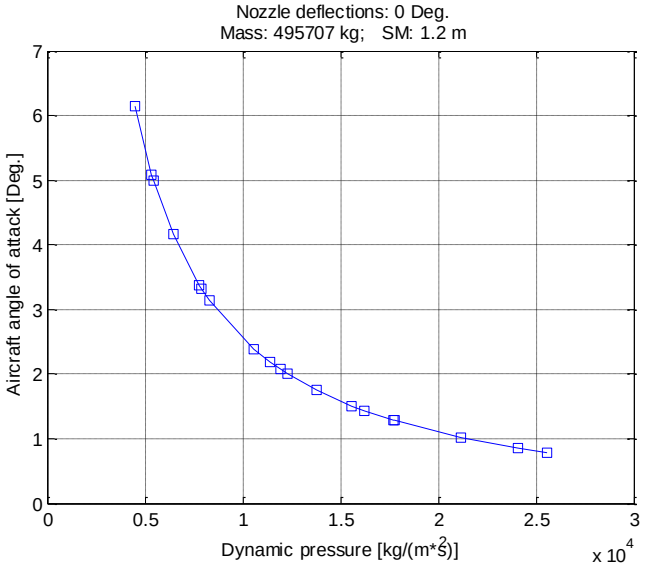

Figure 6-12 Angles of attack of the modified VELA2 under different flight conditions

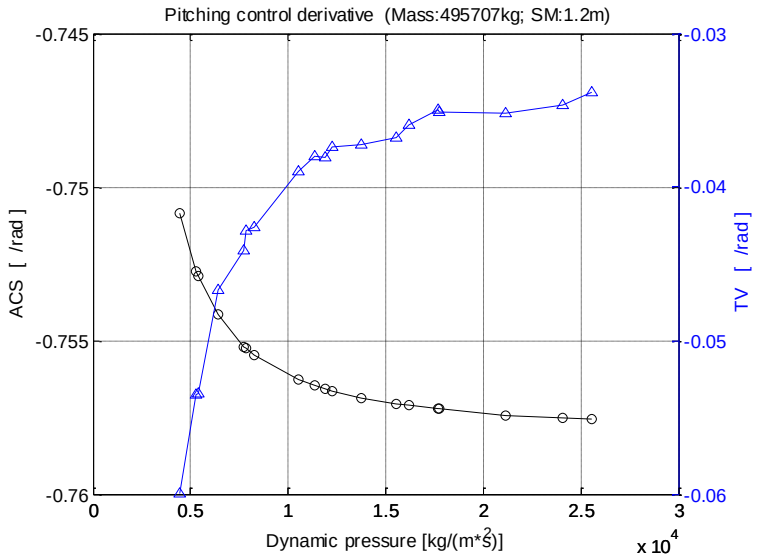

Figure 6-13 Variation of control derivatives under different flight conditions

The decrease of the control effectiveness of thrust vectoring along with the increase of dynamic pressure is due to the definition of control moment coefficient of thrust vectoring. The control moment coefficient of thrust vectoring is the moment produced by thrust vectoring divided by the corresponding flight dynamic pressure. Along with the increase of flight dynamic pressure the gross thrust of engines as well as the control moment produced by thrust vectoring has a lower growth rate. Therefore the absolute value of the control moments divided by the corresponding dynamic pressure decreases when the flight dynamic pressure increases. The comparisons between the two control powers can be made more directly with the derivatives of the two control moments as shown in Figure 6-14. The derivative of control moment is the control moment produced by a unit deflection angle of the control effector. For the flight conditions analyzed in this project, the absolute variation of the derivatives of pitching moment produced by VELA2's ACS is $5.77 \times 10^8\ N \cdot m/rad$, while the respective variation of thrust vectoring is only $2.16 \times 10^7\ N \cdot m/rad$.

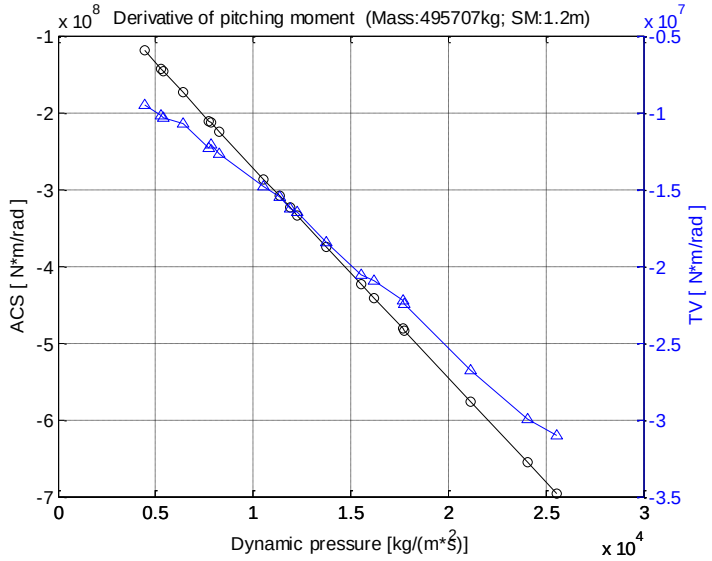

Figure 6-14 Variation of derivatives of pitching moment under different flight conditions

The ratio between the control derivatives of thrust vectoring and the control derivatives of conventional ACS clearly indicates the relative effectiveness of thrust vectoring control to conventional ACS control. The control effectiveness ratio is defined as:

$$\xi = \frac{C_{m_{TV},\delta}}{C_{m_{ACS},\delta}} \tag{6.4}$$

From the calculation method it can be realized that the result of control effectiveness ratio will be the same no matter the denominator and numerator of equation (6.4) are taken from either the moment derivatives or the moment coefficient derivatives. The values of the control effectiveness ratio of the modified VELA2 configuration is shown in Figure 6-15.

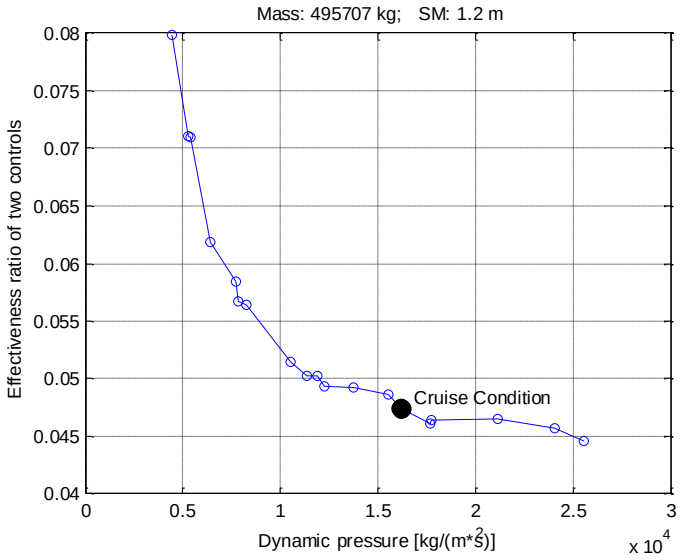

Figure 6-15 Control effectiveness ratio under various flight conditions

From the plotted line three conclusions can be made:

- For level trimmed flight conditions, in general the control effectiveness of vectoring nozzles of the modified VELA2 configuration is much lower than the control effectiveness of conventional ACS. The maximum control effectiveness ratio under all the analyzed flight conditions is only 7.98%.
- Along with the increase of flight dynamic pressure the effectiveness ratio between thrust vectoring control and conventional ACS control of the modified VELA2 configuration decreases. Under all the analyzed flight conditions the control effectiveness ratio decreases from 7.98% to 4.46% when the flight dynamic pressure increases from $4416.8\ kg/(m \cdot s^2)$ to $25533.9\ kg/(m \cdot s^2)$. This trend is already explained with Figure 6-13 and Figure 6-14. With the increase of dynamic pressure, the control derivatives of ACS of VELA2 increases while the control derivatives of thrust vectoring decreases. Combining the changes in the effectiveness of two control powers w.r.t various dynamic pressure leads to a decline of the effectiveness ratio between the two control powers.
- The decline of the control effective ratio in low dynamic pressure region is steeper than that in the high dynamic pressure region. This characteristic is due to the fact that the change of the aircraft angle of attack, hence the change of the control derivatives, becomes more moderate in the high dynamic pressure region than that in the low dynamic pressure region as shown in Figure 6-12.

6.3 Mass and CG variation

During level steady flight of an aircraft the requirement of control moment for trimming the aircraft comes from the existence of either positive or negative static margin. An aircraft with a positive static margin, which normally is the case for a civil transport aircraft for safety considerations, has its CG ahead of its aerodynamic center. During level steady flight the lift will generate nose down moment which requires the control surfaces to deflect upwards and produce a nose up moment to trim the aircraft. In the contrast, an aircraft with a negative static margin requires its control surfaces to deflect downwards during level trimmed flight conditions. The magnitude of trim moment required from control surfaces is dependent on the mass and static margin of the corresponding aircraft. Therefore for the investigation of trimming an aircraft with thrust vectoring controls in this project, the mass and static margin of the analyzed aircraft have obvious influences on the analysis results, and it is necessary to test the effectiveness of thrust vectoring control under different aircraft mass and static margin conditions.

In this thesis project thrust vectoring control simulations are carried out under 7 combinations of mass and static margin conditions. The variation of mass conditions of the modified VELA2 configuration is accomplished by changing the fuel and payload mass, while the variation of static margin is conducted by changing the location of the aircraft CG w.r.t the aircraft aerodynamic center. The combinations of aircraft mass and CG locations analyzed in this project are shown in Figure 1-5 and Table 5-7.

It is easy to speculate qualitatively the influences of aircraft mass on the effectiveness of thrust vectoring control under level trimmed flight conditions. As already clarified in the preceding section that the control power of thrust vectoring is related to the gross thrust of the engines, an increase of the aircraft mass will result in an increase of the effectiveness of thrust vectoring control under the same level trimmed flight condition. The logic of this relation can be explained with the following relation chain:

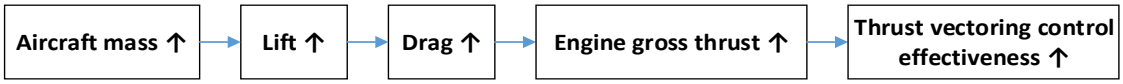

Figure 6-16 Relation chain from aircraft mass to thrust vectoring control effectiveness

It needs to be clarified that the control effectiveness of a control effector is a relative concept. It represents the control moment produced by a unit deflection of the corresponding control surface/vectoring nozzle. A higher control effectiveness dose not simply guarantee a lower deflection angle. The control deflection is also related to the magnitude of moment that is to be balanced by the control powers. For example when the increase of control effectiveness of vectoring thrust is caused by an increase of the aircraft mass, the moment produced by the aircraft main body to be balanced by the control effectors is increased simultaneously.

The influences of CG location on the effectiveness of thrust vectoring control are not so obvious. Two of the seven CG and mass conditions analyzed in this project are compared to explain the effects of CG locations on the effectiveness of thrust vectoring control. One mass and CG condition is the MTOM

with the most forward CG location (the most positive static margin), and the other mass and CG condition is the MTOM with the most aft CG location (the most negative static margin). When considering the variation of the effectiveness of thrust vectoring control due to the variation of aircraft CG locations under a fixed flight condition, it is straight forward to start with the variation of the magnitude of engine gross thrust and following an inverse relation chain as indicated in Figure 6-16 to find the origin which leads to the change of effectiveness of thrust vectoring control.

The gross thrust of the four scaled JT9D turbofan engines used for the modified VELA2 under the two selected aircraft CG conditions are shown in Figure 6-17. Under the same flight condition and aircraft mass value the aircraft with a negative static margin requires more engine thrust for steady level flight than the aircraft with a positive static margin. This indicates that the effectiveness of thrust vectoring control of the modified VELA2 with a negative static margin is higher than that of the VELA2 with a positive static margin.

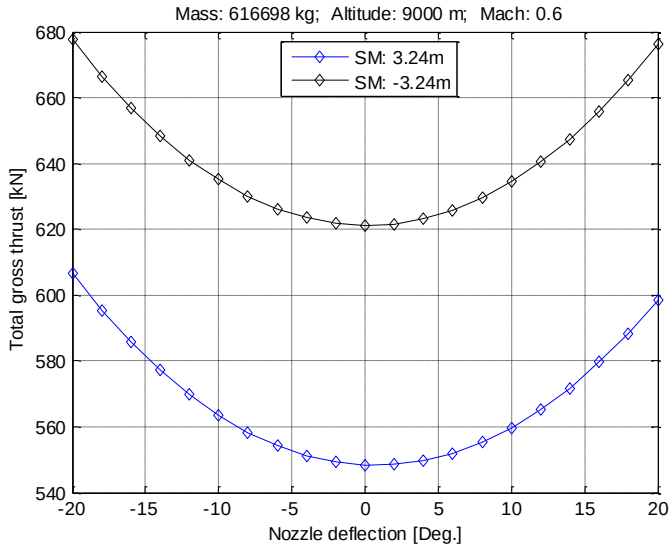

Figure 6-17 Gross thrust of engines of the modified VELA2 under two CG conditions

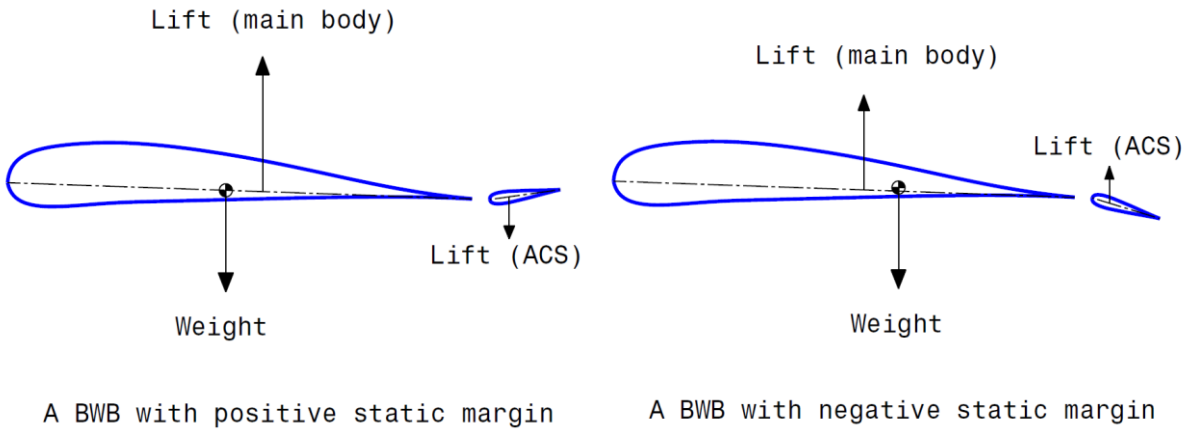

Figure 6-18 Longitudinal trim of a BWB with positive/negative static margin

The location of CG of a BWB configuration with positive/negative static margin and the direction of the required trim force generated by the trailing edge ACS is shown in Figure 6-18. With the same aircraft mass the required total lift is the same. A BWB with a positive static margin has its ACS deflecting upwards under level trimmed flight conditions, and the total lift is the lift of main body subtracted by the downward lift of ACS. In the contrast, a BWB with a negative static margin has its ACS deflecting downwards under level trimmed flight conditions, and the total lift is the lift of main body added by the lift of ACS. Therefore different CG locations (static margins) lead to different lift distributions on aircraft components, and further lead to different drag distributions.

Even though the total lift of the two different aircraft configurations with different CG locations are the same since they should be equal to the identical aircraft weight, the resulted total drags of the two aircraft configurations are not the same. The total drags and their respective drag components of the two aircraft conditions are shown in Figure 6-19. The black lines represent the drag distributions of the configuration with negative static margin while the blue lines represent the configuration with positive static margin. Differences can be observed on the drags generated by the main body, ACS of the two configurations. The resulted total drag of the two configurations are also different. From the VELA2 configuration with a positive static margin to the one with a negative static margin, the lift produced by the aircraft main body is reduced, and the upward lift produced by the ACS is increased. The reduction of lift produced by main body is equal to the increment of lift produced by ACS to keep a constant lift. At the same time, the drag produce by aircraft main body is reduced, while the drag produced by ACS is increased consequently. However the drag reduction from the aircraft main body is less than the magnitude of drag increase from the ACS as can be found from Figure 6-19. This difference in the magnitude of drag variation finally result in an increase of total drag when the aircraft static margin changes from positive to negative.

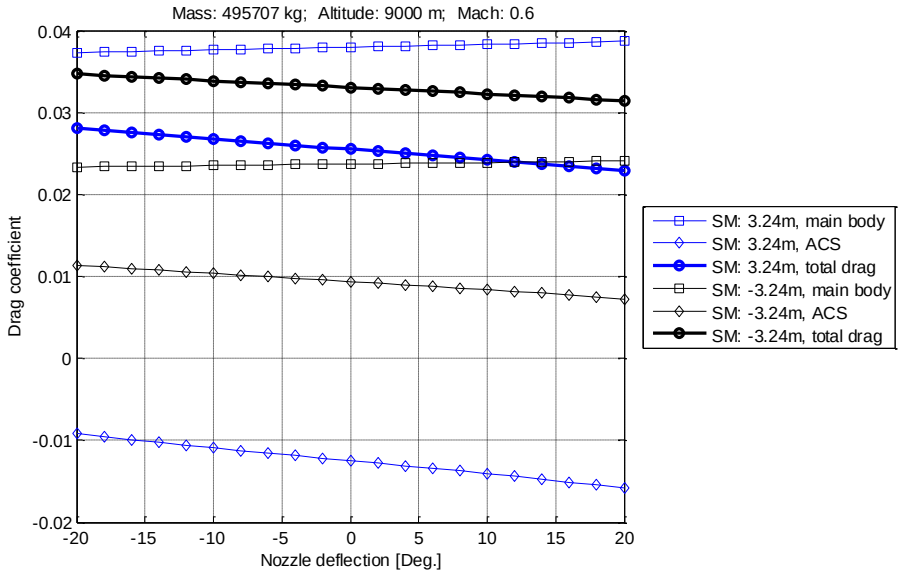

Figure 6-19 Drag distributions of two VELA2 configurations with different static margins

The difference between the drag variations of the two aircraft components (aircraft main body and ACS) comes from the characteristics of nonlinearity of drag polar. For either main wings or tails of an aircraft the drag increase is steeper under large angles of attack than the drag increase under small

angles of attack. For the VELA2 configurations from maximum positive static margin to maximum negative static margin under a flight condition of 9000 m and Mach 0.6 and with zero nozzle deflections, the variation of aircraft angles of attack and ACS deflections are listed in Table 6-2.

Table 6-2 Variation of aircraft angles of attack and ACS deflection angles

	VELA2 with max positive static margin (3.24m)	VELA2 with max negative static margin (-3.24 m)	Variation
Aircraft angle of attack (°)	4.82	3.06	1.76
ACS deflection (°)	-5.24	6.18	11.42

The variation of the deflection angle of ACS is much larger than the variation of the angle of attack of main body. Due to the nonlinearity of drag polar the drag variation of ACS is therefore larger than the drag variation of the main body. The difference between the drag variations of aircraft main body and ACS results in a drag increment when the static margin is changed from the most positive value to the most negative value, and further results in an increment of the required total gross thrust for level trimmed flight conditions.

In short, when the CG location of the modified VELA2 moves rearwards, there will be a reduction in the drag generated by the aircraft main body, and simultaneously there will be a greater increase in the drag generated by the trailing edge ACS. The increment of the resulted total drag leads to an increase of the required total engine gross thrust, and further results in a growth of the effectiveness of thrust vectoring control.

Under a fixed flight condition of 9000 m and Mach 0.6, the total drags of the modified VELA2 with seven different mass and CG conditions are given in Figure 6-20. For every mass and CG condition, the vectoring nozzles are deflected from -20° to 20°. It is shown that compared to the variation of CG location the variation of aircraft mass has a dominating influence on the drag variations of VELA2.

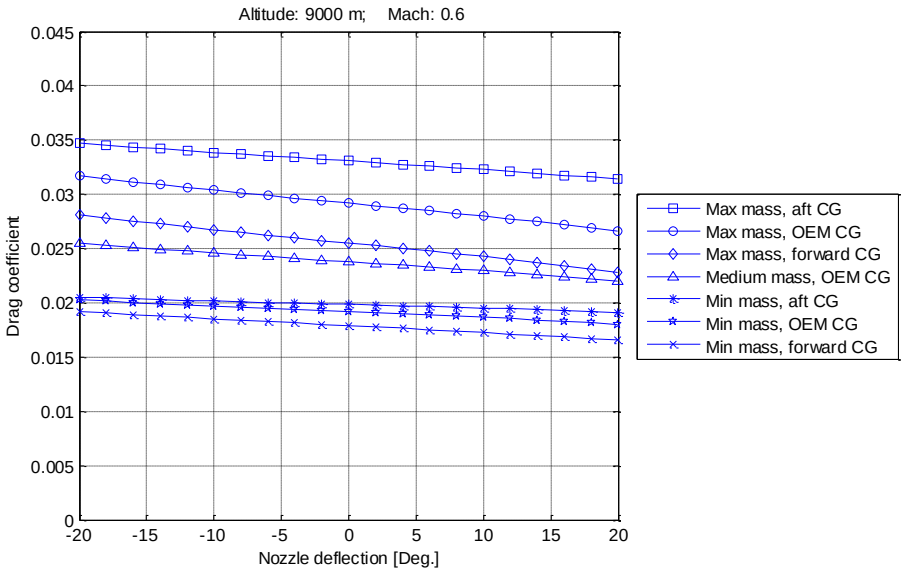

Figure 6-20 Total drag of the modified VELA2 under different mass and CG conditions

Corresponding to the drag variations of the modified VELA2, the engine total gross thrust variations under different mass and CG conditions are given in Figure 6-21. The order of the total gross thrust variation is affected by both the mass of the aircraft and the CG location. The aircraft configuration with the maximum mass and the most negative static margin has the most gross thrust requirement, while the aircraft configuration with the minimum mass and the most positive static margin has the least gross thrust requirement.

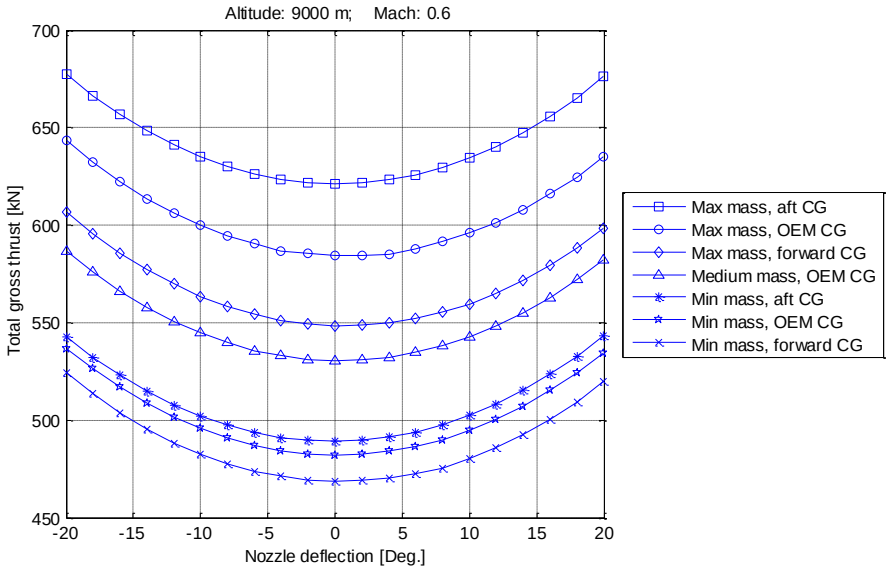

Figure 6-21 Total gross thrust of the modified VELA2 under different mass and CG conditions

The effectiveness ratio of thrust vectoring control to the conventional ACS control of the modified VELA2 is calculated with 7 different mass and CG conditions. With each mass and CG condition of the thrust vectoring simulation, 19 flight conditions are considered. The results are shown in Figure 6-22.

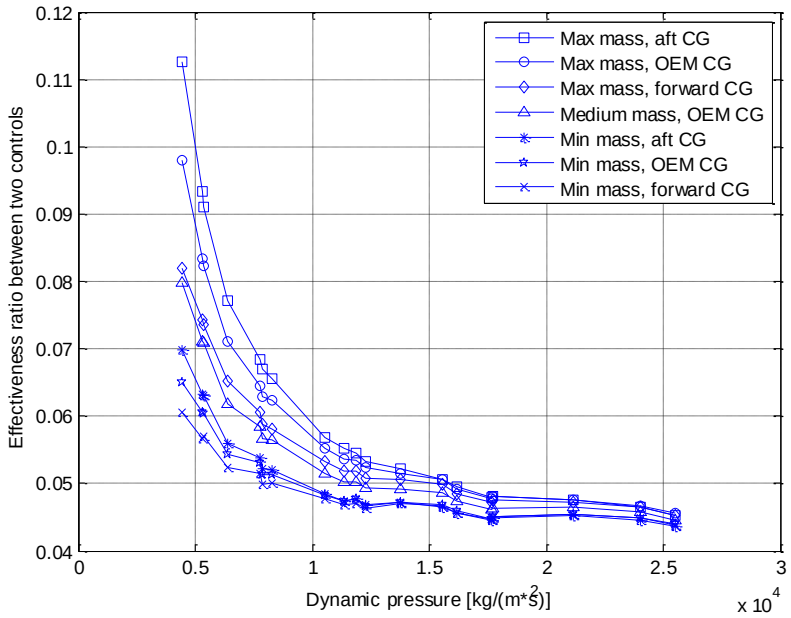

Figure 6-22 Effectiveness ratio of two controls under various analysis conditions

Combining the influences of aircraft mass and CG locations as well as the aircraft flight conditions on the effectiveness of thrust vectoring control as shown in Figure 6-22, it can be observed that:

- Under the same flight condition and CG location, thrust vectoring control is more effective for an aircraft with heavier mass than the same aircraft with lighter mass
- Under the same flight condition and mass condition, thrust vectoring control is more effective for a more rearward CG location than the same aircraft with a more forward CG location
- The influences of aircraft mass and CG location on the effectiveness of thrust vectoring control are more obvious under low dynamic pressure flight conditions. The variation of the effectiveness of thrust vectoring control due to the change of aircraft mass and CG location under the least dynamic pressure condition considered in this project is about 5.21%, while the variation under the most dynamic pressure condition is only about 0.14% which is almost negligible

7 Conclusions and Recommendations

The objective of this thesis project is to carry out flight mechanic analysis on thrust vectoring control with a BWB configuration. The focus of the flight mechanics analysis of this project is on level trimmed flight conditions in longitudinal plane. Thrust vectoring and conventional aerodynamic control surfaces are utilized simultaneously to trim the aircraft under various flight conditions, as well as various aircraft mass and CG conditions. The influences of different nozzle deflections, aircraft flight conditions, aircraft mass and CG conditions on the effects and effectiveness of thrust vectoring are simulated extensively with a flight mechanics toolbox named Phalanx. Based on the implementations of flight mechanics analysis on thrust vectoring and the simulation results several conclusions can be drawn. Recommendations for further improvements on the analyses work are given in this chapter.

7.1 Conclusions

The modelling of thrust vectoring is essential for carrying out the flight mechanics analysis on thrust vectoring control. A thrust vectoring model is successfully built up and embedded in the flight mechanics toolbox through this thesis project. The model contains two main modules, one is the calculation of nozzle deflection angles based on nozzle deflection control inputs, and the other one is the calculation of the thrust loss based on nozzle deflection angles.

For real time simulation of thrust vectoring control during a flight mechanics analysis, an analytical solution of the thrust loss due to nozzle deflections is appropriate. An algorithm developed by Erich Wilson which integrates the compressible flow equations of nozzle internal flow into the nozzle thrust equations is adopted in this project. Based on this algorithm it is possible to take into account the engine thrust loss due to nozzle deflections. By integrating the compressible flow equations into the nozzle thrust equation, the variation of nozzle section areas due to nozzle deflections is embedded in the nozzle thrust equation. It is in this way that the analytical algorithm developed by Erich Wilson calculates the thrust loss of an engine caused by the utilization of thrust vectoring.

Controlling vectoring nozzles is similar to the controlling of conventional aerodynamic control surfaces. The nozzle deflection control module developed in this project calculates the nozzle deflection angles from nozzle deflection control inputs. Even though the flight mechanics simulations conducted in this project are only within the longitudinal plane, the nozzle control module is capable of controlling the nozzles deflecting in both lateral and vertical directions, which makes the control algorithm of nozzle deflections different from the controlling of conventional aerodynamic control surfaces. The simulations of this project are within static flight mechanics domain, therefore a dynamic model of the nozzle control effectors is not developed for the nozzle control module.

Four turbofan engines and eight aerodynamic control surfaces at the wing trailing edge of the modified VELA2 configuration are used to trim the aircraft during level steady flight conditions. Explicit ganging control allocation algorithm is used to develop the control allocation matrix for both ACS and vectoring nozzles. The determination of the explicit ganging matrix is based on several researches and investigations on the influences of different control allocation algorithms on the control power and

aerodynamic performance of a BWB wind tunnel model. It is then chosen to deflect all the available ACS or vectoring nozzles evenly for pitching controls for a satisfactory control performance.

At a beginning stage of investigating the effects and effectiveness of thrust vectoring control under level trimmed flight conditions, an integrated control law and control allocation of ACS and vectoring thrust is not developed yet. It is therefore chosen to control the ACS and thrust vectoring separately to try various combinations of ACS and thrust deflections under a series of flight conditions as well as different aircraft mass and CG conditions, in order to have extensive investigations on the effects and effectiveness of thrust vectoring control compared to conventional ACS control. Combinations of seven aircraft mass and CG conditions, nineteen flight conditions and twenty-one nozzle deflections are simulated through this project.

From the simulation results it is shown that under steady level flight conditions the effectiveness of thrust vectoring control is much lower than the effectiveness of conventional ACS controls. Thrust vectoring control does have the capability to trim the modified VELA2 configuration solely under some of the analysed flight conditions with all the ACS not deflected, but with much larger deflection angles compared to the deflections of ACS when the aircraft is trimmed solely by ACS. Under the flight condition of 9000 m and Mach 0.6, 495707 kg of aircraft mass and 1.2 m of positive static margin, when nozzle deflection angles of the modified VELA2 configuration change from -20° to 20° the corresponding variation of ACS deflection angles required to keep VELA2 in trimmed conditions is only 2.57° from 0.07° to -2.5°.

In some cases thrust vectoring application is beneficial to reduce the induced drag of an aircraft because it helps to reduce the required control deflections from ACS hence the resulted induce drag generated by ACS. However this benefit is easily eliminated by the increase of engine gross thrust due to nozzle deflections. Under steady level flight conditions, a more or less fixed amount of level thrust is required to counteract with the aircraft drag. When engine nozzles are deflected, two obvious consequences are introduced, one is the thrust loss due to nozzle deflections, and the other one is that only part of the nozzle thrust is in the direction of flight speed counteracting with aircraft drag. Therefore the larger the nozzle deflection angel is, the higher the requirement will be on the engine gross thrust for steady level flight conditions, and the fuel consumption rates of the engines will consequently increase due to nozzle deflections.

A parameter called control effectiveness ratio is introduced in this project. It is the ratio between the control derivatives of thrust vectoring and the control derivatives of conventional ACS. This parameter directly reflects the relative effectiveness of the two control powers used for trimming the modified VELA2 in this project. Since the control derivatives of ACS are related to the aerodynamic performance of the corresponding ACS, and the control derivatives of thrust vectoring are related to the corresponding engine gross thrust which are in turn related to the aircraft flight conditions, the control effectiveness ratio between the two control powers is therefore highly dependent on the flight conditions concerned. Under steady level flight conditions with a high flight altitude and a low flight speed which leads to a low flight dynamic pressure, the control effectiveness ratio is relatively large compared to a lower dynamic pressure flight condition which corresponds to a lower flight altitude and higher flight speed.

Since in this project thrust vectoring is used to work with conventional ACS to balance the pitching moments generated by the aircraft main body under steady level flight conditions, and the pitching

moments of main body are dependent on the aircraft mass and the aircraft static margin, therefore the mass and CG location also have influences on the effectiveness of thrust vectoring control. Aircraft mass has an obvious influence on the thrust vectoring control effectiveness because with a heavier aircraft mass under the same flight condition, a higher engine gross thrust is required to maintain the required flight condition which leads to a higher effectiveness of thrust vectoring control. However a higher control effectiveness dose not simply guarantee a lower control deflection when the increase of control effectiveness is caused by an increase of aircraft mass.

The CG location of an aircraft influences the effectiveness of thrust vectoring control in an obscurer way than the aircraft mass does. When the CG location of an aircraft moves rearwards by either reducing the positive static margin or increasing the negative static margin, the aircraft angle of attack will reduce consequently, which results in a reduction of the lift generated by the aircraft main body and a same amount of increment of the lift generated by the ACS. Both variations of the lift from two aircraft components will lead to a respective change on their corresponding drags. However the drag reduction from the aircraft main body is less than the drag increment from the ACS when the magnitude of lift variations on the two aircraft components are the same. Therefore when the CG location moves rearward, the increment of the total drag of all aircraft components leads to an increment of the required engine gross thrust, which further leads to an increment of the effectiveness of thrust vectoring control.

7.2 Recommendations

Based on the work conducted in this thesis project, several recommendations are given for further flight mechanics simulations and analyses of thrust vectoring control applications on a civil transport aircraft:

- A more sophisticated modeling of thrust vectoring is necessary for detailed investigations and analyses of the effects and effectiveness of thrust vectoring control. Several simplifications have been adopted for the modeling of thrust vectoring in this project. For instance the influences of nozzle deflections on the Mach number of nozzle internal flow are neglected. Only the direct influences on nozzle section areas from nozzle deflections are considered. Thrust deflection angles are considered to be identical to the nozzle geometrical deflection angles in this project. The accuracy of the analytical solution for vectoring nozzle thrust calculation needs to be checked with more reliable data such as high fidelity CFD calculations or experimental tests.
- Aircraft data with higher fidelity is required for more accurate results. The aerodynamic tool used to prepare the aerodynamic database in this project is of low fidelity. Compressibility and viscosity are not considered based on the algorithm of the aerodynamic tool. Therefore nonlinear behaviors of the aerodynamic performance due to flow separations, wave drag and friction drag due to flow compressibility and viscosity are not of satisfactory accuracy. For thrust vectoring simulations under steady level flight conditions as conducted in this project, drag estimations are of great importance since the engine gross thrust hence the effectiveness of thrust vectoring control is directly related to the aircraft drag under steady level flight conditions. Aircraft mass and CG location have obvious influences on the effectiveness of thrust vectoring control under steady flight conditions. Aircraft mass and inertia data with more geometrical details and considerations are preferred.

- The possibility of rolling and yawing control with vectoring thrust needs to be investigated. Due to the time limitation as well as the absence of vertical tails from the digital aircraft model used in this project, rolling and yawing control of the modified VELA2 configuration with vectoring thrust is not simulated, even though the thrust vectoring model developed in this project has the capability of lateral and directional controls.
- Flight dynamics analysis of thrust vectoring control needs to be implemented. The flight mechanics simulations carried out in this project are focused on steady level flight conditions. The dynamic behaviors of thrust vectoring controls and the possibilities of improving the handling qualities of a civil transport aircraft with thrust vectoring control are also interesting to discover. To carry out flight dynamic analysis of thrust vectoring control, a dynamic model of the vectoring nozzle control effectors need to be developed, and the stability derivatives of the aircraft aerodynamic database also need to be prepared.

8 References

[1] Directorate-General for Research and Innovation EU, “Flightpath 2050, Europe's Vision for Aviation,” Publications Office of the European Union, Luxembourg, 2011.

[2] R. H. Liebeck, “Blended Wing Body Design Challenges,” Dayton, 2003.

[3] E. M. v. d. Veen, “Civil Application of Thrust Vectoring - An Exploration,” Melbourne, Australia, 1998.

[4] A. I. Omoragbon, G. J. Coleman, L. Gonzalez, B. Watters and B. Chudoba, “Feasibility Study of a Thrust Vector Control Transport,” Arlington, 2013.

[5] A. J. Steer, “Integrated Control of a Second Generation Supersonic Commercial Transport Aircraft Using Thrust Vectoring,” *AIAA,* pp. 454-464, 2000.

[6] E. Wilson, An Introduction to Thrust-Vectored Aircraft Nozzles, Saarbrücken: LAP LAMBERTAcademic Publishing, 2013, pp. 190-208.

[7] Anonymous, “VELA-Very Efficient Large Aircraft,” Airbus Deutschland, Hamburg, 2006.

[8] E. Torenbeek, Synthesis of Subsonic Airplane Design, Dordrecht: Springer, 1982.

[9] NASA, “The Blended-Wing-Body,” Langley Research Center, Hampton, Virginia, 1997.

[10] R. H. Liebeck, “Design of the Blended Wing Body Subsonic Transport,” *Journal of Aircraft,* vol. 41, no. 1, pp. 10-25, January-February 2004.

[11] R. M. Wood and S. X. S. Bauer, “Flying Wings / Flying Fuselages,” Reno, Nevada, 2001.

[12] A. R. Weyl, “Tailless Aircraft and Flying Wings,” *Aircraft Engineering,* pp. 41-46, 1945.

[13] Wikipedia, “Otto Lilienthal,” Wikimedia Foundation, [Online]. Available: http://en.wikipedia.org/wiki/Otto_Lilienthal. [Accessed 18 May 2015].

[14] M. A. Potsdam, A. M. Page and H. R. Liebeck, “Blended Wing Body Analysis and Design,” *AIAA,* pp. 799-805, 1997.

[15] A. Morris, P. Arendsen, G. LaRocca, M. Laban, R. Voss and H. Hönlinger, “MOB - A European Project on Multidisciplinary Design Optimization,” Yokohama, Japan, 2004.

[16] A. J. Morris FREng, “MOB A European Distributed Multi-Disciplinary Design and Optimization Project,” *AIAA,* pp. 1-10, 2005.

[17] M. Hepperle, “The VELA Project,” [Online]. Available: http://www.dlr.de/as/en/desktopdefault.aspx/tabid-188/379_read-636/. [Accessed 18 September 2015].

[18] A. Diedrich, J. Hileman, D. Tan, K. Willcox and Z. Spakovszky, “Multidisciplinary Design and Optimization of the Silent Aircraft,” in *AIAA*, Reno, USA, 2006.

[19] J. I. Hileman, Z. S. Spakovszky and M. Drela, “Airframe Design for Silent Fuel-Efficient Aircraft,” *Journal of Aircraft,* vol. 47, no. 3, pp. 956-969, 2010.

[20] D. Roman, J. B. Allen and R. H. Liebeck, “Aerodynamic Design Challenges of the Blended-Wing-Body Subsonic Transport,” *AIAA,* pp. 618-627, 2000.

[21] G. K. Richey, B. L. Berrier and J. L. Palcza, “Two-Dimensional Nozzle/Airframe Integration Technology - An Overview,” in *AIAA*, Orlando, 1977.

[22] B. Gal-Or, Vectored Propulsion, Supermaneuverability and Robot Aircraft, Haifa: Springer-Verlag, 1989, p. 192.

[23] J. Mace, D. Bowers, M. MacLean and E. Thayer, “Advanced Thrust Vectoring Nozzles for Supercruise Fighter Aircraft,” in *AIAA*, Monterey, 1989.

[24] W. B. Herbst, “Future Fighter Technologies,” *Journal of Aircraft,* vol. 17, no. 8, pp. 561-566, 1980.

[25] P. Costes, “Investigation of Thrust Vectoring and Post-Stall Capability in Air Combat,” *AIAA,* pp. 893-905, 1988.

[26] K. A. Deere, “Summary of Fluidic Thrust Vectoring Research Conducted at NASA Langley Research Center,” in *AIAA*, Orlando, 2003.

[27] B. Gal-Or, “Review of the Debate and the Development of Thrust Vectoring Technology,” *Thermal Science,* vol. 7, no. 1, pp. 1-6, 1998.

[28] W. F. Phillips, Mechanics of Flight, Hoboken: John Wiley & Sons, 2010.

[29] M. E. Dreier, Introduction to Helicopter and Tiltrotor Flight Simulation, AIAA, 2007.

[30] T. Melin, “A Vortex Lattice MATLAB Implementation for Linear Aerodynamic Wing Applications,” KTH, Stockholm, 2000.

[31] J. D. Anderson, Fundamentals of Aerodynamics, 5th Edition, New York: McGraw-Hill, 2011.

[32] T. Melin, “User's guide and reference manual for Tornado,” [Online]. Available: https://www.academia.edu/. [Accessed 23 10 2015].

[33] O. Gur, W. H. Mason and J. A. Schetz, “Full-Configuration Drag Estimation,” *Journal of Aircraft,* vol. 47, no. 4, pp. 1356-1367, 2010.

[34] B. Lokker, “Blended Wing Body LY Mass and Performance Prediction,” DLR, Hamburg, 2014.

[35] D. Howe, “Blended Wing Body Airframe Mass Prediction,” *Journal of Aerospace Engineering,* vol. 215 Part G, pp. 319-331, 2001.

[36] J. Roskam, “Part I: Preliminary Sizing of Airplanes,” in *Airplane Design*, Kansas, Roskam Aviation and Engineering Corporation, 1985, pp. 89-101.

[37] B. S. Aranjo, B. R. Hughes and H. N. Chaudry, “Performance Investigation of Ground Cooling for the Airbus A380 in the United Arab Emirates,” *Applied Thermal Engineering,* vol. 36, pp. 87-95, 2011.

[38] E. Obert, “4 The Aircraft Design Process,” in *Aerodynamic Design of Transport Aircraft*, Amsterdam, IOS Press BV, 2009, p. 25.

[39] E. A. Wilson, D. Adler and P. Bar-Yoseph, “Thrust-Vectoring Nozzle Performance Modeling,” *Journal of Propulsion and Power,* vol. 19, no. 1, pp. 39-47, 2003.

[40] B. Gal-Or, Vectored Propulsion, Supermaneuverability and Robot Aircraft, Jerusalem, Israel: Springer-Verlag, 1990.

[41] V. Sherbaum and M. Lichtsinder, “Jet Deflection Angles in Military, Civil and RPV Thrust Vectoring Aircraft,” *International Journal of Turbo and Jet Engines,* vol. 15, pp. 91-94, 1998.

[42] P. Malan and E. F. Brown, “Inlet Drag Prediction for Aircraft Conceptual Design,” *Journal of Aircraft,* vol. 31, no. 3, pp. 616-622, 1994.

[43] W. S. Levine, “Control Allocation,” in *Control System Applications*, CRC Press, 2011, pp. 250-273.

[44] T. A. Johansen and T. I. Fossen, “Control Allocation - A Survey,” *Automatica,* vol. 49, no. 5, pp. 1087-1103, 2013.

[45] S. M. Waters, M. Voskuijl, L. L. Veldhuis and F. J. Geuskens, “Control Allocation Performance for Blended Wing Body Aircraft and Its Impact on Control Surface Design,” *Aerospace Science and Technology,* no. 29, pp. 18-27, 2013.

[46] C. Huijts and M. Voskuijl, “The Impact of Control Allocation on Trim Drag of Blended Wing Body Aircraft,” *Aerospace Science and Technology,* no. 46, pp. 72-81, 2015.